



<http://researchcommons.waikato.ac.nz/>

Research Commons at the University of Waikato

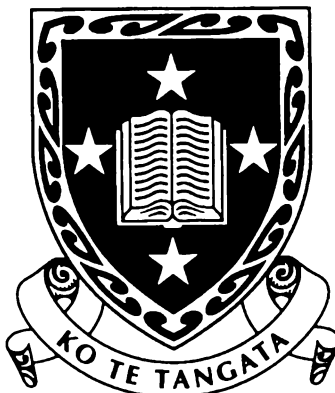
Copyright Statement:

The digital copy of this thesis is protected by the Copyright Act 1994 (New Zealand).

The thesis may be consulted by you, provided you comply with the provisions of the Act and the following conditions of use:

- Any use you make of these documents or images must be for research or private study purposes only, and you may not make them available to any other person.
- Authors control the copyright of their thesis. You will recognise the author's right to be identified as the author of the thesis, and due acknowledgement will be made to the author where appropriate.
- You will obtain the author's permission before publishing any material from the thesis.

Distributed Computing & Solid Oxide Fuel Cell Modelling



A thesis
submitted in fulfilment of
the requirements for the degree of
Doctor of Philosophy
at The University of Waikato
by

Rhys Edwin Foster

The University of Waikato
Hamilton
New Zealand
2004

TK 2931

.F61

2004

710|06

ISSUE
DESK

7-2004
2004

551797

© 2004 Rhys E. Foster

Abstract

Solid oxide fuel cells (SOFC) are a power generation technology that offers the potential to revolutionize the energy industry. Lower emissions and higher energy efficiencies than conventional thermal generation but, moreover, the ability to deliver these improvements in small generators, enables the distributed generation paradigm to flourish.

The objective of this work was two-fold; to develop a model to aid in the optimization of a tubular SOFC design, and to develop a distributed computing platform for the solution of large scale models on a network of desktop computers.

Distributed computing is the division of a computational problem amongst a number of computers. While a well established technology, having roots in the super-computer application space, distributed computing has never before been applied to SOFC modelling. A test application for distributed computing is detailed, showing the application of distributed computing techniques to a SOFC stack model. The test case is found to scale well with up to four clients, providing linear growth in processing overhead with each additional client. This illustrated the potential for a detailed SOFC model to be distributed across a network of PCs.

Computer modelling of an anode supported tubular SOFC is rare in the literature. Validation of a finite-element model was undertaken against experimental data, showing good correlation. The model was then exercised to optimize aspects of the cell design revealing key limitations in the anode electronic conductivity and cathode activation overpotential. Modelling predicted that the addition of a metallic mesh inside the cell would increase the output voltage by 28 mV and an experiment with two samples and two controls showed a gain of 30 mV. Simulation of the cathode showed that improving the exchange current density to accepted levels (i.e. from 20 mA.cm^{-2} to 200 mA.cm^{-2}) would give a concomitant increase in cell voltage from 580 mV to 658 mV (all other variables constant).

Reworking the distributed application to a generic interface for distributing Matlab problems allowed for a demonstration of the distributed solution of a short

stack of detailed (finite element) fuel cells. Four computers were used in the test one coordinating server and three clients to solve the models. Even though the three client computers were extremely unbalanced (individual solution times of 5, 25, and 30 minutes), the net effect was a solution time close to the sum of the processing power of the three or a 17% reduction from the total time for the best performing client. Again, this demonstrated the potential advantage to be gained from applying distributed computing to fuel cell models and further investigation with additional clients is strongly recommended.

This thesis describes advances in the design of a novel tubular SOFC gained through the use of a computer model. The demonstration of distributed computing technology for solving complex models is unique in the field of fuel cells and represents a significant contribution to fuel cell science and engineering.

Acknowledgements

Initial funding for this research was provided, in part, by the Foundation for Research, Science and Technology (FRST) in New Zealand under contract UOW804.

From May 2000 onwards facilities were provided by Acumentrics Corporation in Massachusetts, USA.

Table of Contents

Abstract	iii
Acknowledgements	v
Table of Contents	vi
List of Figures	x
List of Tables	xii
1 Introduction	1
1.1 Solid Oxide Fuel Cells	2
1.1.1 Fuel Cell Potential and Losses	3
1.1.2 Efficiency of a Fuel Cell	5
1.1.3 Fuel Cell Development	7
1.1.4 Solid Oxide Fuel Cell Components and Designs	8
1.2 Modelling Solid Oxide Fuel Cells	15
1.3 Distributed Computing	17
1.4 Distributed Computing for SOFC Modelling	19
1.5 References	19
2 Modelling Solid Oxide Fuel Cells	27
2.1 Fuel Cell Physics Modelling	27
2.1.1 Mass Transport	27
2.1.2 Heat Transfer	30
2.1.3 Chemical	32
2.1.4 Electrochemical	34
2.1.5 Geometric	36
2.2 Principles of Fuel Cell Modelling	39
2.3 Novel Fuel Cell Modelling Methods	41
2.3.1 Object-based Modelling	41
2.3.2 System Identification	42
2.4 Distributed Computing and Fuel Cell Modelling	44
2.5 References	45

3 Feasibility of Distributed Computing for Fuel Cell Modelling	51
3.1 Why Distributed Computing?	51
3.2 Software Implementation	52
3.2.1 User Interface and Model Structure	52
3.2.2 Client-Server Development	61
3.3 Initial Distributed Model Performance.	65
3.4 Further Work	66
3.5 References	66
4 Finite Element Model – Description & Validation	69
4.1 Model Description	69
4.1.1 Geometry	70
4.1.2 The Method of Finite Elements	71
4.1.3 Flow Field – Momentum Transport	72
4.1.4 Diffusion – Mass Transport	73
4.1.5 Electronic – Electron Transport	76
4.1.6 Electrochemistry	77
4.1.7 Thermal	81
4.1.8 Mesh and Solver	81
4.2 Model Validation	81
4.2.1 Single/Double-ended geometry	84
4.3 Conclusions	86
4.4 List of Symbols	86
4.5 Default Values	88
4.6 References	89

5 Component Analysis Results for a Tubular SOFC	91
5.1 Component Loss Calculations	91
5.2 Results & Discussion	97
5.2.1 Cathode Polarization	102
5.2.2 Anode Conductivity	104
5.3 Conclusions	107
5.3.1 Recommended Component Focus	108
5.4 References	108
6 Development of a Generic Distributed Computation Interface	111
6.1 Introduction	111
6.2 Distributed Computation with Matlab	111
6.3 Results & Discussion	115
6.4 Conclusions	120
7 Conclusions & Further Work	123
7.1 Conclusions	123
7.1.1 Finite Element Solid Oxide Fuel Cell Model	123
7.1.2 Distributed Computing for Fuel Cell Modelling	123
7.2 Further Work	124
7.2.1 Cell Modelling	124
7.2.2 Experimental Studies	125
7.2.3 Distributed Computing	125

Appendix A Distributed FEM Results Log Files	127
A.1 Solution.log	127
A.2 Communications (Comms.log)	130
A.3 Sample Client Log	137
Appendix B SOFC Materials	145
B.1 Electrolytes	145
B.1.1 Zirconia	145
B.1.2 Ceria	146
B.1.3 Other Electrolyte Materials	146
B.2 Anodes	147
B.3 Cathodes	147
B.4 Current Collection	148
B.5 References	149
Appendix C High Performance Computing	155
C.1 Massively Parallel Processors	155
C.2 Clusters	157
C.3 Networks of Workstations	159
C.4 Distributed computing	160
C.5 Internet Distributed Computing	160
C.6 References	161

List of Figures

Figure 1-1 General operating processes of a SOFC	2
Figure 1-2 Ideal Potential of a H ₂ /O ₂ fuel cell	4
Figure 1-3 Comparison of Gibbs (fuel cell) and Carnot (heat engine) theoretical efficiencies.	6
Figure 1-4 Siemens Westinghouse Tubular SOFC design [22]	10
Figure 1-5 Comparison of Siemens-Westinghouse designs: (a), (b) traditional; (c), (d) HPD [22].	11
Figure 1-6 Mitsubishi Heavy Industries tubular SOFC design [32]	12
Figure 1-7 Cross-flow planar stack concept [35]	14
Figure 1-8 The Sulzer Hexis cylindrical planar stack design [37]	15
Figure 2-1 Experimental and theoretical pressure distributions in a SOFC stack. (Lines are theoretical data) [11]	29
Figure 2-2 Cross-section SEM of a structured cathode [27].	35
Figure 2-3 Planar cross-flow unit cell [47]	40
Figure 3-1 User interface for a local solution	53
Figure 3-2 A ladder network element	53
Figure 3-3 Stack configuration options	56
Figure 3-4 Modelled cell interconnection	57
Figure 3-5 Stack temperature profile	58
Figure 3-6 Fuel configuration options	59
Figure 3-7 Cell solution flowchart	60
Figure 3-8 Client state machine	62
Figure 3-9 Server state machine	62
Figure 3-10 Client scaling for three row stack.	65
Figure 4-1 Section of tube and corresponding model geometry	71
Figure 4-2 Empirical fit of current density to total overpotential	79
Figure 4-3 Experimental and modelled data at 800°C (geometry A)	83
Figure 4-4 Experimental and modelled data at 850°C (geometry A)	83
Figure 4-5 Experimental and modelled data at 800°C (geometry B)	84
Figure 4-6 Experimental and modelled data at 800°C and (geometry D)	85
Figure 4-7 Axial current density plot showing single end and double end collection	85
Figure 4-8 Axial hydrogen mole fraction at electrolyte boundary (50% fuel utilization)	86

Figure 5-1 Component losses for double-ended 14 x 280 mm tube at 50% fuel utilization	98
Figure 5-2 Component losses for double-ended 14 x 280 mm tube at 75% fuel utilization	99
Figure 5-3 Component losses for double-ended 14 x 190 mm tube at 50% fuel utilization	99
Figure 5-4 Component losses for double-ended 14 x 190 mm tube at 75% fuel utilization	100
Figure 5-5 Component losses for single-ended 14 x 190 mm tube at 50% fuel utilization	100
Figure 5-6 Component losses for double-ended 14 x 190 mm tube at 75% fuel utilization	101
Figure 5-7 Relative losses for single-ended 14 x 190 mm tube at 50% fuel utilization	102
Figure 5-8 Cell performance increase due to cathode exchange current density	103
Figure 5-9 Change in component losses at various cathode exchange current densities (relative to $j_{0C} = 200 \text{ A.m}^{-2}$) for 28 cm cell at 50% fuel utilization with inlet only current collection.	104
Figure 5-10 Change in component losses due to the addition of a porous metallic annulus.	105
Figure 5-11 Percentage change in current density distribution due to introduction of anode insert.	106
Figure 5-12 Cell performance change due to anode thickness	106
Figure 5-13 Change in component losses at various anode thicknesses (relative to 1.4 mm).	107
Figure 6-1 Client and server application status during asynchronous solution processing.	112
Figure 6-2 Modified user interface for the distributed Matlab server.	113
Figure 6-3 File copy setup for distributed Matlab.	114
Figure 6-4 Solution performance of each client.	116
Figure 6-5 Solution processing times for each client.	116
Figure C-1 Earth Simulator floor plan – World’s fastest supercomputer (2003) [3]	156
Figure C-2 Kentucky Asymmetric Zero (KASY0) - first supercomputer under \$100/GFLOPS [6]	158

List of Tables

Table 1-1 Representative Solid Oxide Fuel Cell Technology Companies (2004 Q1)	7
Table 1-2 Representative Fuel Cell Technology Companies (2004 Q1 – non SOFC)	8
Table 2-1 Comparison of operating variables for a stack [11].	29
Table 2-2 Cell Performance data [17] (highlight shows most favourable value)	37
Table 4-1 Tube geometries	82
Table 5-1 Coefficients for equation 5-8 at various cathode exchange current densities.	93
Table 6-1 Computer specifications	115
Table 6-2 Distributed solution statistics.	117
Table 6-3 Results log excerpt.	119
Table C-1 Effect of interconnect on cluster price & performance (all prices approx.)	159

1 Introduction

Focus on fuel cells, as a vehicle for improved efficiency of electricity generation, is increasing in line with global concerns over humanity's impact on the environment. A fuel cell is an electrochemical reactor, meaning that fuel cells produce electrical power through the electrochemical conversion of a continuously supplied fuel. This avoids the thermodynamic limitations of the Carnot cycle, leading to the potential for higher efficiencies than traditional combustion based generation methods.

Of the various fuel cell technologies, solid oxide fuel cells (SOFC) offer benefits of high overall efficiency and the ability to run directly on lower hydrocarbon fuels [1-4]. Specifically, SOFCs are commonly operated on methane or natural gas, without any external fuel processing [3,4].

Designing a SOFC requires insight into the complex interrelations of electrochemistry, heat and mass transfer, structure, and geometry. Computer models are an effective way of understanding these interrelations; producing results in a timely and cost-effective manner.

Computer modelling and simulation in general has expanded in recent years, from simple models of heat transfer and structural stress, to the point now where detailed global climate models are being not only considered but solved. However, modelling in fuel cell development has advanced at a more conservative pace, making only small incremental improvements over time.

The explosive growth in personal computer ownership numbers and internet connectivity have driven an alternative modelling paradigm, distributed computing, to the fore and it is still in the early stages of being harnessed for scientific purposes. Although not all computer models are well suited to distributed computing, fuel cell stacks invariably make use of a repeated structure, so they are extremely well suited to the application of distributed techniques.

1.1 Solid Oxide Fuel Cells

SOFCS produce electrical energy from the oxidation of a fuel gas. The fundamental difference between this electrochemical process and a combustion (direct oxidation) process, is that the electron exchange parts of the reaction are separated (by some form of electrolyte), allowing the energy of the reaction to be applied to an electrical circuit. This is fundamental to all electrochemistry and is also the driving principle behind batteries. The processes underlying the operation of a SOFC, fuelled on hydrogen, are shown in Figure 1-1.

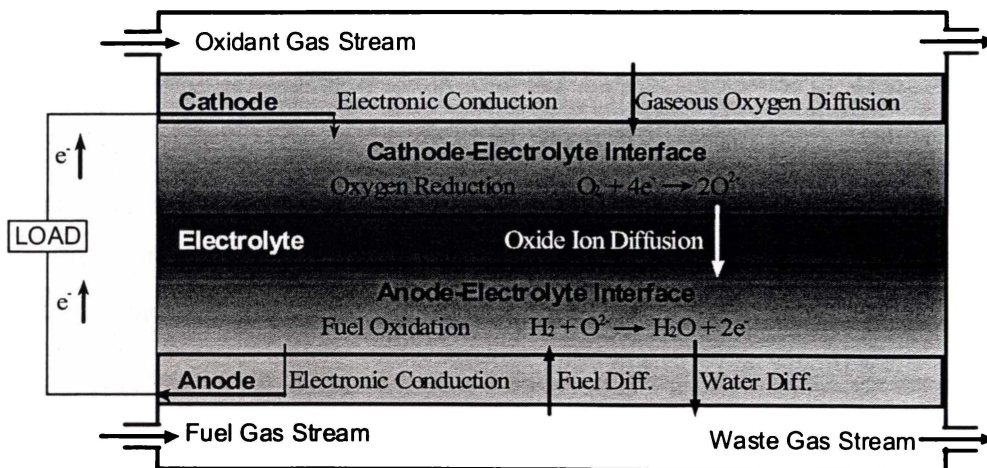


Figure 1-1 General operating processes of a SOFC

All SOFCs share some common features. Fuel and oxidant streams are always separated by a solid electrolyte-electrode structure. Due to the low voltage of the electrochemical cell (~1 V), practical electrical power can only be obtained through the connection of a number of cells in series. Often some form of current collector is employed either to connect cells (an inter-connect) or to provide a lower resistance path than the electrodes themselves.

The primary reactions in a SOFC are the electrochemical reduction of oxygen at the cathode and oxidation of fuel at the anode. In addition, a methane-fuelled SOFC involves the formation of carbon monoxide at the anode, steam (or air)

reforming, and the CO-CO₂ shift reaction occurring in the fuel channel and the porous anode. These reactions are detailed in equations 1-1 through 1-6.



1.1.1 Fuel Cell Potential and Losses

Ideal standard potential, or Gibbs voltage, refers to the potential difference between the two electrodes in an ideal fuel cell. This is different for each fuel oxidation reaction due to the free energy involved. The free energy ($\Delta_f G$ equation 1-7), is dependant on temperature (T), while the enthalpy ($\Delta_f H$) and entropy ($\Delta_f S$) change terms have very weak temperature dependence. This yields a linear temperature dependence of the ideal standard potential, E^0 , (equation 1-8) between room temperature and 1100°C (Figure 1-2), where n_e is the number of electrons transferred in the reaction, and F is Faraday's constant.

$$\Delta_f G = \Delta_f H - T\Delta_f S \quad (1-7)$$

$$E^0 = \frac{-\Delta_f G^0}{n_e F} \quad (1-8)$$

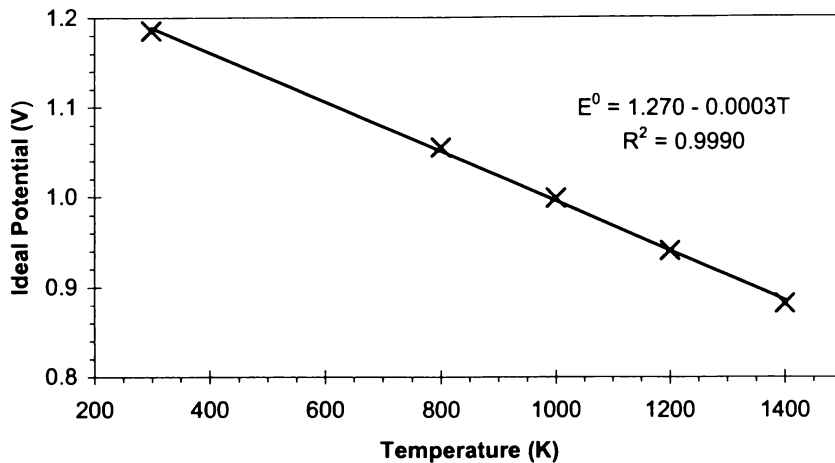


Figure 1-2 Ideal Potential of a H₂/O₂ fuel cell

The thermodynamics of the chemical equilibrium limits the amount of free energy available to do useful work. This chemical balance is reflected in the Nernst potential, E_N , given in equation 1-9, wherein R_G is the ideal gas constant and p_i is the partial pressure of species i . Put simply, the Nernst contribution to the cell potential is due to the local chemical concentration of the gases.

$$E_N = E^0 - \frac{R_G T}{n_e F} \ln \left(\frac{p_{H_2O}}{p_{H_2} \cdot p_{O_2}^{0.5}} \right) \quad (1-9)$$

A number of effects in the cell resemble electrical resistances, obeying Ohm's Law, and are thus referred to as ohmic losses, ohmic polarizations, or ohmic overpotentials. All of the electron transport mechanisms in the cell are modelled

this way; electronic conduction in electrodes and current collectors, and ionic conduction in the electrolyte. Charge transfer processes do not fall within this realm and are handled as activation overpotentials.

Activation overpotential arises from the activation energy required for the electrode reactions. That is, cell potential is further reduced by the kinetics of the chemical reactions occurring at the electrodes. The activation overpotential is most commonly modelled by the Tafel equation (equation 1-10) or the Butler-Volmer equation (equation 1-11), wherein η is the overpotential, i is the cell current, i_0 is the exchange current density, β is the transfer coefficient, and a and b are experimentally determined coefficients.

$$\eta = a + b \ln i \quad (1-10)$$

$$i = i_0 \left\{ \exp\left(\frac{\beta n_e F \eta}{RT}\right) - \exp\left[\frac{-(1-\beta)n_e F \eta}{RT}\right] \right\} \quad (1-11)$$

1.1.2 Efficiency of a Fuel Cell

Being an electrochemical reactor, a fuel cell is free from the temperature dependant restrictions on efficiency of a heat engine. This differentiation can be seen clearly in Figure 1-3. The Gibbs efficiency (equation 1-12) is the ratio of free energy ($\Delta_f G$) to the available energy (enthalpy, $\Delta_f H$), and is the upper limit to the efficiency of any system. A heat engine, however, is governed by the Carnot cycle, which limits the efficiency by the ratio of sink and source temperatures as shown in equation 1-13. The Gibbs efficiency improves as the temperature decreases, attaining unity at absolute zero (no entropy contribution). Carnot efficiency improves as the source temperature increases, and/or the sink temperature decreases, attaining unity only when the sink temperature is absolute zero (Temperatures in equations 1-12 and 1-13 are in Kelvin).

Lowering the sink temperature for a heat engine below ambient temperatures is impractical, due to the energy requirements of maintaining such a temperature. Further, sink temperatures below the condensation point of the exhaust gases is generally inadvisable, due to the formation of corrosive condensates in the exhaust. Figure 1-3 illustrates the differences in theoretical efficiencies of fuel cells and heat engines as a function of temperature, highlighting an operating point for SOFC.

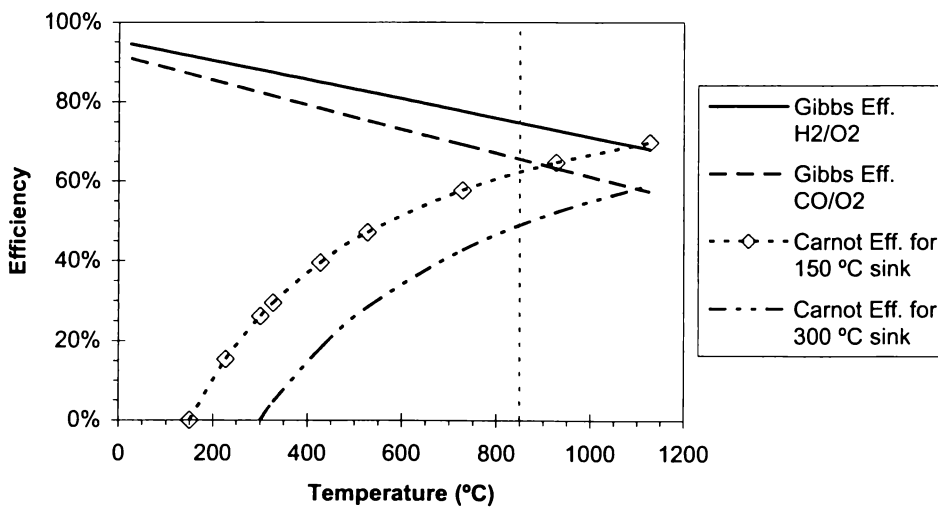


Figure 1-3 Comparison of Gibbs (fuel cell) and Carnot (heat engine) theoretical efficiencies.

$$\begin{aligned}
 \eta_G &= \frac{\Delta_f G}{\Delta_f H} \\
 &= \frac{\Delta_f H - T \Delta_f S}{\Delta_f H} \\
 &= 1 - \frac{T \Delta_f S}{\Delta_f H}
 \end{aligned} \tag{1-12}$$

$$\begin{aligned}
 \eta_T &= \frac{T_{source} - T_{sink}}{T_{source}} \\
 &= 1 - \frac{T_{sink}}{T_{source}}
 \end{aligned} \tag{1-13}$$

1.1.3 Fuel Cell Development

SOFCS have been researched for approximately 25 years, with considerable development over the last 10-15 years. There are now a number of companies in the business of SOFC development, with others looking into other fuel cell technologies, most notably proton exchange membrane (PEM) fuel cells. These companies, pursuing the commercialization of SOFC technologies, have begun presenting at international symposia [5-9]. A selection of active solid oxide fuel cell companies is outlined in Table 1-1 with companies pursuing other fuel cell technologies in Table 1-2.

Table 1-1 Representative Solid Oxide Fuel Cell Technology Companies (2004 Q1)

Company	Primary location	Fuel cell and proposed markets
Acumentrics	USA	Tubular for distributed generation (DG).
CFCL	Australia	Planar.
Fuel Cell Technologies	Canada	Tubular SOFC integrator (Siemens-Westinghouse cells).
Global Thermoelectric	Canada	Planar.
Siemens-Westinghouse	USA	Tubular for centralised generation.
Sulzer Hexis	Europe	Planar cylindrical for DG
Tokyo Gas	Japan	Tubular and planar development.

Table 1-2 Representative Fuel Cell Technology Companies (2004 Q1 – non SOFC)

Company	Primary location	Fuel cell and proposed markets
Anuvu	USA	Proton exchange membrane (PEM) fuel cell for automotive application.
Ballard	Canada	PEM fuel cell for automotive.
Fuel Cell Energy	USA	Molten carbonate fuel cell for centralised generation.
Medis Technologies	USA	Proprietary liquid electrolyte fuel cells for portable electronics.
Nuvera	Italy, USA	PEM fuel cell for automotive and DG.
Plug Power	USA	PEM fuel cell for DG.
Proton Energy	USA	PEM fuel cell for automotive and DG.
Relion (Avista)	USA	PEM fuel cell for DG.
United Technologies	USA	Phosphoric acid, PEM, alkaline developments. (Alkaline used in US space program).

1.1.4 Solid Oxide Fuel Cell Components and Designs

SOFCs can be categorized into three basic designs; electrolyte-supported, anode-supported, and cathode-supported. Each of these designs is named for its primary structural supporting component. In electrolyte-supported designs the electrolyte, typically yttria-stabilized-zirconia (YSZ), provides the structural support for the cell and is usually the thickest component. The thickness of the electrolyte is generally 100-500 µm, with electrodes being screen printed or slurry coated onto the electrolyte substrate [10,11]. In the electrode-supported designs an electrode forms the supporting member, with a thickness of 0.5-2 mm. The electrolyte is deposited on top of the electrode with a thickness of 10-40 µm, followed by the opposing electrode [12].

A strontium doped lanthanum manganite (LSM - e.g. $\text{La}_{0.9}\text{Sr}_{0.1}\text{MnO}_{3-\delta}^*$) is the commonly applied SOFC cathode material, with a nickel-YSZ cermet (ceramic-metal composite) forming the anode. Nickel oxide and YSZ are mixed and formed into a dense ceramic layer for the anode, and the nickel oxide is subsequently reduced to metallic nickel. During the reduction the porosity of the anode is formed.

Current collection and/or cell interconnection is performed by either a chromium based alloy (only for operating temperatures below $\sim 850^\circ\text{C}$) [13-17], a noble metal (e.g. platinum, gold, silver), or a strontium doped lanthanum chromite (LSC - e.g. $\text{La}_{0.8}\text{Sr}_{0.2}\text{CrO}_{3-\delta}$) ceramic interconnect [18-21].

One of the earliest SOFC geometries was the tubular design of Westinghouse (now Siemens-Westinghouse) which has oxidant flowing through the middle of a SOFC tube and fuel flowing on the outside of the tube [22]. However, it is the planar geometry that has received the majority of attention, with various groups looking into different configurations and components [10,15,23-30]. Planar designs rely on a bipolar plate to provide gas channels and electrical series connectivity, promising high power densities and ease of fabrication. Ongoing problems with sealing in planar designs has lead to the perception that tubular SOFCs are currently the closest to commercialization [31].

1.1.4.1 Westinghouse: Tubular & Flattened Tubular [22]

Westinghouse (now Siemens-Westinghouse) has been working with SOFC power generation since 1984. Their primary design is based on an extruded (or isostatically pressed) cathode tube of doped lanthanum manganite, which is then coated with electrolyte, anode and interconnect layers (Figure 1-4). The interconnection layer is plasma sprayed, while the other layers are applied by electrochemical vapour deposition (EVD). Slurry coating has recently been implemented for anode coating to reduce production costs, and has shown better

* δ represents the fact that the manganese ion (Mn) will exist in different valence states in the doped material.

performance than anodes coated by EVD. The materials used could be considered traditional: YSZ electrolyte, doped lanthanum manganite cathode, Ni-YSZ anode, and doped lanthanum chromite interconnection. The tube is closed at one end, with air applied via an air delivery tube, as shown in Figure 1-5. The active length of a tube is 150 cm, with a diameter of 22 mm.

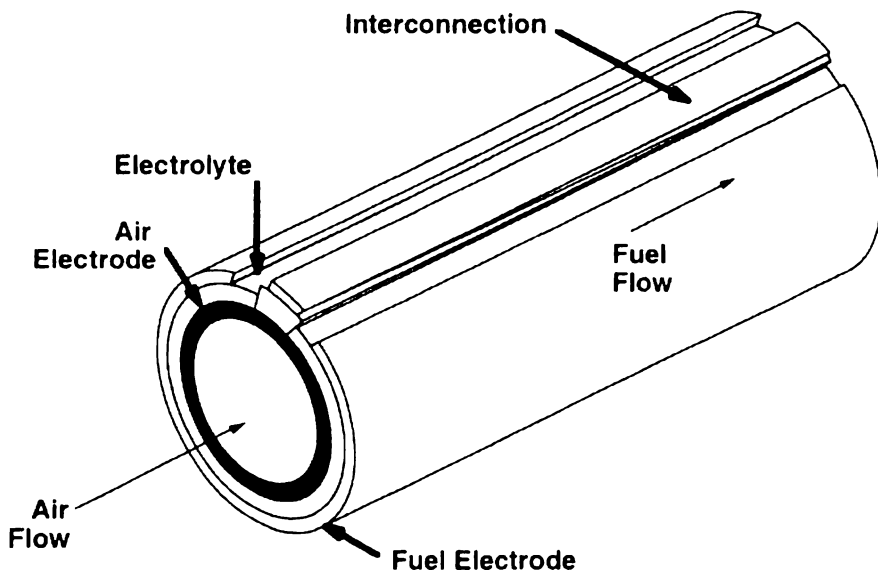


Figure 1-4 Siemens Westinghouse Tubular SOFC design [22]

More recently, Siemens proposed a new design to reduce the current path through the cell. Figure 1-5 shows the difference in current path between the traditional tubular design [(a) and (b)] and the new “high power density” (HPD) design [(c) and (d)]. Recalling the low electronic conductivity of the electrode materials, the key advantage of this design is the shortened current path across the cell. The airflow is also changed, in that the air makes a double pass though the fuel zone, although reaction on the inflow would be limited due to the blocking action of the interconnection, hence lowering the effective active area.

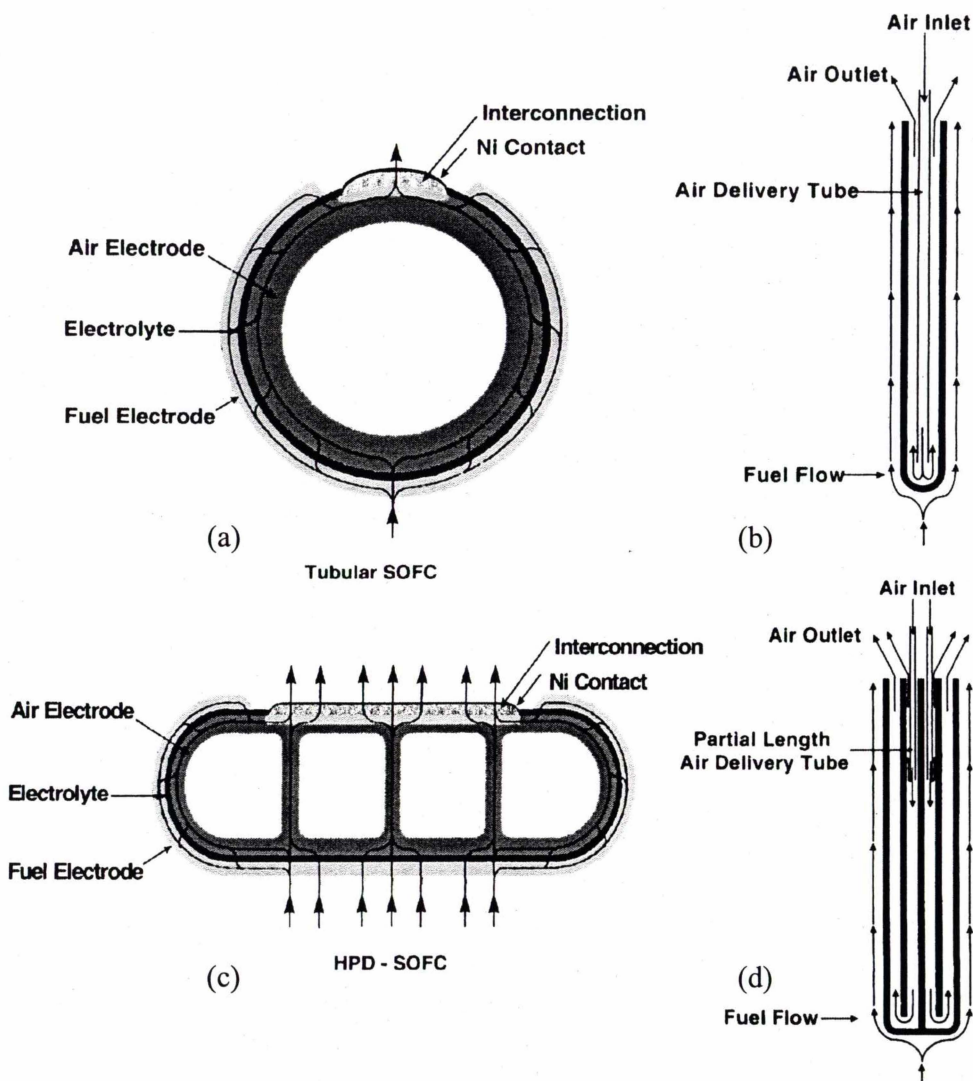


Figure 1-5 Comparison of Siemens-Westinghouse designs: (a), (b) traditional; (c), (d) HPD [22].

1.1.4.2 Mitsubishi Heavy Industries: Segmented Tubular [32]

Mitsubishi Heavy Industries (MHI) has also developed a tubular SOFC technology. In association with Tokyo Electric Power Company (1986 to 1989) and Electric Power Development Company (1989 onwards), MHI have developed SOFCs since 1984. The design is a segmented cells-in-series design, as shown in Figure 1-6. The cell starts with an extruded porous substrate tube of stabilized zirconia. Additional layers are then applied by plasma spray coating. The substrate tube has an outer diameter of 21 mm, with subsequent coatings being between 100

and 200 μm in thickness, giving a finished tube an outside diameter of approximately 22 mm with a length of 720 mm.

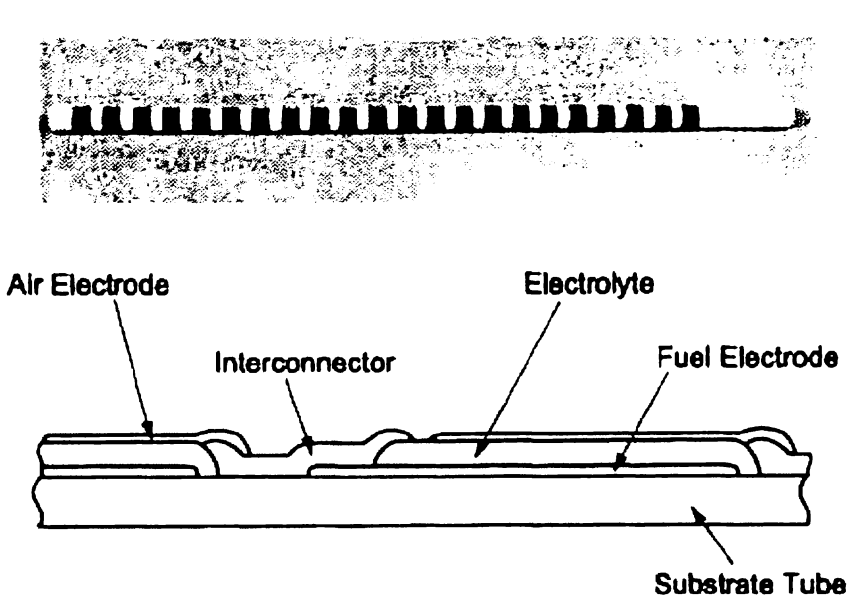


Figure 1-6 Mitsubishi Heavy Industries tubular SOFC design [32]

Similar to the Siemens-Westinghouse design, MHI utilizes a YSZ electrolyte, a nickel-YSZ anode, a LSM cathode, and a LSC interconnect. Notable differences include the fact that the fuel is inside the tubes, and each tube operates between 12 and 17 Volts, compared to ~ 0.7 Volts for the Siemens-Westinghouse design. The increased voltage (and hence, reduced current) from each tube can lead to a reduction in external ohmic losses and allows for a more fault-tolerant wiring design.

1.1.4.3 Micro-Tubular

In 1996 Kilbride proposed what is now called the micro-tubular SOFC [33]. Utilizing an electrolyte support tube of only 2.1 mm in diameter, this design touts rapid cycling, with the initial experiments proving heating rates of $100^\circ\text{C}.\text{min}^{-1}$. Subsequent modelling showed that a heating rate of $800^\circ\text{C}.\text{min}^{-1}$ would yield minimal stress, and led to experimentation at rates up to $40^\circ\text{C}.\text{s}^{-1}$ ($2400^\circ\text{C}.\text{min}^{-1}$), with no failures [34]. The anode (inside of the tube) is slurry coated, while the

cathode is applied with a number of methods (e.g. screen printing, painting). Metallic current collectors are added; typically a silver wire is wound around the cathode, while a nickel wire (coiled) is applied to the anode.

1.1.4.4 Acumentrics Anode Supported Tubular

Acumentrics Corporation has pursued a path at the juncture of tubular designs, with a small, anode supported, tubular SOFC. A thick (1-2 mm) nickel cermet anode forms the supporting member of this cell, to which an YSZ electrolyte is applied by vacuum infiltration. Following initial firing, the LSM cathode is dip-coated over the electrolyte and re-fired. The sintered cell has an outside diameter of 7 or 15 mm, with the cathode and electrolyte being approximately 100 μm , and 25 μm respectively. Various cell lengths have been tested, but all remain below 0.5 m in total length.

1.1.4.5 Traditional Planar

Due to the well developed and economical tape-casting process for ceramic fabrication, planar cell designs are still the most widely examined. Planar stacks are referenced by the flow regime of the fuel and oxidant gases. The primary planar flow configurations are; co-current flow (co-flow), in which the fuel and air channels run parallel and flows are in the same direction; counter-current flow (counter-flow), in which the fuel and air flows run in opposite directions through parallel channels; and cross-current flow (cross-flow), where the two channels (and hence flows) are perpendicular. A typical planar stack design is shown in Figure 1-7.

The cross-flow design is the most commonly employed, as it reduces the sealing requirements and manifold complexity compared to the parallel flow schemes. However, co- and counter-flow are still often used for comparison in planar simulations, often highlighting certain advantages of parallel flow geometries. An example of a parallel flow stack variant is outlined in *1.1.4.6 Sulzer Hexis: Cylindrical Planar* below, with further detail on simulations covered in the following chapter.

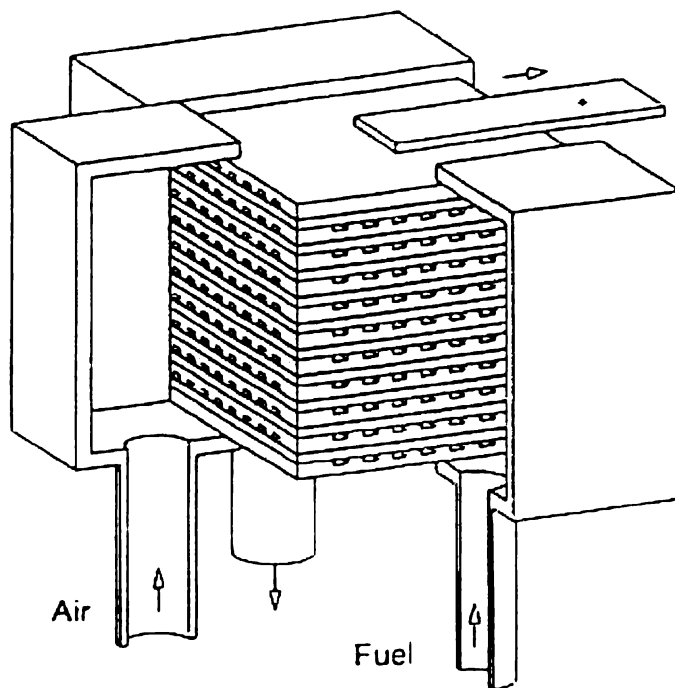


Figure 1-7 Cross-flow planar stack concept [35]

Planar systems offer very high current densities, up to 1.4 W.cm^{-2} [36], and with the widespread implementation of metallic interconnect layers, have the potential for high volumetric power density stacks. Still, primary concerns for planar stacks remain the slow heat-up required to prevent the cracking of the ceramic plates and finding effective sealing compounds for their present operating temperatures.

1.1.4.6 Sulzer Hexis: Cylindrical Planar [37]

Founded in 1997, Sulzer Hexis Ltd. is continuing development of their cylindrical planar system, which grew from work initiated by Sulzer Innotech in 1991. Figure 1-8 accentuates the novel method of eliminating the manifold problems encountered in traditional planar designs by using a machined interconnect plate. The interconnect plate provides excellent heat transfer (helping to maintain a uniform cell temperature), cell interconnection, and gas distribution of fuel (from a central feed column) and air (from outside the stack). Air supply for the fuel cell, provided from outside the stack, is preheated as it passes to the inner edge of the cell and is electrochemically reacted on the return path. It can hence be seen

that the Sulzer Hexis design is a form of co-current flow, as described in *1.1.4.5 Traditional Planar*.

The primary innovation of the Sulzer Hexis concept (the machined interconnect plate described above) is, however, also the weakest aspect of this system economically. These machined parts are very expensive to fabricate, thus increasing the system cost dramatically (a 1 kW system has approximately 70 of these plates). However, Sulzer Hexis has stated that, in industrial production quantities, it will meet the cost target of 1000 US\$/kW_{el} [37].

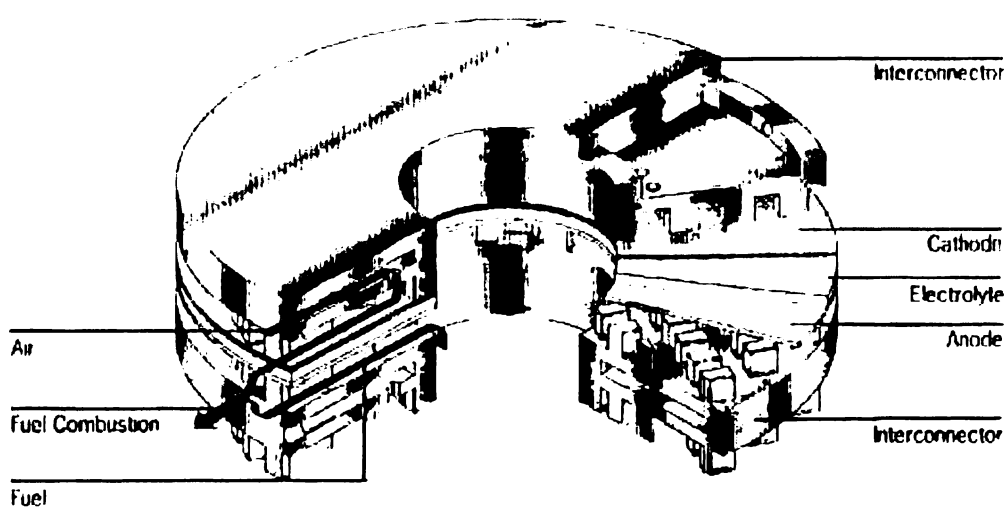


Figure 1-8 The Sulzer Hexis cylindrical planar stack design [37]

1.2 Modelling Solid Oxide Fuel Cells

The Solid Oxide Fuel Cell (SOFC) has been under development for more than two decades. A significant part of the development effort is the evolution of mathematical models to help determine the viability of ideas and find, theoretically, optimum conditions. A wide variety of effects have been modelled, utilising a broad range of disciplines. Modelling of SOFC systems has been reported frequently over recent years [3,38-48], however, models are still somewhat restricted in their application.

In order to solve (or even pose) models, a number of assumptions must be made. Some of these assumptions are regarding the nature of the studied system. For example, application of the Butler-Volmer equation carries the tacit assumption that the electrode reaction is at equilibrium and that no mass-transfer effects are present. Other assumptions are related to the solubility of the problem, a pertinent example of which is the treatment of heat transfer as described below.

Many earlier planar cell models examined two-dimensional temperature distributions, assuming the system was vertically adiabatic [49-52]. Primarily, this was done to reduce problem complexity, enabling solutions to be obtained, or to reduce the time required for solution. Subsequently, it was shown that this assumption had a significant impact on the utility of these two-dimensional models, and by the mid-1990's, three-dimensional thermal simulations were appearing, with results being significantly different from those obtained earlier [25,53,54].

Heat transfer by radiation is the other area prone to exclusion or mitigation by assumption. Earlier models ignored radiation [27,50], primarily due to the added complexity that radiation introduced. However, radiation has been identified as a significant mechanism of heat loss from the system during normal operation and it sharply impacts a thermal analysis [25,54]. The inclusion of radiation significantly increases the complexity of an analysis largely due to the generation and storage of view factors. A radiation view factor, F_{jk} , is defined as the fraction of radiant energy emitted from surface j that is directed at surface k . For an n surface system this requires an $n \times n$ matrix and using double precision numbers, this requires $4n^2$ bytes of storage.

By way of example, Hartvigsen et al [25] showed that, for a single cell model with 35 000 + radiation faces, in excess of 9 000 MB of RAM was required for view factor storage. In this case the excessive memory requirement was overcome by the adoption of a sparse storage scheme, because the studied system had many zero view factors (due to the aspect ratio of the cell). The view factor storage requirement was reduced to 26 MB, well within reach of many workstations of the

time. Nevertheless, the inclusion of radiation increased solution time from 1.2 hours to 9 hours [25].

Beyond the modelling of single cells, the complexity only increases. Consider the fluid dynamics in a tubular fuel cell stack cavity. A logical simplification would be to consider the analytical solution for flow over a bank of tubes at some average temperature and gas composition, which would be a reasonable approach for a system energy balance. However, the sensitivity of the fuel cell performance to temperature and the concomitant effect on heat generation could lead to significant local heating of cells. These hotspots would also correspond to areas of reactant depletion, modifying the density and heat capacity of the gas streams. So a true understanding of behaviour in the fuel cell stack, and even of the individual cells' performance, often necessitates more detailed modelling to be undertaken.

1.3 Distributed Computing

When a model or simulation of a complex system stretches beyond the in-house resources of available PC or workstation resources, two approaches are commonly taken. First to simplify the problem by narrowing the problem domain, either through assumptions or restriction of scope. The second, often impractical, option is to yearn for some time on a supercomputer to solve the problem! For most researchers, access to supercomputer resources is rare or extremely limited. Today a third option, distributed computing, presents an interesting alternative to traditional supercomputers enabling the solution of sophisticated models without compromising detail or scope .

Distributed computing refers to the use of geographically dispersed computing resources. Distributed computing had its genesis in the 1970's [55], developing in synergy with supercomputing. Distributed computing led to developments such as the Internet, and the Grid. The Internet grew from a vision of a highly reliable information/communication network. The Grid, conversely, aims to share supercomputing resources between collaborating institutions, focusing less on reliability and more on computational performance. An example of co-operative distributed computing is the Internet Domain Name System (DNS). DNS is implemented by a number of co-operating computers (DNS servers), that each

store information regarding specific hosts and other DNS servers, allowing for the resolution of host names into IP addresses. When software requires that a domain name be resolved (e.g. www.waikato.ac.nz) it asks the local DNS server, as defined in the local computer's TCP/IP (Transmission Control Protocol/Internet Protocol) settings. If the local server cannot resolve the name, it contacts other DNS servers in a hierarchical fashion (it keeps a list), until it can resolve the name. For example, assuming the local DNS server has no record of ".nz" it will contact the next higher DNS server, which we will assume is one of the root name servers. The root name server will direct the local DNS server to the ".nz" server which has a record for ".ac.nz" server, which in turn knows ".waikato.ac.nz", the Waikato University DNS server which returns the IP address of www.waikato.ac.nz. The robustness of the worldwide web and email attest to the reliability of this highly distributed system.

Distributed computing is not applicable to every problem, with the key requirement being that the problem can be logically broken down into semi-independent sub-problems. The difference in problem complexity between the complete problem and the sub-problems can be referred to as the granularity of the problem. Problems with a high granularity can have a large number of clients working on them simultaneously. Related to the granularity, the connectivity of a problem describes the amount of information that must pass between the client and server at each iteration and the effect this may have on other client data. A high level of connectivity may imply that the problem requires (or would be most efficiently solved with) a sequential algorithm. Thus, the nature of the problem can have a significant impact on the type of partitioning considered for a distributed computing solution.

Client and server software need to be created to leverage distributed computing techniques, although careful development will allow the software to be applied to many classes of problems. Unlike less distributed solutions (e.g. Clusters and supercomputers), the operating system requires no particular advanced features and the client can even be designed to function on multiple different operating systems (e.g. SETI@Home [56,57]).

1.4 Distributed Computing for SOFC Modelling

Models of SOFC single cells are becoming common-place, and are providing sufficient detail to compare favourably with experimental results. Stack models however are still based on homogenised or approximate cell parameters. Using a single cell as the sub-model, distributed computing techniques can provide detailed models of entire SOFC stacks without the need for extremely large models or supercomputers.

While SOFC modelling seems well suited to the application of distributed computing, no mention is made of this pairing in the literature. This thesis explores this paradigm by developing a computer application for the solution of complex fuel cell models across a network of computers.

Arrival at this juncture requires two main thrusts. First a client-server application is required to provide the distribution interface and, second, a model is required to distribute. To this end, a simple distributed computation client server application is developed to test the feasibility of a distribution interface with a simplistic model (chapter 3). Subsequently, the development of a detailed finite-element model of a tubular SOFC is undertaken and tested against experimental data (chapter 4). This model is used to provide insight into the cell design and to direct design improvements, some of which are tested experimentally (chapter 5). Finally the distributed application is modified to handle the complex model, and preliminary results of the distribution are presented (chapter 6).

1.5 References

1. Coutelieris, F. A., Douvartzides, S. & Tsiakaras, P. The importance of the fuel choice on the efficiency of a solid oxide fuel cell system. *Journal of Power Sources* **123**, 200-205 (2003).
2. Eguchi, K., Kojo, H., Takeguchi, T., Kikuchi, R. & Sasaki, K. Fuel flexibility in power generation by solid oxide fuel cells. *Solid State Ionics* **152-153**, 411-416 (2002).
3. Van herle, J., Marechal, F., Leuenberger, S. & Favrat, D. Energy balance model of a SOFC cogenerator operated with biogas. *Journal of Power Sources* **118**, 375-383 (2003).

4. Ahmed, K., Gamman, J. & Foger, K. Demonstration of LPG-fueled solid oxide fuel cell systems. *Solid State Ionics* **152-153**, 485-492 (2002).
5. Singhal, S. C. & Dokiya, M. (eds.) *Solid Oxide Fuel Cells (SOFC VI)* (The Electrochemical Society, Pennington, NJ, 1999).
6. Singhal, S. C. & Yokokawa, H. (eds.) *Solid Oxide Fuel Cells VII* (The Electrochemical Society, Pennington NJ, 2001).
7. Singhal, S. C. & Dokiya, M. (eds.) *Solid Oxide Fuel Cells VIII (SOFC VIII)* (The Electrochemical Society, Pennington NJ, 2003).
8. Stevens, P. (ed.) *3rd European Solid Oxide Fuel Cell Forum* (European Fuel Cell Forum, Lucerne, Switzerland, 1998).
9. Huijsmans, J. (ed.) *5th European Solid Oxide Fuel Cell Forum* (European Fuel Cell Forum, Lucerne, Switzerland, 2002).
10. Huiberts, R. C. & Huijsmans, J. P. P. in *Seventh International Solid Oxide Fuel Cell Symposium* (eds. Yokokawa, H. & Singhal, S. C.) 155-159 (The Electrochemical Society, NJ, Tsukuba, Japan, 2001).
11. Visco, S. J., Jacobson, C. & Jonghe, L. C. D. in *Fifth International Solid Oxide Fuel Cell Symposium* (eds. Stimming, U., Singhal, S. C., Tagawa, H. & Lehnert, W.) 710 (The Electrochemical Society, NJ, Aachen, 1997).
12. Larsen, P. H., Bagger, C., Linderoth, S., Mogensen, M., Primdahl, S., Jørgensen, M. J., Hendriksen, P. V., Kindl, B., Bonanos, N., Poulsen, F. W. & Maegaard, K. A. in *Seventh International Solid Oxide Fuel Cell Symposium* (eds. Yokokawa, H. & Singhal, S. C.) 28-37 (The Electrochemical Society, NJ, Tsukuba, Japan, 2001).
13. Huang, K., Hou, P. Y. & Goodenough, J. B. Characterization of iron-based alloy interconnects for reduced temperature solid oxide fuel cells. *Solid State Ionics* **129**, 237-250 (2000).
14. Horita, T., Xiong, Y., Kishimoto, H., Yamaji, K., Sakai, N. & Yokokawa, H. Application of Fe-Cr alloys to solid oxide fuel cells for cost-reduction: Oxidation behavior of alloys in methane fuel. *Journal of Power Sources* **131**, 293-298 (2004).
15. Kurokawa, H., Kawamura, K. & Maruyama, T. Oxidation behavior of Fe-16Cr alloy interconnect for SOFC under hydrogen potential gradient. *Solid State Ionics* **168**, 13-21 (2004).
16. Zeng, Z. & Natesan, K. Corrosion of metallic interconnects for SOFC in fuel gases. *Solid State Ionics* **167**, 9-16 (2004).

17. Zhu, W. Z. & Deevi, S. C. Opportunity of metallic interconnects for solid oxide fuel cells: a status on contact resistance. *Materials Research Bulletin* **38**, 957-972 (2003).
18. Yang, Y.-J., Wen, T.-L., Tu, H., Wang, D.-Q. & Yang, J. Characteristics of lanthanum strontium chromite prepared by glycine nitrate process. *Solid State Ionics* **135**, 475-479 (2000).
19. Duran, P., Tartaj, J., Capel, F. & Moure, C. Formation, sintering and thermal expansion behaviour of Sr- and Mg-doped LaCrO₃ as SOFC interconnector prepared by the ethylene glycol polymerized complex solution synthesis method. *Journal of the European Ceramic Society* **24**, 2619-2629 (2004).
20. Hilpert, K., Steinbrech, R. W., Boroomand, F., Wessel, E., Meschke, F., Zuev, A., Teller, O., Nickel, H. & Singheiser, L. Defect formation and mechanical stability of perovskites based on LaCrO₃ for solid oxide fuel cells (SOFC). *Journal of the European Ceramic Society* **23**, 3009-3020 (2003).
21. Zhu, W. Z. & Deevi, S. C. Development of interconnect materials for solid oxide fuel cells. *Materials Science and Engineering A* **348**, 227-243 (2003).
22. Singhal, S. C. in *Solid Oxide Fuel Cells (SOFC VI)* (eds. Singhal, S. C. & Dokiya, M.) 39-51 (The Electrochemical Society, Honolulu, 1999).
23. Achenbach, E. & Reus, U. in *Solid Oxide Fuel Cells (SOFC VI)* (eds. Singhal, S. C. & Dokiya, M.) 1125-1134 (The Electrochemical Society, Honolulu, 1999).
24. Sammes, N. M., Ratnaraj, R. & Fee, M. G. The effect of sintering on the mechanical properties of SOFC ceramic interconnect materials. *Journal of Materials Science* **29**, 4319-4324 (1994).
25. Hartvigsen, J., Elangovan, S. & Khandkar, A. in *5th International Conference on the Science and Technology of Zirconia V* (eds. Badwal, S. P. S., Bannister, M. J. & Hannick, R. H. J.) 682-693 (Technomic Publishing Company Inc., Lancaster, PA, Melbourne, 1993).
26. Bossel, U. G. (Swiss Federal Office of Energy, Berne, 1992).
27. Ferguson, J. R. in *2nd International Symposium on SOFCs* (eds. Grosz, F., Zegers, P., Singhal, S. C. & Yamamoto, O.) 305-312 (Commission of the European Communities, Athens, 1991).
28. Recknagle, K. P., Williford, R. E., Chick, L. A., Rector, D. R. & Khaleel, M. A. Three-dimensional thermo-fluid electrochemical modeling of planar SOFC stacks. *Journal of Power Sources* **113**, 109-114 (2003).
29. Tanner, C. W. & Virkar, A. V. A simple model for interconnect design of planar solid oxide fuel cells. *Journal of Power Sources* **113**, 44-56 (2003).

30. Yakabe, H., Ogiwara, T., Hishinuma, M. & Yasuda, I. 3-D model calculation for planar SOFC. *Journal of Power Sources* **102**, 144-154 (2001).
31. Singhal, S. C. Solid oxide fuel cells for stationary, mobile, and military applications. *Solid State Ionics* **152-153**, 405-410 (2002).
32. Mori, H., Omura, H., Hisatome, N., Ikeda, K. & Tomida, K. in *Solid Oxide Fuel Cells (SOFC VI)* (eds. Singhal, S. C. & Dokiya, M.) 52-59 (The Electrochemical Society, Honolulu, 1999).
33. Kilbride, I. P. Preparation and properties of small diameter tubular solid oxide fuel cells for rapid start-up. *Journal of Power Sources* **61**, 167-171 (1996).
34. Van herle, J., Ihringer, R., Sammes, N. M., Tompsett, G., Kendall, K., Yamada, K., Wen, C., Kawada, T., Ihara, M. & Mizusaki, J. Concept and technology of SOFC for electric vehicles. *Solid State Ionics* **132**, 333-342 (2000).
35. Buchkremer, H. P., Diekmann, U. & Stöver, D. in *2nd European SOFC Forum* 221- (Oslo, 1996).
36. Borglum, B. & Neary, E. in *Eighth Grove Fuel Cell Symposium* (London, 2003).
37. Diethelm, R., Schmidt, M., Honegger, K. & Batawi, E. in *Solid Oxide Fuel Cells (SOFC VI)* (eds. Singhal, S. C. & Dokiya, M.) 60-67 (The Electrochemical Society, Honolulu, 1999).
38. Zhu, H. & Kee, R. J. A general mathematical model for analyzing the performance of fuel-cell membrane-electrode assemblies. *Journal of Power Sources* **117**, 61-74 (2003).
39. Walters, K. M., Dean, A. M., Zhu, H. & Kee, R. J. Homogeneous kinetics and equilibrium predictions of coking propensity in the anode channels of direct oxidation solid-oxide fuel cells using dry natural gas. *Journal of Power Sources* **123**, 182-189 (2003).
40. Suwanwarangkul, R., Croiset, E., Fowler, M. W., Douglas, P. L., Entchev, E. & Douglas, M. A. Performance comparison of Fick's, dusty-gas and Stefan-Maxwell models to predict the concentration overpotential of a SOFC anode. *Journal of Power Sources* **122**, 9-18 (2003).
41. Roos, M., Batawi, E., Harnisch, U. & Hocker, T. Efficient simulation of fuel cell stacks with the volume averaging method. *Journal of Power Sources* **118**, 86-95 (2003).
42. Petrucci, L., Cocchi, S. & Fineschi, F. A global thermo-electrochemical model for SOFC systems design and engineering. *Journal of Power Sources* **118**, 96-107 (2003).

43. Ota, T., Koyama, M., Wen, C.-j., Yamada, K. & Takahashi, H. Object-based modeling of SOFC system: dynamic behavior of micro-tube SOFC. *Journal of Power Sources* **118**, 430-439 (2003).
44. Li, P.-W. & Chyu, M. K. Simulation of the chemical/electrochemical reactions and heat/mass transfer for a tubular SOFC in a stack. *Journal of Power Sources* **124**, 487-498 (2003).
45. Chan, S. H., Chen, X. J. & Khor, K. A. A simple bilayer electrolyte model for solid oxide fuel cells. *Solid State Ionics* **158**, 29-43 (2003).
46. Nagata, S., Momma, A., Kato, T. & Kasuga, Y. Numerical analysis of output characteristics of tubular SOFC with internal reformer. *Journal of Power Sources* **101**, 60-71 (2001).
47. Campanari, S. Thermodynamic model and parametric analysis of a tubular SOFC module. *Journal of Power Sources* **92**, 26-34 (2001).
48. Arriagada, J., Olausson, P. & Selimovic, A. Artificial neural network simulator for SOFC performance prediction*1. *Journal of Power Sources* **112**, 54-60 (2002).
49. Yentekakis, I. V., Neophytides, S., Seimanides, S. & Vayenas, C. G. in *2nd International Symposium on SOFCs* (eds. Grosz, F., Zegers, P., Singhal, S. C. & Yamamoto, O.) 281-288 (Commission of the European Communities, Athens, 1991).
50. Chindemi, M., Belmonte, G. & Malandrino, A. in *1st European SOFC Forum* (ed. Bossel, U.) 363 (Lucerne, 1994).
51. Arato, E. & Costa, P. in *2nd International Symposium on SOFCs* (eds. Grosz, F., Zegers, P., Singhal, S. C. & Yamamoto, O.) 273-280 (Commission of the European Communities, Athens, 1991).
52. Erdle, E., Gross, J., Müller, H. G., Müller, W. J. C., Reusch, H.-J. & Sunnenschein, R. in *2nd International Symposium on SOFCs* (eds. Grosz, F., Zegers, P., Singhal, S. C. & Yamamoto, O.) 265-272 (Commission of the European Communities, Athens, 1991).
53. Costamagna, P. & Arato, E. in *1st European SOFC Forum* (ed. Bossel, U.) 287- (Lucerne, 1994).
54. Achenbach, E. Three-dimensional and time-dependent simulation of a planar solid oxide fuel cell stack. *J. Power Sources* **49**, 333- (1994).
55. Fischer, M. J. & Merritt, M. Appraising two decades of distributed computing theory research. *Distributed Computing* **16**, 239-247 (2003).

56. Anderson, D. in *Bioastronomy 99: A New Era in Bioastronomy* (eds. Lemarchand, G. & Meech, K.) 511 (Astronomical Society of the Pacific: San Francisco, 1999).
57. Website, *SETI@Home website*, (1999) <http://setiathome.ssl.berkeley.edu>

2 Modelling Solid Oxide Fuel Cells

The Solid Oxide Fuel Cell (SOFC) has been under development for more than two decades. A significant part of the development effort is the evolution of mathematical models to help determine the viability of ideas and find, theoretically, optimum conditions. A wide variety of effects have been modelled, utilising a broad range of disciplines. Modelling of SOFC is widely recognised as having commenced in the early eighties with the work of Vayenas et al. [1-4]. Since then modelling has experienced rapid growth, with the power and accessibility of computer modelling being more fully exploited. For a discussion of modelling efforts prior to 1990 the reader is referred to Yentekakis et al [5].

Modelling is a very generic term, encompassing a number of methodologies, focusing on simulating certain aspects of a system to assist in understanding that system.

2.1 Fuel Cell Physics Modelling

Rigorous modelling of a SOFC requires the coupling of a number of disciplines. Electrochemistry is the prominent phenomenological effect in a fuel cell, and is coupled to heat and mass transfer in a large number of models.

2.1.1 Mass Transport

Multiple modes of mass transport can be considered in a solid oxide fuel cell (SOFC), including pressure-flow in the gas phase, gas diffusion in electrodes, and ion transport in the electrolyte.

Suwawarangkul et al. [6] have developed a simple single dimensional anode model to analyse the relative performance of different diffusion models of the porous SOFC anode. Three diffusion models are compared; Fick's law, the Stefan-Maxwell model, and the dusty gas model. The dusty gas model is shown to give the best agreement with experimental results, with the Stefan-Maxwell model performing well for a hydrogen-water system, but not so well for a methane system. Stefan-Maxwell model performance is attributed to the observation that

hydrogen has a much higher mobility, and the effects of Knudsen type diffusion (which accounts for collisions with solid structures) are much less. Both the dusty gas model and Fick's law account for Knudsen diffusion in the effective binary diffusivity coefficients whereas pure Stefan-Maxwell diffusion only considers the binary diffusivities. This also explains the observation that the Stefan-Maxwell model fails to account for variations in pore size.

One of the only examples of Nernst-Planck diffusion and migration applied to a SOFC is presented in a one-dimensional electrolyte model by Chan et al. [7]. The Nernst-Planck model accounts for the effect of the electric field on the migration of charged particles and in SOFCs is primarily relevant to the transport of oxide ions through the electrolyte. Chan et al. examined doped-ZrO₂ and doped-Bi₂O₃ electrolyte materials for application to SOFCs and ceramic oxygen generators. Oxygen permeation and electronic leakage current were analysed and showed that the electronic conductivity of bismuth oxide based electrolytes is advantageous for differential oxygen generators (i.e. separating oxygen from air without applied power). The benefit arises from the fact that the leakage current coincides with the oxygen gradient but is counteracted by ionic flow, thereby enhancing the oxygen permeation rate. Of course this leakage is detrimental to a SOFC and, in this case, the zirconia electrolyte is favoured. The model was subsequently expanded to study bi-layer electrolytes, comprised of a YSZ blocking layer applied to a doped-Bi₂O₃ or doped-Ce₂O₃ electrolyte [8]. Significant performance improvements were concluded to be possible contingent on the blocking layer being dense and ultra thin (sub-micron).

2.1.1.1 Reactant distribution

Early modelling in this area gave a differential flow effect of 95% to 110% of average flow rate [9]. This was subsequently refined for the optimisation of design parameters to prevent unfavourable flow distributions [10]. More recently, the effect of reactant distribution on the actual operating parameters of a SOFC has been undertaken [11]. Figure 2-1 shows the variations in pressure (and hence flow) throughout a stack and the impact on stack output is detailed in Table 2-1.

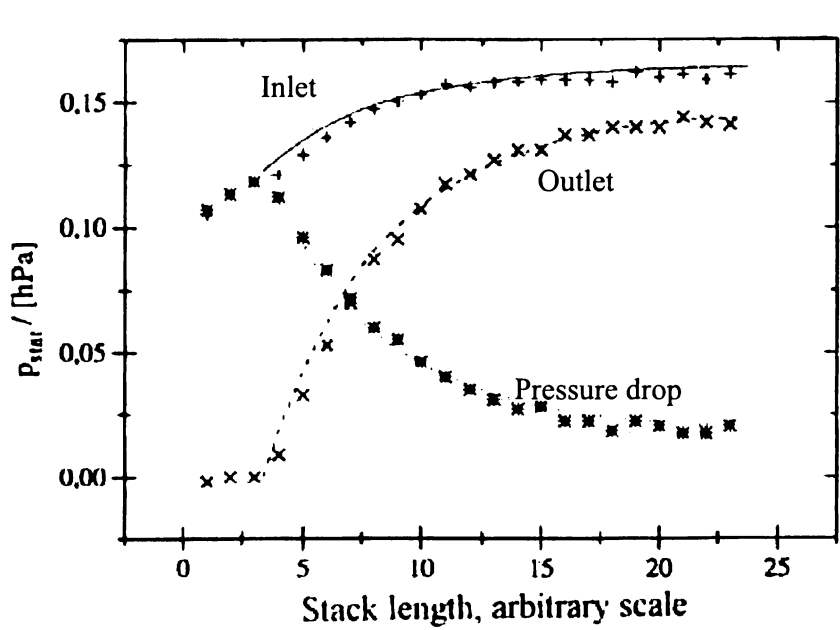


Figure 2-1 Experimental and theoretical pressure distributions in a SOFC stack.
(Lines are theoretical data) [11]

Table 2-1 Comparison of operating variables for a stack [11].

	Flow simulation	Voltage (V)	ΔV (mV)	Power (W)	T_{\max} (K)	T_{\min} (K)	dT/ds (K.mm ⁻¹)	Δj_{\max} (mA.cm ⁻²)
Cross-Flow	With	0.732	4.7	1099	982.2	904.5	1.51	220.2
	Without	0.734	0.1	1102	973.2	919.4	1.34	232.1
Co-Flow	With	0.720	1.7	1080	978.1	897.1	1.51	322.2
	Without	0.725	0.3	1088	967.9	896.6	1.31	195.8
Counter-Flow	With	0.744	7.3	1116	988.0	934.2	1.67	410.8
	Without	0.746	0.4	1118	982.8	941.8	1.43	307.1

The rows in Table 2-1 show the differences between simulations with and without a stack-level flow model for various flow geometries. While it is evident that the effect on output (power) is less than 1%, it is also apparent that the temperature and current density ranges are significantly broader with the more detailed simulation. Results are also given for a variation in the ratio of outlet to inlet

manifold cross-sectional areas. An outlet air manifold with twice the cross-sectional area of the inlet manifold is shown to reduce the non-uniformity of airflow to approximately 10% (from 75% at equal areas).

2.1.2 Heat Transfer

Temperature distributions are central to the modelling of SOFC, as variations in temperature across a cell can lead to dramatic variations in available current density, especially when coincident with areas of fuel, or oxidant, depletion. The modes of heat transfer in a SOFC cover the gamut, with conduction in solid and gas phases, convection in the gas phase and between the solid and gas, and radiation between bodies.

A number of planar cell models have been expanded to account for vertical temperature distributions in a stack. This is of particular interest for a larger stack as the low thermal conductivity of the ceramic components makes the propagation of temperature changes very gradual. Of course, the use of a metallic interconnect significantly improves this situation but it also causes greater heat loss from the stack due to the higher surface temperature [12]. Thermal transience (or thermal lag) is also of interest, with the significant heat capacity of a stack playing a crucial role.

Thermal transience was becoming prevalent in SOFC modelling by 1994 and, while gradual heating has been the norm, one model compares the minimum heating times with a heated gas stream and simple radiative heating, quoting 2 and 5 hours respectively [13]. Following warm-up, initiating reactant flows and drawing electric current causes another equilibration to take place, from a relatively constant temperature to the steady state distribution. For a particular set of boundary conditions, this start-up equilibration has been modelled to take approximately 7 minutes to be close to steady state but 33 minutes to actually reach steady state [12]. After 7 minutes the temperature contours had a similar distribution to the steady state and the maximum and minimum temperatures are within about 2 cm of their steady state locations. However, the actual temperatures at 7 minutes were up to 60°C different from the steady state values obtained at 33 minutes.

Another source of thermal transience is load change. When the load (and thus current density) is increased, the waste heat of the cell is also increased; hence another thermal equilibration process occurs. While the temperature increases the cell voltage also increases, due to the temperature dependant reduction in cell resistance. In the case of a constant electrical power load step-change, both the voltage and current would step-change, overshoot, and re-equilibrate. A model on this effect shows that, for a step-change in current, the settling time is relatively independent of the magnitude of the change in current density and is more dependant on the thermo-physical properties of the materials [13]. Differences between ceramic and metallic interconnects exist, with a ceramic interconnected stack accounting for 90% of the voltage drop in approximately 2 minutes, while a similar metallic arrangement takes 5 minutes.

Modelling of a co-flow cell has shown that a heat front forms in the direction of gas flow and, further, that the cell will extinguish should this front reach the exit [14]. The proposed solution is to periodically reverse the gas flow, which causes part of the heat front to remain in the cell and reverse direction. Further analysis determined that a sustainable cycle, allowing reasonable operating temperatures, could be achieved with this periodic reversal. However, no serviceable mechanism to implement this reversal was offered.

Hot spots can occur in a cell due to the formation of cracks, particularly the growth of micro-cracks in the ceramic electrolyte. The formation of a crack, aligned with the first channel may lead to a reduction in power output of 39% [15].

Automotive applications for fuel cells are receiving increased attention. Petruzzi et al. developed a thermal and electrochemical model of a planar SOFC stack for application as an automotive auxiliary power unit (APU) [16]. Building on the modelling representation of Achenbach [17] the dynamic model attempted to optimise the heating time by installing a heat exchanger between the burner and stack. Regulating the flow through the heat exchanger allows temperature gradients in the stack to be controlled. However, even with an unconstrained airflow the minimum heat-up time achievable was 20 minutes (from 25°C) which

is identified as too long for an automotive application. Cool-down presents another problem in that active cooling is not an option. Passive cooling is modelled with the constraint that the surface temperature must not exceed 100°C. This safety related constraint was shown to necessitate improvement in the insulation package either doubling the insulation thickness or using improved materials. A related benefit of improving the insulation was a concomitant increase in the average stack temperature, from 250°C to 450°C, after 20 hours of cooling, providing a significant reduction in restart time (~15 minutes from 250°C to ~8 minutes from 450°C).

2.1.3 Chemical

Chemical equilibrium and reaction rates drive the electrochemistry in the cell with reforming reactions working in synergy with the electrochemistry. Any chemical modelling is closely coupled with mass transport and heat transfer.

The “segmented cells in series” design of Mitsubishi is the focus of a finite volumes model examining the design of a concentric internal reformer tube (one for each cell). Nagata et al. conclude that a graded catalyst density in the internal reformer can be used to flatten the temperature profile along the cell [18].

Focussing on the creation of an autothermal system, Aguiar et al. also analysed a tubular steam reformer inside a tubular SOFC (anode inside design – not segmented) [19]. A two-dimensional heterogeneous model of the reformer is coupled with a one-dimensional electrochemical and thermal model of the SOFC. Similar to Nagata et al., severe cooling at the reformer inlet is overcome by lowering the local activity of the reforming catalyst which, while simple in the model, is noted to be non-trivial in reality. A number of limitations in this model become apparent on closer analysis. Heat transfer by radiation is accounted for with a general expression for radiation between two long concentric cylinders. This would appear to be unjustified as the model generates significant temperature gradients, suggesting a more detailed treatment should be considered. A constant cell voltage was applied “as both electrodes are normally good conductors”, citing Haynes & Wepfer [20]. Haynes & Wepfer considered the Westinghouse tubular design in which current only traverses the tube circumference; however, Aguiar et

al. assumed rotational symmetry, requiring current to be collected at the ends of the tube. This type of tubular arrangement has been well cited as having considerable losses in the current collection [21-23], making a constant cell voltage unreasonable. Notwithstanding this argument, the constant cell voltage assumption has also been shown to be invalid for the Westinghouse design [24] and is, to some extent, supported by the fact that Westinghouse chose to pursue a “high-power-density” design to reduce circumferential losses. Finally, the open circuit potential in the Nernst equation is presented as the ideal standard potential (without temperature correction) rather than the Gibb’s potential, introducing a further error (approximately 200 mV – or 20% – at 800°C).

Aguiar et al. subsequently extended their model, adding direct reforming on the anode to account for methane slippage through a low activity reformer [25]. This revision showed a steep temperature gradient at the reformer outlet due to the direct reforming on the anode surface.

The Colorado School of Mines has applied their hydrocarbon reaction modelling to an analysis of a planar SOFC fuel channel. Contrary to the accepted practice (that a reforming agent is necessary), Walters et al. considered operation on a pure fuel stream, modelling direct hydrocarbon oxidation at the anode as well as surface and gas phase reactions [26]. The one-dimensional isothermal, isobaric model considered a feedstock of dry natural gas (95% methane, 5% ethane) and used a detailed hydrocarbon reaction model (2498 reactions among 291 species) to predict the formation of cyclic and polycyclic hydrocarbons. Cyclic hydrocarbons are cited as indicators of coking propensity, that is, molecular carbon is likely to form in the presence of these cyclic hydrocarbons. The kinetic model predicted concentrations of cyclopentene as high as 0.4 ppm with increasing mole fraction along the channel length. The low concentration was attributed to the combination of a short residence time in the catalyst and the slow rate of molecular weight growth processes. Conflicting behaviour was predicted by the equilibrium calculations which showed extremely high coking propensity at the fuel channel inlet (due to the low oxygen atom content). Reducing the fuel cell operating temperature from 900°C to 800°C was shown to reduce the coking propensity by several orders of magnitude.

2.1.4 Electrochemical

Elementary electrochemical effects are often modelled with a simple resistive model of a cell, simplifying the voltage-current (V-I) characteristic of the cell to a linear drop from open circuit potential. However, better understanding of the fuel cell is obtained from more detailed treatments of the electrochemistry.

In order to account for the effect that the electrode-electrolyte interface has on the cell performance, electrochemists developed the concept of the three phase boundary (tpb) length. It is generally thought that the electrochemical reactions in a fuel cell occur at a three phase boundary, that is, the juncture of electronic conductor, ionic conductor and reactant. Mixed conduction electrodes (with significant ionic and electronic conductivity) somewhat mitigate this, but are beyond the scope of this discussion. Because the three phase boundary is not usually uniform (consider the anode cermet – a mixture of ion conducting ceramic particles, electron conducting metal particles and void space), the tpb length is used to account for the extension of the active surface area from the modelled interface, effectively scaling the assumed surface area. Recent models have attempted to further characterise interfacial effects as detailed below.

Herbstreit et al. analysed the cathode electrolyte interface with experimental work and three-dimensional finite element modelling [27]. Experimental trials consisted of increasing the surface area of the electrolyte substrate by screen-printing electrolyte particles onto the electrolyte surface before applying the pure LSM cathode coating (Figure 2-2). A number of trials were conducted, examining surface area enlargements of 0 to 50%. Modelling of the enlarged surface area showed excellent agreement with the experimental results.

Also working with increased cathode surface area, Virkar et al. developed an empirical expression for the effective charge transfer resistance in terms of electrode morphological and bulk properties (e.g. grain size, porosity, thickness) [28]. Experimental trials showed reasonable agreement with the proposed expression, supporting the thesis that an asymptotic value of the effective charge transfer resistance can be calculated (as thickness tends to infinity).

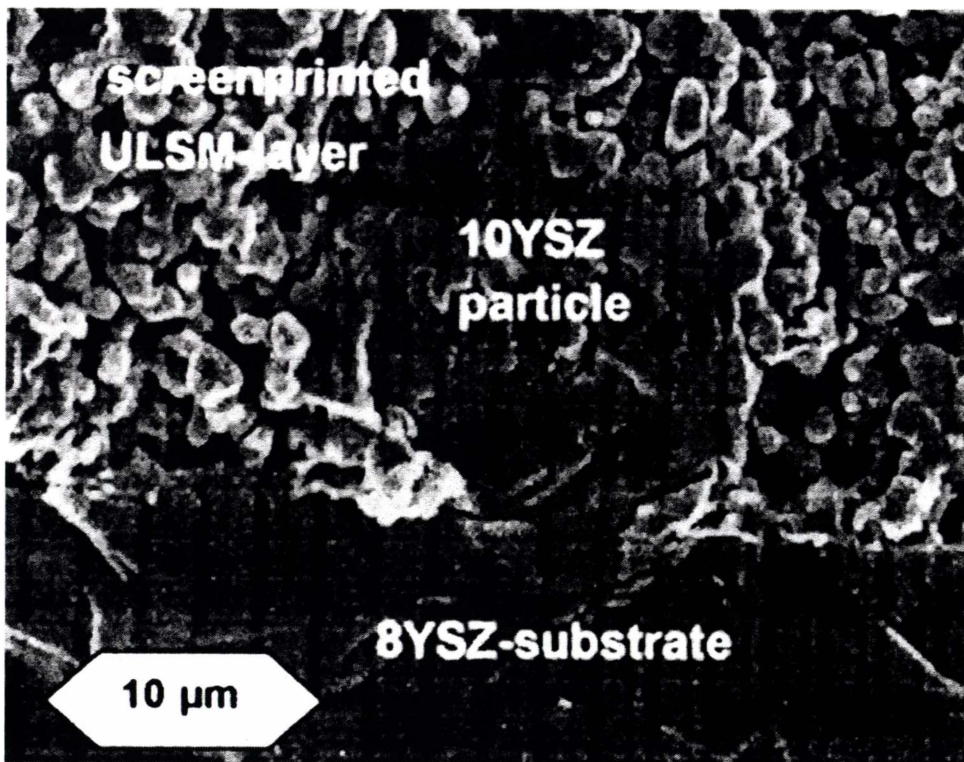


Figure 2-2 Cross-section SEM of a structured cathode [27].

Approaching electrode optimization from a different angle, Chan et al. developed a model of the anode using a random packing of spheres with electronic and ionic conductivities determined by percolation theory [29]. Activation overpotential was modelled by the well known Butler-Volmer equation (equation 2-1, where j is the current density, j_0 the exchange current density, β the transfer coefficient, n_e the number of participating electrons, E_{act} the activation overpotential and F , R and T have their usual meaning). The detailed treatment showed that total overpotential at the anode exhibits a minimum which is dependant on particle size and thickness of the anode as well as water content of the fuel stream. Increasing water content of the fuel stream was shown to reduce anode polarization which, as Virkar et al. observed, explains the concave up curvature in typical SOFC voltage current curves [28]. Further, as the anode particle size is reduced, the effect of water vapour content is accentuated. Similar to Virkar et al., the anode thickness was shown to have very little effect on total anode polarization, beyond some limiting value. However, while Virkar et al. stated an asymptotic effect, Chan et

al. showed a slightly deleterious effect for increasing the anode thickness beyond an optimal value.

$$j = j_0 \left\{ \exp \left[\beta \frac{n_e F E_{act}}{R T} \right] - \exp \left[(\beta - 1) \frac{n_e F E_{act}}{R T} \right] \right\} \quad (2-1)$$

Prior to their anode micro model, Chan et al. presented a sensitivity analysis (to component thicknesses) using literature values for the various electrochemical properties in a planar solid oxide fuel cell [30]. The model endorses the superiority of an anode supported design, yielding approximately twice the current density of electrolyte or cathode supported cells, even in the case of a cathodic pressure of 400 kPa (~4 atm).

2.1.5 Geometric

2.1.5.1 Planar Geometric Effects

Because cross-flow systems are simpler to seal, planar fuel cell developers are currently focussed on this geometry, although many simulations examine co- and counter-flow geometries, in some cases to the exclusion of cross-flow [14,31,32]. A well-regarded model details the thermal and electrical benefits of parallel flows (Table 2-2) but highlights the point that the cross-flow design is the most readily realised; “From the engineering point of view the cross-flow of fuel and air in the cell is easiest to verify by the manifolding system. Therefore the cross-flow design is most frequently applied in the tests ...” [17] p340. Others have also observed that parallel-flow has significant performance advantages over cross-flow [5,33,34], however, physical realisation of a parallel flow planar design is isolated to the Sulzer-Hexis cylindrical planar design, which uses a substantially different flow pattern to these models (see section 1.1.4.6).

Table 2-2 Cell Performance data [17] (highlight shows most favourable value)

Parameter	Cross-flow	Co-flow	Counter-flow
Cell voltage (V)	0.682	0.674	0.708
Cell power (W)	20.46	20.21	21.23
Maximum thermal gradient ($^{\circ}\text{C.mm}^{-1}$)	7.09	5.08	5.13
Maximum solid temperature ($^{\circ}\text{C}$)	1061	1013	1052
Minimum solid temperature ($^{\circ}\text{C}$)	823	861	910
Maximum current density (mA.cm^{-2})	368	184	432
Efficiency (%)	52.2	51.6	59.2

Interconnect rib width has been shown to be an important quantity in planar cell design, initiated with a model examining the specific effects of rib thickness [35]. The model clearly showed that the current density under the ribs is strongly dependant on in-plane diffusion of gases through the electrodes and is hence much lower than beneath the channels. Rib area efficiency was subsequently defined to indicate the effect of the rib width, and this notation has been adopted by others [36]. Alternatively, an analysis of circular contacts was shown to collect a greater power than rib contacts [37]. The circular contact layout proposed is similar to that later adopted for the Hexis project (see section 1.1.4.6).

Tanner et al. provided a conflicting analysis of interconnect design having developed a general quantitative expression for the design of optimal interconnects and concluding that ribs are the superior current collector [38]. However, a number of significant assumptions are not accounted for. In the solution of the differential equations it becomes apparent (although not stated) that the Nernst potential is considered constant throughout the cell which, while necessary for the analytical solution of the differential equations, is equivalent to assuming a uniform current density, negligible fuel utilization, and an isothermal cell. Uniform current density in an interconnect performance model is a major

shortcoming and, when coupled with the claim of a critical quantitative comparison of geometries, mitigates the conclusions. Additionally, the diameter and spacing of the circular contacts are equated to the rib width and channel spacing respectively, yielding a much lower contact area. A real implementation of circular contacts would likely consider the overall cell pressure drop and total volume of material as design constraints, both of which would lead to a greater number of contacts than considered by Tanner et al. Further, circular contacts would promote some mixing of the gas streams, alleviating the effects of high current density areas in the cell. Finally, the flow orientation considered for the rib design is a parallel-flow arrangement which, as discussed earlier, has not been physically realised outside of the laboratory. A cross-flow arrangement could, quite feasibly, yield results more in line with those developed (by Tanner et al.) for circular contacts.

Dimensions of the electrolyte and electrodes have received varied attention. Obviously the pursuit of thinner electrolytes is strongly sought to reduce the cell specific resistance. The majority of designs use a thick electrode (or substrate) to support the cell, applying a thin film electrolyte (e.g. Westinghouse – cathode support, Mitsubishi Heavy Industries – porous substrate and, Acumentrics, Global Thermoelectric – anode support). Providing a counterpoint to this, Costamagna and Arato presented a compelling model of reactant and current density distributions (in a planar cell) with the conclusion that any component (electrolyte or electrode) less than 20 microns thick is likely to cause significant resistance to mass and charge diffusion [10]. This can be easily understood by considering the in-plane conductivities, which play a very important role in planar designs. Reducing the thickness of a component reduces its cross-plane resistance. However, it also increases its in-plane resistance and it is in-plane electrical and ionic conduction that are critical to getting charge carriers to the current collecting ribs, as mentioned above.

Stresses caused by thermal expansion are of particular importance to SOFC design. The greatest stress has been identified to occur in the region of the cathode, and could be relieved by a reduction in the thermal expansion coefficient of the cathode [39].

2.1.5.2 Tubular Geometries

Tubular designs, including cathode supported (Siemens-Westinghouse), segmented (Mitsubishi Heavy Industries), anode supported (Acumentrics) and electrolyte supported (Keele University), have received less attention in the modelling literature than the planar designs. Focus on planar modelling could be postulated as being related to the ready extrapolation from the flat cells commonly used in SOFC cell experimentation to planar geometries.

Campanari et al [40] provided a sensitivity analysis in their tubular cathode supported SOFC model, highlighting the necessity for a detailed reforming kinetics model of a hydrocarbon fuelled system. Other modelling of the Siemens-Westinghouse tubular design has been concerned with heat and mass transfer inside a cell, assuming a uniform stack environment [24].

Embedding a tubular reformer inside a tubular fuel cell as modelled by Aguiar et al. and Nagata et al. is expounded in detail in section 2.1.3

Micro-tubular models are necessarily of the exploratory and “proof-of-concept” varieties, with analyses of cell conduction losses [23] and fluid flow in prototype units [41-45].

2.2 Principles of Fuel Cell Modelling

A number of principles are leveraged in SOFC models, in order to simplify their solution. Many such assumptions are mentioned above including an isothermal system and uniform gas concentration. However, the ubiquitous assumption in *stack models* is that of homogenisation.

Early modelling focused on a small unit cell (Figure 2-3), allowing an analysis to be broken down into manageable components. This unit cell would be modelled in detail, and then a larger scale model could use homogenised property values for each cell. Karoliussen et al [46] demonstrated that a rigorous numerical computation of the temperature distribution in a unit cell would require a minimum of 45 nodes ($3 \times 3 \times 5$). However, by homogenising the properties within a unit cell, analysis of a complete stack layer could be made, allocating a single node for each unit cell, reducing the complexity of the problem by a factor

of 45. Further analysis showed that the accuracy of the homogenised model could be improved by the use of effective thermal conductivities, as the homogenisation assumption was found to be ill-suited to solid phase heat conduction [46].

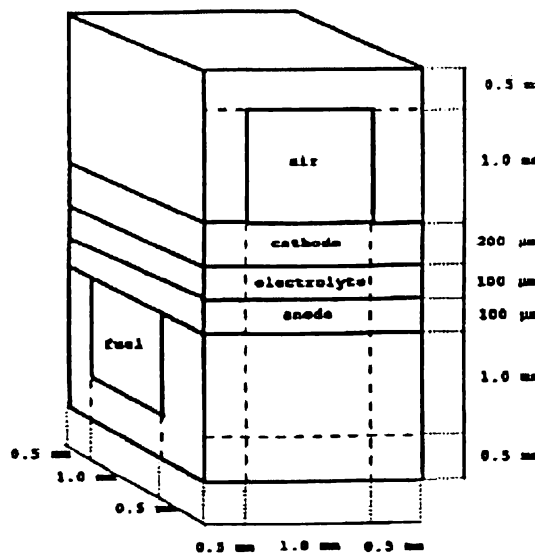


Figure 2-3 Planar cross-flow unit cell [47]

Recently, Roos et al. have developed a hierarchical model in which each tier in the hierarchy relies on homogenised data from the previous tier [48]. Denoted the “numerical volume averaging method” a detailed hierarchy is developed, from gas flow in electrode pores to heat transfer through the exterior insulation. Further work is identified in the experimental validation of the model and in mathematical justification of some of the homogenisation assumptions. One such shortcoming is the modelling of flow in the electrodes by Darcy’s law (which assumes that the driving force for flow is the pressure gradient), yet at higher levels the homogenising volumes are considered isobaric, thus negating any pressure driven flow.

2.3 Novel Fuel Cell Modelling Methods

Certain modelling methods, some of which are well established in other fields, have received little attention in the SOFC modelling literature. A number of developments have been made in the area of system identification, which matches a model to experimental data, and these are detailed below. Other methods have seen less exposure, including object based modelling, and semi-analytic methods.

Cooper et al. [44] use a technique referred to as “matched asymptotic expansions” to model a micro-tubular SOFC. The method seems to rely on mathematical assumptions to find exact solutions in certain domains, while resorting to numerical methods in other areas. The technique was stated to compare favourably with a numerical simulation, but failed to correspond to experimental data. One critical flaw was the assumption that there is no axial contribution to the cell resistivity, essentially treating the electrodes as equipotential surfaces. The obvious invalidity of this assumption (for a micro-tubular SOFC) has been demonstrated by Boersma et al. [23]. Subsequent refinements [45] added the effects of carbon deposition and removal at the anode surface but still failed to fit experimental data. In order to improve the simulation of mass flux effects, the reaction rate constants and “cell specific resistance” were modified, however this led to an extremely poor fit of the cell voltage-current characteristic. So, while this particular model failed to correspond with experimental data, the applicability of this method to SOFC modelling remains feasible.

2.3.1 Object-based Modelling

Modern software engineering is typified by object oriented programming (OOP). Key tenets of object oriented programming are the related concepts of data hiding and code reuse. Explaining these concepts requires a simple orientation to object orientated programming.

An object is essentially a collection of data, the elements of which are often called properties. A class provides the definition of a type of object, including all of the properties of the object as well as a collection of functions (methods) which act on the data. A number of unique objects can be created from a single class definition,

sharing a common set of methods but, each with their own property values. The class may also define a number of internal variables and functions which are not visible outside of the class, which is the essence of data hiding. The visible properties and methods make up the interface of the class, defining the possible interactions with objects of this type. Further, as long as the interface is preserved, the implementation of the class could be changed, optimizing a method for example, without adversely affecting programs using the class. The following example illustrates these concepts.

Let us define a class for an *electrochemical cell*. The properties of this class are the cell temperature, inlet mass flux of hydrogen, inlet mass flux of oxygen, terminal voltage, outlet mass flux of hydrogen, and outlet mass flux of oxygen; with the last two being read-only properties. For methods we will have a solve method which returns the cell current. Hidden within the class are parameters defining the cell geometry and electrochemistry. Assuming a detailed stack model is developed from a collection of *electrochemical cell* objects, this model should not need to be modified if the *electrochemical cell* class is modified, that is, if the geometry details or solution method is changed. Additionally, a range of stack models could be developed using the same *electrochemical cell* class.

Ota et al. [49] have taken the essence of object orientation and applied it to the problem of modelling a solid oxide fuel cell. While the application of object oriented programming techniques is not unique, the thoughtful definition of objects and interfaces is new to SOFC modelling. The well defined boundaries allow for extensive collaboration during the model development, potentially reducing development time significantly. Further, the requirement to have an “overall expert” is minimised, as each contributor need only understand their particular component and the interfaces (but not the details) of other components.

2.3.2 System Identification

Many modelling techniques fall under the umbrella of system identification with the essence being the correlation of a model with experimental data. Coefficients for a particular model are determined so as to minimize the error between the output of the model and a set of sampled data. By fitting the data at a number of

different system configurations, the effect of operating and/or design parameters on the model coefficients can be determined. This allows subsequent prediction by interpolation or extrapolation. As a simple example, consider a fuel cell analysed at different fuel flows and temperatures. With a steady-state electrochemical model, system identification may determine the temperature dependence of the ionic conductivity and the effect of fuel flow on potential (Nernst effect).

When combined with frequency response analysis (i.e. electrochemical impedance spectroscopy), detailed dynamic models can be developed with system identification. One such system has been used to attribute certain cell characteristics to associated electrochemical impedance spectra [50-52]. A peak-fitting distribution function was used to determine independent processes from impedance spectra [50]. The distribution function was presented as more informative than traditional equivalent circuit techniques, and analysis of some electrode processes yielded optimistic results.

2.3.2.1 State-Space Modelling

State-space modelling refers to system identification with the model expressed in the state-space formulation. The state-space formulation is commonly used in control system design and is expressed by the pair of equations 2-1, where y is the vector of outputs, u is the vector of inputs, and x is the state vector. A , B , C , and D are coefficient matrices that determine the linear system for each variable.

$$\begin{aligned}\frac{d}{dt} \mathbf{x}(t) &= \mathbf{A}\mathbf{x}(t) + \mathbf{B}\mathbf{u}(t) \\ \mathbf{y}(t) &= \mathbf{C}\mathbf{x}(t) + \mathbf{D}\mathbf{u}(t)\end{aligned}\tag{2-1}$$

Bieberle & Gauckler have applied state-space modelling to the determination of kinetic parameters at an SOFC anode [53]. Using the cell overpotential as the input and the Faradaic current as the output, the state vector is comprised of the surface concentrations of the active species and the reaction rate constants. This

model was calibrated against experimental data from a 1 cm^2 cell with a patterned anode (allowing measurement of the three-phase boundary length [54-56]).

Although the agreement between the modelled and experimental data is limited, and some of the state variables take unexpected values, this method shows great potential for simplified modelling. A particular complication that is not acknowledged is the nonlinearity introduced by the rate equation implementation. Strictly, due to the non-linear state function, this implementation is not a state-space model, but does fit the more general classification of system identification. Further, the nonlinearity significantly complicates the solution of the coefficients.

2.3.2.2 Neural Networks

More generic than the state-space model, and widely regarded as one of the most generic identification tools, artificial neural networks allow for non-linear models of arbitrary accuracy to be developed [57]. The generic nature of the neural network approach can make training of the network particularly troublesome, and a balance must be found between accuracy and solubility.

Arriagada et al. [58] developed a neural network model of an SOFC, touting excellent predictive capabilities of the neural network (most outputs show less than 1% maximum error). The primary limitation of this neural network is that the training and validation data both come from another model, a weakness which was acknowledged by the authors. However, the limited utility of the model should not detract from the fact that this was one of the first published applications of neural network simulation to a solid oxide fuel cell.

2.4 Distributed Computing and Fuel Cell Modelling

Solid oxide fuel cell modelling is still developing, as is demonstrated by the literature. While some of the basic principles are shared, the models themselves still vary widely, with very little comparison being possible between models. Numerical simulations still have a major role to play in the developing realm of fuel cells, providing design insights and enabling rapid prototyping techniques.

In the wider world of modelling, distributed computing has not really advanced beyond the concepts of parallel and symmetric multi-processing. Except for a small collection of problems requiring enormous levels of computation on disconnected data sets (e.g. finding prime numbers, or alien intelligence), the potential of distributed computing remains untapped. The modular nature of fuel cells, with multiple identical sub-assemblies seems well suited to the application of distributed techniques.

2.5 References

1. Debenedetti, P. G. & Vayenas, C. G. Steady-state analysis of high temperature fuel cells. *Chemical Engineering Science* **38**, 1817-1829 (1983).
2. Michaels, J. N., Vayenas, C. G. & Hegedus, L. L. *Journal of the Electrochemical Society* **133**, 522-525 (1986).
3. Yang, Y., Debenedetti, P. G., Britt, H. & Vayenas, C. G. in *International symposium on process systems engineering* 28-40 (Kyoto, 1982).
4. Vayenas, C. G. & Hegedus, L. L. *Industrial Engineering Chemistry Fundamentals* **24**, 316-324 (1985).
5. Yentekakis, I. V., Neophytides, S., Seimanides, S. & Vayenas, C. G. in *2nd International Symposium on SOFCs* (eds. Grosz, F., Zegers, P., Singhal, S. C. & Yamamoto, O.) 281-288 (Commission of the European Communities, Athens, 1991).
6. Suwanwarangkul, R., Croiset, E., Fowler, M. W., Douglas, P. L., Entchev, E. & Douglas, M. A. Performance comparison of Fick's, dusty-gas and Stefan-Maxwell models to predict the concentration overpotential of a SOFC anode. *Journal of Power Sources* **122**, 9-18 (2003).
7. Chan, S. H., Chen, X. J. & Khor, K. A. An electrolyte model for ceramic oxygen generator and solid oxide fuel cell. *Journal of Power Sources* **111**, 320-328 (2002).
8. Chan, S. H., Chen, X. J. & Khor, K. A. A simple bilayer electrolyte model for solid oxide fuel cells. *Solid State Ionics* **158**, 29-43 (2003).
9. Arato, E. & Costa, P. in *2nd International Symposium on SOFCs* (eds. Grosz, F., Zegers, P., Singhal, S. C. & Yamamoto, O.) 273-280 (Commission of the European Communities, Athens, 1991).
10. Costamagna, P. & Arato, E. in *1st European SOFC Forum* (ed. Bossel, U.) 287- (Lucerne, 1994).

11. Achenbach, E. & Reus, U. in *Solid Oxide Fuel Cells (SOFC VI)* (eds. Singhal, S. C. & Dokya, M.) 1125-1134 (The Electrochemical Society, Honolulu, 1999).
12. Achenbach, E., Bleise, C. & Divisek, J. in *4th International Symposium on SOFCs* 1095-1104 (Yokohama, 1995).
13. Achenbach, E. in *1st European SOFC Forum* (ed. Bossel, U.) 337- (Lucerne, 1994).
14. Neophytides, S. & Tripakis, A. in *1st European SOFC Forum* (ed. Bossel, U.) 307- (Lucerne, 1994).
15. Melhus, O. & Ratkje, S. K. in *4th International Symposium on SOFCs* 1123- (Yokohama, 1995).
16. Petrucci, L., Cocchi, S. & Fineschi, F. A global thermo-electrochemical model for SOFC systems design and engineering. *Journal of Power Sources* **118**, 96-107 (2003).
17. Achenbach, E. Three-dimensional and time-dependent simulation of a planar solid oxide fuel cell stack. *J. Power Sources* **49**, 333- (1994).
18. Nagata, S., Momma, A., Kato, T. & Kasuga, Y. Numerical analysis of output characteristics of tubular SOFC with internal reformer. *Journal of Power Sources* **101**, 60-71 (2001).
19. Aguiar, P., Chadwick, D. & Kershenbaum, L. Modelling of an indirect internal reforming solid oxide fuel cell. *Chemical Engineering Science* **57**, 1665-1677 (2002).
20. Haynes, C. & Wepfer, W. J. 'Design for power' of a commercial grade tubular solid oxide fuel cell. *Energy Conversion and Management* **41**, 1123-1139 (2000).
21. Hatchwell, C. E., Sammes, N. M. & Kendall, K. Cathode current-collectors for a novel tubular SOFC design. *Journal of Power Sources* **70**, 85-90 (1998).
22. Hatchwell, C., Sammes, N. M., Brown, I. W. M. & Kendall, K. Current collectors for a novel tubular design of solid oxide fuel cell. *Journal of Power Sources* **77**, 64-68 (1999).
23. Boersma, R. J., Sammes, N. M. & Fee, C. J. Losses resulting from in-plane electricity conduction in tubular solid oxide fuel cells. *Solid State Ionics* **135**, 493-502 (2000).
24. Li, P.-W. & Chyu, M. K. Simulation of the chemical/electrochemical reactions and heat/mass transfer for a tubular SOFC in a stack. *Journal of Power Sources* **124**, 487-498 (2003).

25. Aguiar, P., Chadwick, D. & Kershenbaum, L. Effect of methane slippage on an indirect internal reforming solid oxide fuel cell. *Chemical Engineering Science* **59**, 87-97 (2004).
26. Walters, K. M., Dean, A. M., Zhu, H. & Kee, R. J. Homogeneous kinetics and equilibrium predictions of coking propensity in the anode channels of direct oxidation solid-oxide fuel cells using dry natural gas. *Journal of Power Sources* **123**, 182-189 (2003).
27. Herbstritt, D., Weber, A. & Ivers-Tiffée, E. Modelling and DC-polarisation of a three dimensional electrode/electrolyte interface. *Journal of the European Ceramic Society* **21**, 1813-1816 (2001).
28. Virkar, A. V., Chen, J., Tanner, C. W. & Kim, J.-W. The role of electrode microstructure on activation and concentration polarizations in solid oxide fuel cells*1. *Solid State Ionics* **131**, 189-198 (2000).
29. Chan, S. H. & Xia, Z. T. Anode micro model of solid oxide fuel cell. *Journal of the Electrochemical Society* **148**, A388-A394 (2001).
30. Chan, S. H., Khor, K. A. & Xia, Z. T. A complete polarization model of a solid oxide fuel cell and its sensitivity to the change of cell component thickness. *Journal of Power Sources* **93**, 130-140 (2001).
31. Hartvigsen, J., Elangovan, S. & Khandkar, A. in *3rd International Symposium on SOFCs* (eds. Singhal, S. C. & Iwahara, H.) 878- (Honolulu, 1993).
32. Bleise, C., Divisek, J., Steffen, B., König, U. & Schultze, J. W. in *3rd International Symposium on SOFCs* (eds. Singhal, S. C. & Iwahara, H.) 861- (Honolulu, 1993).
33. Ferguson, J. R. in *2nd International Symposium on SOFCs* (eds. Grosz, F., Zegers, P., Singhal, S. C. & Yamamoto, O.) 305-312 (Commission of the European Communities, Athens, 1991).
34. Arato, E. & Costa, P. 6- (Swiss Federal Office of Energy, Berne, 1992).
35. Solheim, A. in *3rd International Symposium on SOFCs* (eds. Singhal, S. C. & Iwahara, H.) 841 (Honolulu, 1993).
36. Nisancioglu, K., Karoliussen, H. & Ødegård, R. in *1st European SOFC Forum* (ed. Bossel, U.) 249- (Lucerne, 1994).
37. Koeppen, J. & Winkler, W. in *2nd European SOFC Forum* 247- (Oslo, 1996).
38. Tanner, C. W. & Virkar, A. V. A simple model for interconnect design of planar solid oxide fuel cells. *Journal of Power Sources* **113**, 44-56 (2003).

39. Takehara, Z., Kanamura, K., Hirano, A. & Ipponmatsu, M. in *2nd International Symposium on SOFCs* (eds. Grosz, F., Zegers, P., Singhal, S. C. & Yamamoto, O.) 313- (Commission of the European Communities, Athens, 1991).
40. Campanari, S. & Iora, P. Definition and sensitivity analysis of a finite volume SOFC model for a tubular cell geometry. *Journal of Power Sources* **132**, 113-126 (2004).
41. Lockett, M., Simmons, M. J. H. & Kendall, K. CFD to predict temperature profile for scale up of micro-tubular SOFC stacks. *Journal of Power Sources* **131**, 243-246 (2004).
42. Boersma, R. J., Sammes, N. M. & Fee, C. in *Solid Oxide Fuel Cells (SOFC VI)* (eds. Singhal, S. C. & Dokiya, M.) 1109-1124 (The Electrochemical Society, Honolulu, 1999).
43. Foster, R. E., Sammes, N. M. & Fenton, B. in *Solid Oxide Fuel Cells (SOFC VI)* (eds. Singhal, S. C. & Dokiya, M.) 1078-1086 (The Electrochemical Society, Honolulu, 1999).
44. Cooper, R. J., Billingham, J. & King, A. C. Flow and reaction in solid oxide fuel cells. *Journal of Fluid Mechanics* **411**, 233-262 (2000).
45. King, A. C., Billingham, J. & Cooper, R. J. Performance modelling of solid oxide fuel cells. *Combustion Theory and Modelling*, 639-667 (2001).
46. Karoliussen, H., Nisancioglu, K. & Solheim, A. Estimation and use of Effective conductivities for Heat Transfer Calculations in a SOFC. *Unknown Resource*, 245-.
47. Bossel, U. G. (Swiss Federal Office of Energy, Berne, 1992).
48. Roos, M., Batawi, E., Harnisch, U. & Hocker, T. Efficient simulation of fuel cell stacks with the volume averaging method. *Journal of Power Sources* **118**, 86-95 (2003).
49. Ota, T., Koyama, M., Wen, C.-j., Yamada, K. & Takahashi, H. Object-based modeling of SOFC system: dynamic behavior of micro-tube SOFC. *Journal of Power Sources* **118**, 430-439 (2003).
50. Müller, A., Schichlein, H., Feuerstein, M., Weber, A., Krügel, A. & Ivers-Tiffée, E. in *Solid Oxide Fuel Cells (SOFC VI)* (eds. Singhal, S. C. & Dokiya, M.) 925-931 (The Electrochemical Society, Honolulu, 1999).
51. Schichlein, H., Feuerstein, M., Müller, A., Weber, A., Krügel, A. & Ivers-Tiffée, E. in *Solid Oxide Fuel Cells (SOFC VI)* (eds. Singhal, S. C. & Dokiya, M.) 1069-1077 (The Electrochemical Society, Honolulu, 1999).

52. Schichlein, H., Müller, A. C., Voigts, M., Krügel, A. & Ivers-Tiffée, E. Deconvolution of electrochemical impedance spectra for the identification of electrode reaction mechanisms in solid oxide fuel cells. *Journal of Applied Electrochemistry* **32**, 875-882 (2002).
53. Bieberle, A. & Gauckler, L. J. State-space modeling of the anodic SOFC system Ni, H₂-H₂O|YSZ. *Solid State Ionics* **146**, 23-41 (2002).
54. Mizusaki, J., Tagawa, H., Saito, T., Yamamura, T., Kamitani, K., Hirano, K., Ehara, S., Takagi, T., Hikita, T., Ippommatsu, M., Nakagawa, S. & Hashimoto, K. Kinetic studies of the reaction at the nickel pattern electrode on YSZ in H₂---H₂O atmospheres. *Solid State Ionics* **70-71**, 52-58 (1994).
55. Bieberle, A. & Gauckler, L. J. Reaction mechanism of Ni pattern anodes for solid oxide fuel cells. *Solid State Ionics* **135**, 337-345 (2000).
56. Bieberle, A., Meier, L. P. & Gauckler, L. J. The Electrochemistry of Ni Pattern Anodes Used as Solid Oxide Fuel Cell Model Electrodes. *Journal of the Electrochemical Society* **148**, A646-A656 (2001).
57. Hagan, M. T., Demuth, H. B. & Beale, M. H. *Neural Network Design* (PWS, Boston, MA, 1996).
58. Arriagada, J., Olausson, P. & Selimovic, A. Artificial neural network simulator for SOFC performance prediction*1. *Journal of Power Sources* **112**, 54-60 (2002).

3 Feasibility of Distributed Computing for Fuel Cell Modelling

Distributed computing has been applied to some of the most computationally intensive problems known. Detailed fuel cell stack models are currently limited in their scope due to the overwhelming complexity of detailed simulation. In this work a model process is developed that is representative of a fuel cell stack electrochemical model, and is solved in a distributed computing framework. Solution time for the problem is shown to scale well as additional computers are added to the framework.

3.1 Why Distributed Computing?

Development of fuel cell systems often relies on detailed analysis of the fuel cell's electrical and thermal characteristics. Comprehensive modelling of these features requires levels of computational power unavailable to most developers. Due to this restriction on available computational resources, analysts are forced to restrict their models. For example, an analysis of thermal stresses within a Solid Oxide Fuel Cell (SOFC) stack restricted the analysis domain to a single cell channel [1]. Similarly, a model of load response for a PEM (Polymer Electrolyte Membrane) stack was based on constraining the stack to a single non-linear system [2]. The assumptions made in these models do not preclude their usefulness in understanding the systems under analysis, but models cannot provide insight into processes obfuscated by assumptions. Moreover, examining a different aspect of the system would often require a new model to be developed.

A number of analysts of similarly complex problems are turning to distributed computing to analyze their systems [3-5]. Distributed computing is the process of analyzing data using the resources of multiple computers. One of the primary limitations of distributed computing is that the problem must be able to be constructed as a number of relatively independent sub-problems. Due to the

modular arrangement of fuel cell stacks, it is possible to develop a model for deployment in a distributed computing framework, such as is described herein.

3.2 Software Implementation

As a demonstration of the benefits (and applicability) of distributed computing to the solution of fuel cell stack models, a simple model is developed here and tested in a network environment. The model is not intended to accurately represent a particular fuel cell, nor is the solution method intended to be optimal. The model encompasses the electrical and electrochemical aspects of a SOFC, including gas depletion, and temperature variation. The simplicity of the cell model makes it insensitive to geometry (planar or tubular) and electrode orientation. Where it aids description, an anode-inside tubular design is considered for the purposes of visualization.

3.2.1 User Interface and Model Structure

An application was developed in Microsoft Visual Basic to provide a basic user interface and to allow for simple networking. A preliminary user interface is shown in Figure 3-1, with solution progress in the left pane, debug information in the right pane, and basic solution parameters collected in the upper right corner. Further details of the user interface will be given below.

The cell model implemented for this proof of concept is a one-dimensional resistive ladder network, as shown in Figure 3-2, wherein a single element is delineated by the dashed bounding box. Within each element the Nernst potential is calculated at the inlet node of the element (equations 3-1 and 3-2). The current from the element is determined by the difference between the Nernst potential (E_N) and the cell voltage (E_{cell}), using Ohm's law, as shown in equation 3-3. It should be noted that the V-I characteristic for this cell is perfectly linear, as the cell is modelled as a pure resistance, with some temperature dependence allowed. Current collection is assumed to be ideal, so no voltage drop is considered in the electrodes. Thus, the same cell voltage is impressed at each element.

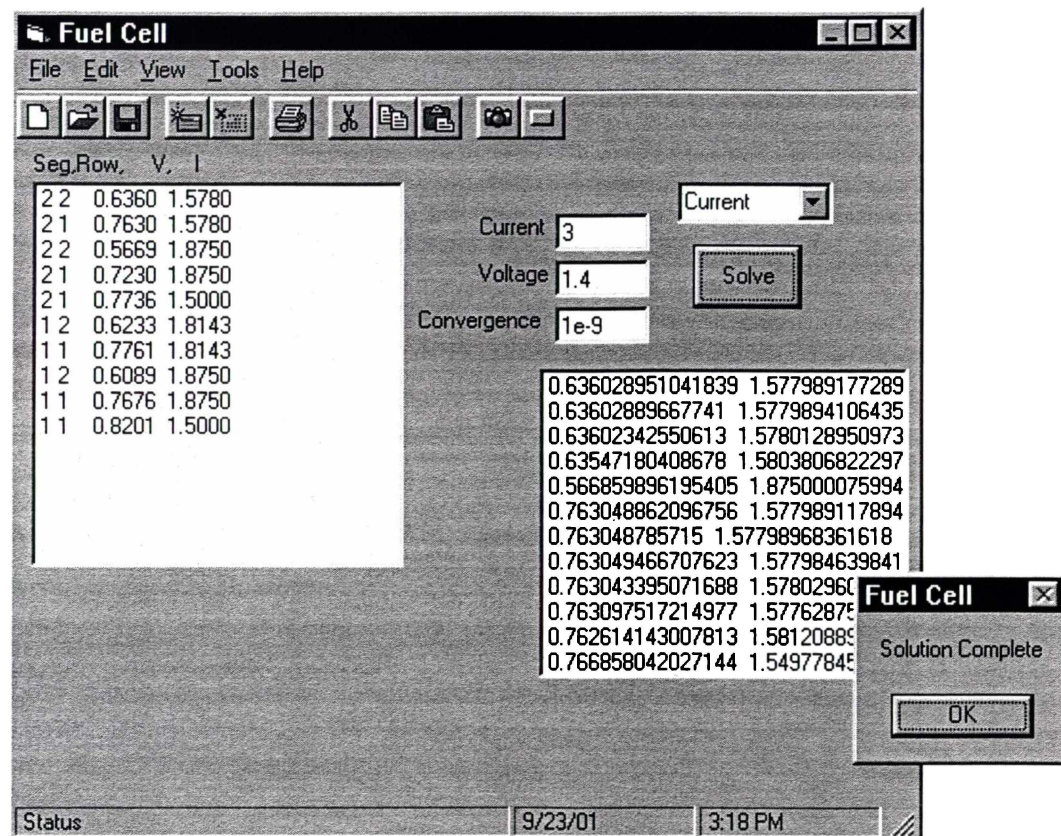


Figure 3-1 User interface for a local solution

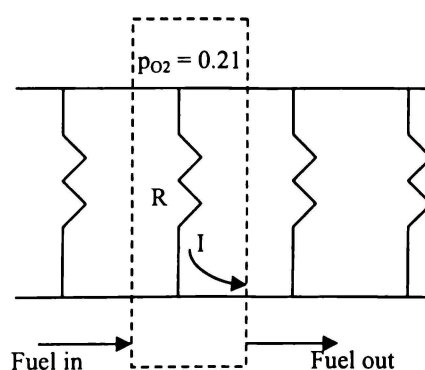


Figure 3-2 A ladder network element

Consumption of fuel gases (ϕ - mol.s⁻¹) is calculated from the current (I) produced in the element, using Faraday's law (equation 3-4), with the restriction that the

Nernst potential due to each active system must be equal at the element outlet node. With the assumption that an element is isobaric, and isothermal, and given that the oxygen partial pressure is considered constant, the partial pressures can be rendered as molar flux quantities (χ). Equating the Nernst potentials then gives equation 3-5, which can be rearranged to a quadratic expression in ϕ_{H_2} , as shown in equation 3-6. Completing the square gives two possible hydrogen fluxes, the most likely solution being the smallest change.

$$E_{N,H_2} = 1.271 - 2.75 \times 10^{-4} T - \frac{RT}{2F} \ln \left(\frac{p_{H_2O}}{p_{H_2} p_{O_2}^{0.5}} \right) \quad (3-1)$$

$$E_{N,CO} = 1.468 - 4.52 \times 10^{-4} T - \frac{RT}{2F} \ln \left(\frac{p_{CO_2}}{p_{CO} p_{O_2}^{0.5}} \right) \quad (3-2)$$

$$E_N - E_{cell} = IR \quad (3-3)$$

$$\phi = \frac{I}{2F} = \phi_{H_2} + \phi_{CO} \quad (3-4)$$

$$1.77 \times 10^{-4} T - 0.197 = \frac{RT}{2F} \ln \left[\frac{(\chi_{H_2O} + \phi_{H_2})(\chi_{CO} - \phi + \phi_{H_2})}{(\chi_{H_2} - \phi_{H_2})(\chi_{CO_2} + \phi - \phi_{H_2})} \right] \quad (3-5)$$

$$\begin{aligned}
 0 &= A\phi_{H_2}^2 + B\phi_{H_2} + C \\
 A &= 1 - e^D \\
 B &= \chi_{H_2O} + \chi_{CO} - \phi + (\chi_{H_2} + \chi_{CO_2} + \phi)e^D \\
 C &= \chi_{H_2O}(\chi_{CO} - \phi) - \chi_{H_2}(\chi_{CO_2} + \phi)e^D \\
 D &= \frac{2F}{R} \left(1.77 \times 10^{-4} - \frac{0.197}{T} \right)
 \end{aligned} \tag{3-6}$$

Three levels of stack interconnection are provided and an options screen allows for user configuration thereof (Figure 3-3). First, a row of cells are electrically connected in parallel, sharing a common fuel source. Second, a segment is a collection of rows which can be specified to be connected in electrical series or parallel. Finally, a stack is a collection of segments, where the fuel inlet to a cell in the segment is the outlet of the corresponding cell in the previous segment. The segments making up a stack can be specified to be connected in series or parallel. The sub-stack geometry illustrated in Figure 3-4 shows two segments per tube, and four tubes per row. A number of these rows could be stacked together to form a fuel cell stack with two electrical outputs (one per segment). Segment outputs can then be connected in parallel or series. In planar stack terminology, a cell could correspond to a single channel, a row to a plate, a segment to a sub-stack, and multiple segments would correlate to a number of sub-stacks with gas flows connected channel by channel (no mixing between substacks). Figure 3-3 shows that the number of segments can be changed, and cell lengths specified for each segment, or a uniform length applied to each segment. While tube diameter (in mm) is specified, a planar geometry could be simulated by scaling this input by $1/\pi$.

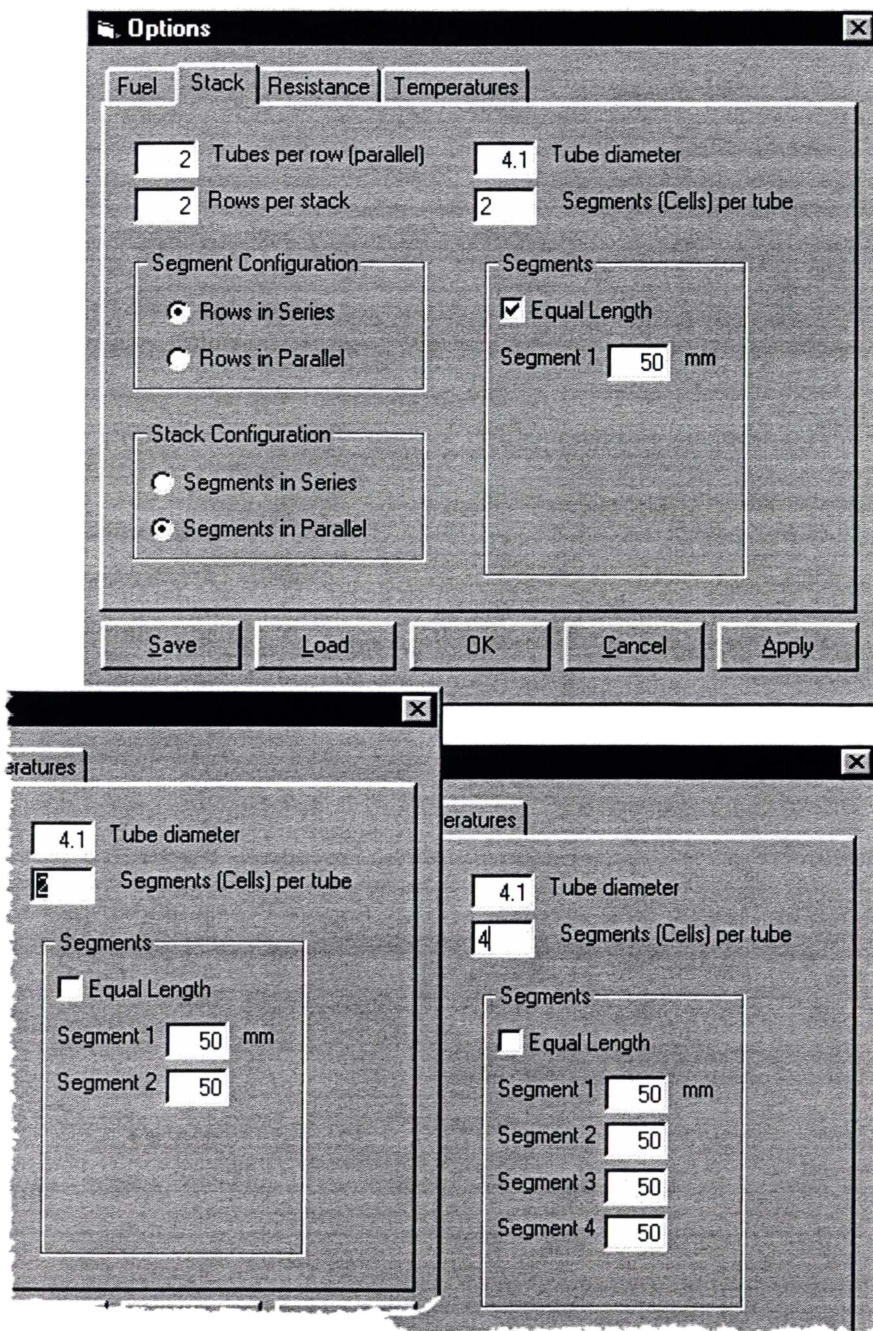


Figure 3-3 Stack configuration options

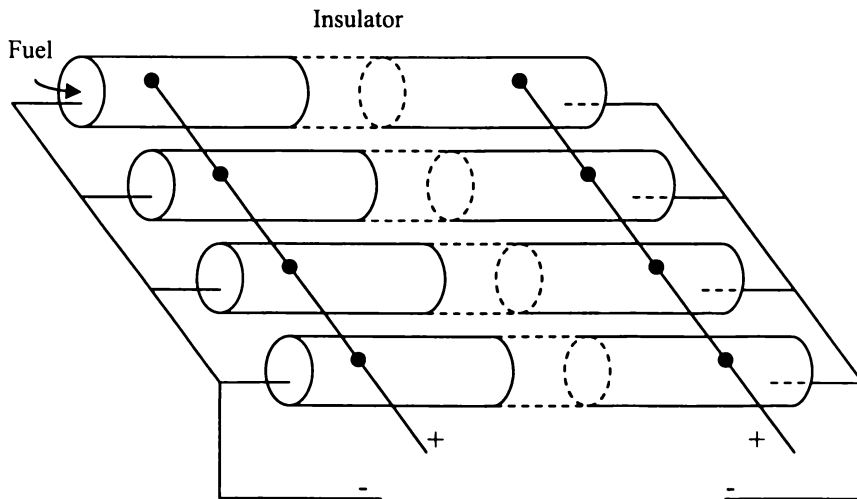


Figure 3-4 Modelled cell interconnection

Remembering that the cell structure is modelled as a resistive element, the temperature dependence of the resistance is accounted for by equation 3-7, where the coefficients can be specified through the user interface. Equation 3-7 also provides an Arrhenius term for the ionic conductivity of the electrolyte [6].

$$R = Ae^{\frac{B}{T}} + C + DT \quad (3-7)$$

Heat generation and transfer are not considered, in order to keep the model simple. Temperature is specified at the inlet, midpoint, and outlet of the tube, and at multiple verticals in the stack, as shown in Figure 3-5. Local temperature is linearly interpolated from the specified points. The number of vertical points can be changed and updated similar to the segment method shown in Figure 3-3. The $3 \times 3 \times 3$ arrangement displayed on the temperature map allows for a limited three-dimensional temperature field, and allows for temperature distributions to be input from a well-instrumented test stack.

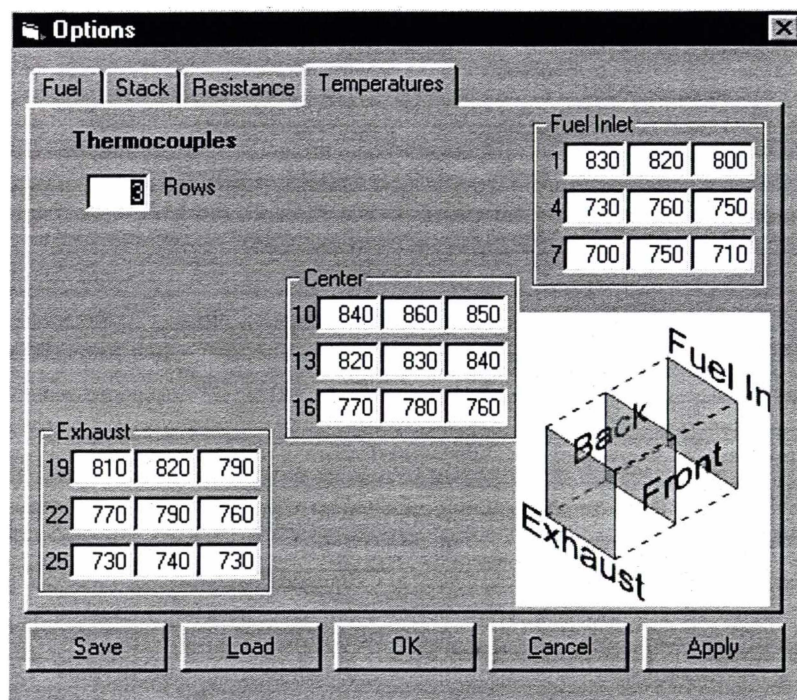


Figure 3-5 Stack temperature profile

Fuel for the stack is specified as a methane-air mixture and is assumed to be fully pre-reformed at the entry to the cell. The oxygen to carbon (O:C) ratio must be such that no methane, but some hydrogen remains in the stream. Specifically, the O:C ratio must lie in the range $0.5 \leq O : C < 2.0$. Values outside these limits will cause an error to be displayed during solution initialization and the task will be aborted. The air side of the fuel cell does not consider depletion and fixes the oxygen mole fraction at 0.21. Fuel configuration parameters are shown in Figure 3-6, including some parameters that are not implemented (e.g. cathode air flow, Hydrogen fuel). Air and fuel mixture parameters for the partial oxidation precursors can be specified in a number of ways. O:C Ratio can be expressed as oxygen:fuel or air:fuel. Fuel consumption can be determined in one of three ways; fixed fuel utilization, fixed fuel flow, and fixed fuel and air flows. Fixed utilization adds an outer iteration to the solution for utilization convergence and ignores the inputs for fuel and air flows instead determining these values from the O:C ratio and the estimated current. Fixed fuel flow, ignores the utilization and air entries, calculating air flow from the O:C ratio. Finally, fixed fuel and air flows

ignores the utilization and O:C ratio inputs but back calculates the O:C ratio for display purposes.

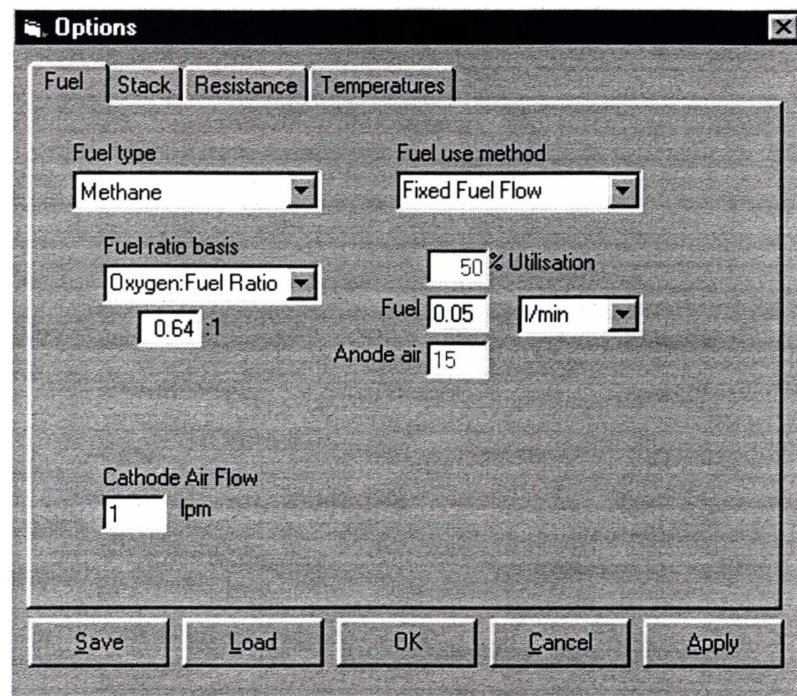


Figure 3-6 Fuel configuration options

Figure 3-7 provides a flowchart overview of the solution process for a row of cell segments (the segments are solved individually). In a distributed arrangement, the solution described in Figure 3-7 is executed at each client, as directed by a main server application.

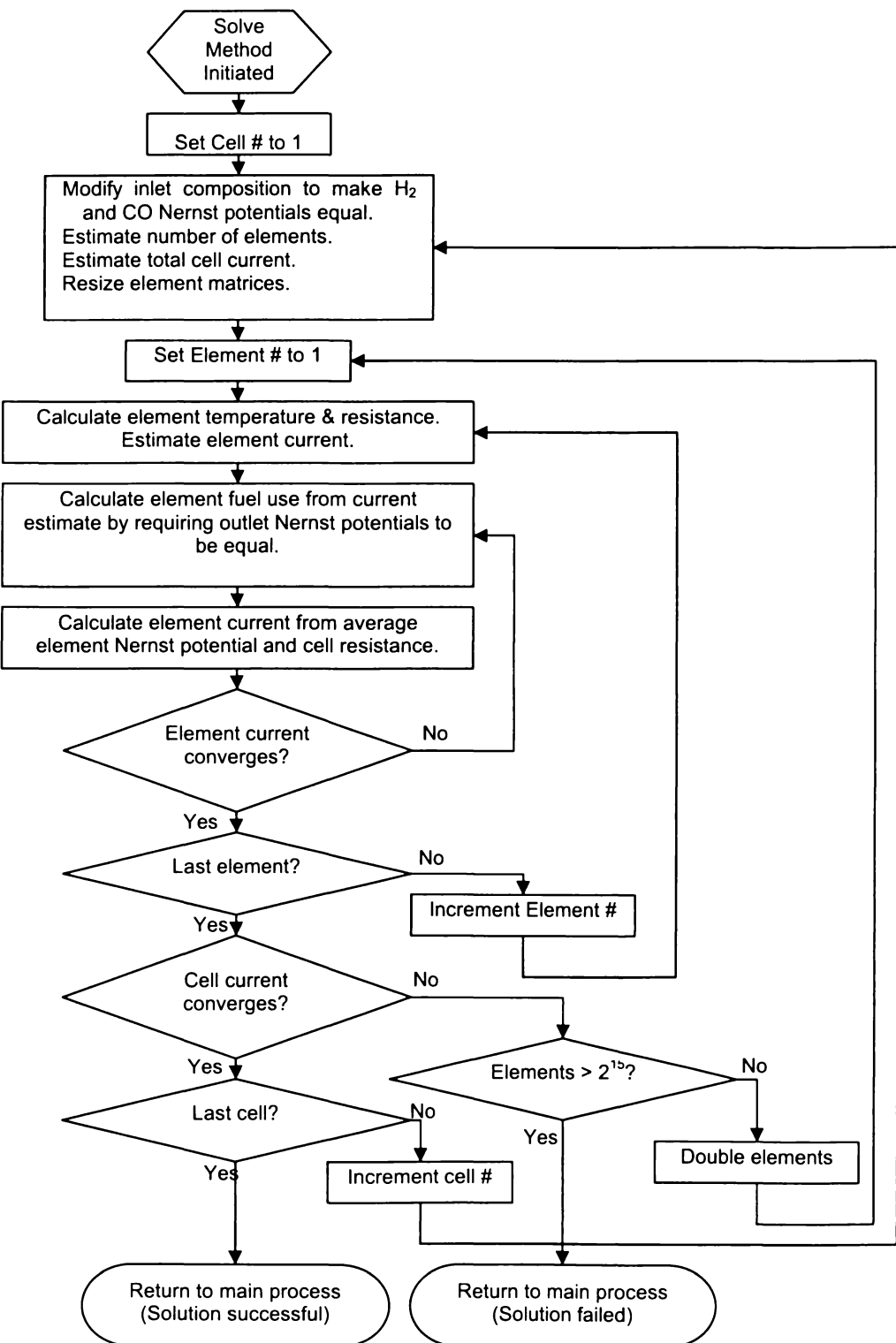


Figure 3-7 Cell solution flowchart

Progress of a simple solution using a local version can be tracked in Figure 3-1. Above the ‘Solve’ button is a drop-down box, which allows for the selection of dependant variable. At the commencement of a solution, the value entered for the dependant variable is used as the initial guess for that parameter (current of 3 A in Figure 3-1), while the value of the independent variable (stack voltage of 1.4 V) is the bounding criterion. The solution shown is for a stack with two rows connected in series, and two segments connected in parallel. The initial guess of 3 Amps is divided between the two segments, and the first row solution is shown at the bottom of the left pane (Figure 3-1). The two rows making up this segment are then solved, with iterative updates to the current, until the voltage for the segment reaches the required value of 1.4 V ($0.7761 + 0.6233$). The solution of the second segment then proceeds in the same fashion, yielding a final current of $1.81 + 1.58 = 3.39$ Amps. The row voltages come out at $0.78 + 0.62$ for the first segment, and $0.76 + 0.64$ for the second. Voltage differences in a segment can be accounted for by the temperature map in Figure 3-5, and the current differences are additionally related to fuel depletion.

Processing requirements for this system are presented as a reasonable approximation to the processing requirements of a full-stack electrochemical model. The solution of the cell entities requires the bulk of the processing, with a small amount of processing in outer iterations to ensure consistency of the overall solution.

3.2.2 Client-Server Development

In a client-server scenario, the server application sends information to the client describing the cells to be solved including; number of cells, length of cells, temperature profile, inlet gas composition, and required cell current or voltage. The client software, in turn, processes the solution and returns the outlet gas composition and output current and voltage. Elementary interactions of the client and server software, during operation, can be gleaned from Figure 3-8 and Figure 3-9.

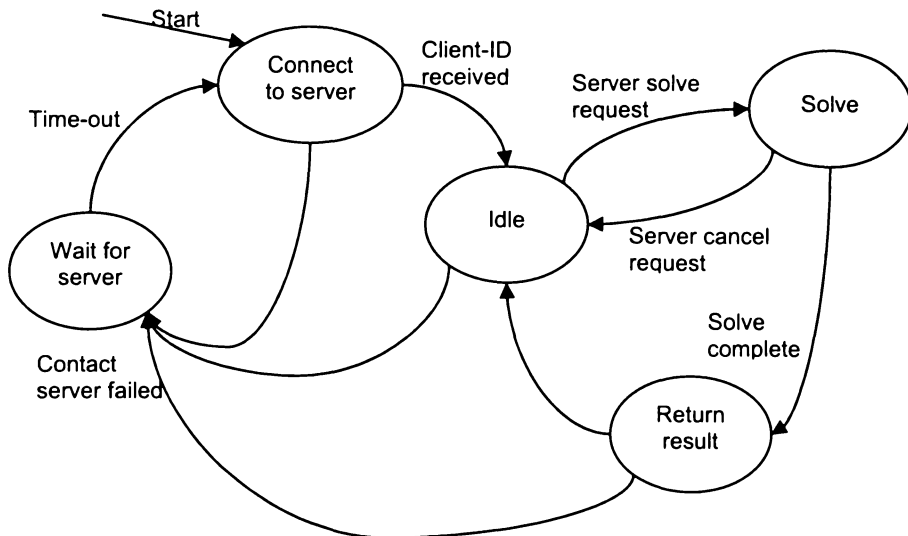


Figure 3-8 Client state machine

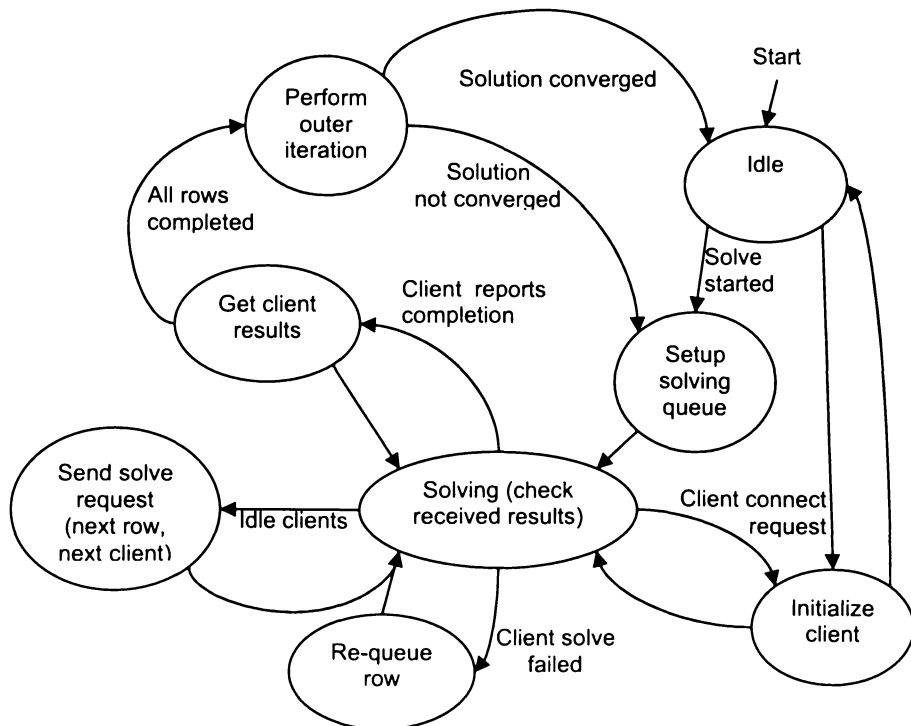


Figure 3-9 Server state machine

In addition to the passing of data and instructions back and forth, initialization, scheduling and tracking need to be implemented. First and foremost, the server application needs to define a “remote access object” so that clients can access it across the network. Common methods of implementing remote communications are the CORBA model (Common Object Request Broker Architecture) and, in Microsoft environments, DCOM (Distributed Component Object Model). In a Microsoft Visual Basic environment, setting up remote access (via DCOM) is relatively transparent to the programmer, but requires additional configuration during deployment.

The server application allows for the remote creation of a connection object. This connection object allows clients to connect to the server’s own control object (indirectly) while still maintaining their own unique reference to the server. Thus multiple clients, each with their own connection object (on the server), can communicate with the single server object. When a client first connects to the server, the client attempts to create a connection object. If this creation is successful it can then connect to the shared server object and, during the process, the server has also created a reference to the client object. Two significant impediments to this implementation are:

1. The client must know the server, that is, the client must have the address of the server machine to connect to.
2. Both the client and server must have prior knowledge of the other’s object class when the application is built.

The “prior knowledge” requirement causes a chicken-egg type of problem, in that neither application can be built without a complete copy of the others classes (code). In addition, the server needs to be able to connect to multiple instances of the client object, and some of these objects need to be on different computers. Furthermore, any changes in either application requires that both applications be rebuilt. Circumventing this in Visual Basic requires a public abstract class which, in essence, is a definition of the interface provided by an object (in object oriented programming this is referred to as polymorphism). The abstract class (which will

never change) can then be stored in a “type library” or dynamically linked library (dll). This way, when changes are made to the client application, the server need not be rebuilt, as the abstract class (by which the server understands the client) has not changed. By including the abstract client class, the server has knowledge of the interface to the clients, while the client software is responsible for *implementing* the interface (fleshing out the details). Conversely, the client has access to the server through a similar abstract interface. For example, the client interface has a solve method, which the server calls when it has data for the client to process. The server has no knowledge of how the client will actually process the data, but trusts that each client will produce the same results. The server will be oblivious to the existence of multiple different client implementations.

These connections allow the server application to send and receive data from clients, and for the client to notify the server of its status. The server application keeps queues of idle clients, busy clients and clients awaiting server response. Ideally the last of these queues should be empty; however, every client enters this list when it completes a solution. In order to avoid communication timeout problems, the server will respond to notifications at the highest priority. Conversely, the server may be processing high priority data at the time a notification comes in and does not wish to deal with communications immediately. To balance these two needs, when a notification is received from a client, the server acknowledges the notification, places it in the queue, and returns to the task that was interrupted. When the server completes the task at hand it can process the queues. This method, commonly referred to as an asynchronous callback function, can introduce some client idle time, but is necessary in the instance of simultaneous client notifications. An asynchronous call-back is also used for the client’s solve function, so that the server is not blocked during client processing. That is, when the server calls the client’s solve function, the client sets a flag that it needs to process the data, but then returns from the solve function. Once the solve function has returned, the server has confirmation that the client received the message, and can continue with its other tasks. Meanwhile, the client starts processing the data and, when complete, notifies the server of the completion.

3.3 Initial Distributed Model Performance.

As the cell model is far from ideal, single client results are dispensed with. A model with three rows of tubes, with four tubes in each row and two cells on each tube, was run on up to five computers (one as server), with the results shown in Figure 3-10. The basic computer was configured with a Celeron CPU at 700 MHz and 128 MB of RAM. The problem scales well with up to four clients, even though a maximum would be expected at three clients (one per row of tubes). Overhead on Figure 3-10 shows the time not spent on the clients, and is made up of server processing, communications, and client management. The ‘perfect scaling’ curve is derived from the result for a local only solution, and determines the overhead for the one client case. The fact that overhead increases linearly with the number of clients suggests a far from optimal networking scheme. However, the scaling of solution time bespeaks the potential of this style of application in the solution of fuel cell simulations.

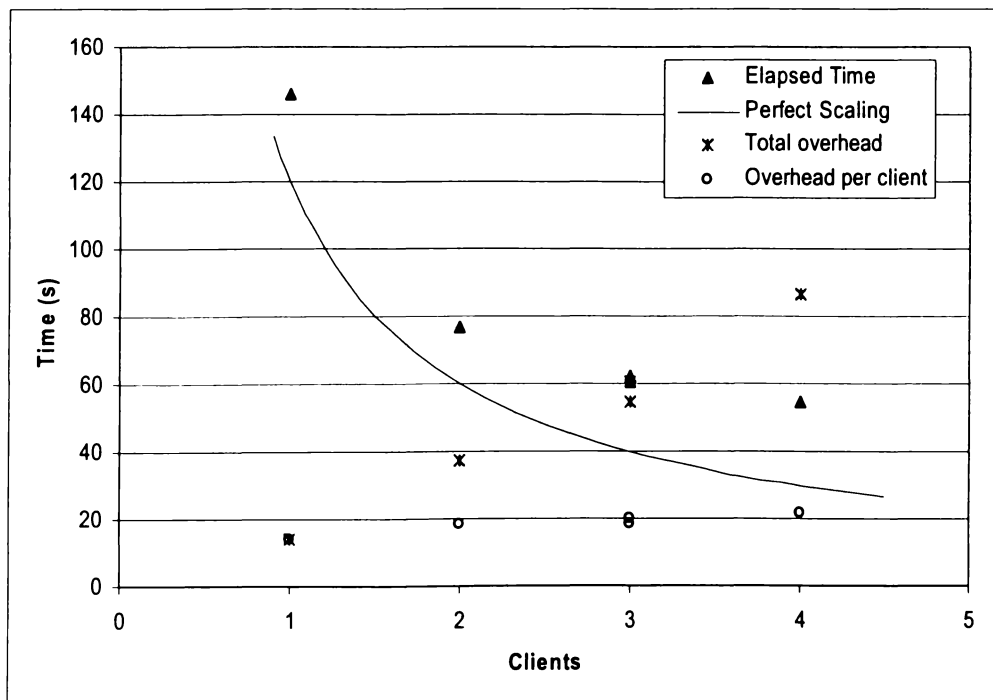


Figure 3-10 Client scaling for three row stack.

3.4 Further Work

A demonstration has been given of the application of distributed computing techniques, to a problem representative of a fuel cell stack model. The fuel cell problem scales well with the addition of basic clients, showing its suitability to distributed techniques. Further distributed modelling is detailed in chapter 6 with the detailed finite element cell model developed in chapters 4 & 5.

3.5 References

1. Yakabe, H., Ogiwara, T., Hishinuma, M. & Yasuda, I. 3-D model calculation for planar SOFC. *Journal of Power Sources* **102**, 144-154 (2001).
2. Yerramalla, S., Davari, A., Feliachi, A. & Biswas, T. Modeling and simulation of the dynamic behavior of a polymer electrolyte membrane fuel cell. *Journal of Power Sources* **124**, 104-113 (2003).
3. Anderson, D. in *Bioastronomy 99: A New Era in Bioastronomy* (eds. Lemarchand, G. & Meech, K.) 511 (Astronomical Society of the Pacific: San Francisco, 1999).
4. Website, Distributed Computing Technologies Inc.,
<http://www.distributed.net/>
5. Website, The Great Internet Mersenne Prime Search, <http://mersenne.org/>
6. Bossel, U. G. in *Final Report on SOFC Data* (International Energy Agency, Berne, 1992).

4 Finite Element Model – Description & Validation

Modelling of an anode supported tubular solid oxide fuel cell with a commercial finite element modelling tool is described. An isothermal model for fluid flow, diffusion, and electrochemical effects is developed. Results for operation on hydrogen are presented for a selection of cells, and are shown to be comparable to experimental results. Design variations are proposed, modelled, and compared with initial experimental results. Geometric variations are reasonably well accounted for, however, the isothermal model will be examined for replacement with a more detailed thermal treatment.

4.1 Model Description

Finite element modelling (FEM) is undertaken to determine optimal design parameters for a tubular fuel cell. The design under consideration is an anode supported tubular design, wherein the anode cermet (ceramic-metal composite) is relied upon to collect current from the cell. As electrical power increases with length, the number of cells required to provide a specified stack power decreases as the length of the tubes is increased. However, as length increases current collection losses increase. Initial work, herein, is directed at the validation of the model against experimental data.

The FEM model is undertaken with the commercial modelling software Femlab®, which is an add-on package to the widely used Matlab® suite. Femlab provides a useful graphical development environment, and access to lower level scripting through Matlab. Matlab handles most of the matrix manipulation, with Femlab

[®] Femlab is a registered trademark of Comsol, further information is available at www.femlab.com.

[®] Matlab is a registered trademark of The Mathworks, further information is available at www.mathworks.com.

contributing a few “helper-functions” specific to FEM analysis. One of the particular advantages of Femlab is the ease with which solution systems can be coupled and decoupled, a specific example of which is discussed below.

4.1.1 Geometry

The tube is modelled as an axisymmetric section, comprised of three sub-domains, as shown in Figure 4-1. The first sub-domain represents the gas stream, and requires the solution of both a momentum balance and a mass balance. Sub-domain two represents the porous anode cermet and encompasses mass-transfer and electrical effects. Finally, the third sub-domain represents the metallic cathode current collection and only includes electrical effects. The modelled cathode current collector geometry is much thicker than the physical object to allow a mesh of reasonable density to be created, and this thickening is accounted for in the electrical model. Electrochemical effects are applied as boundary coefficients in the anode mass transfer equations so the electrolyte layer is accounted for in this boundary. The mass balance solution must be continuous between the first and second sub-domains. The electrical solutions, however, are disparate and have an enforced discontinuity (accounting for electrochemical effects) at the shared boundary.

Cathodic oxidant concentration is assumed to be constant due to the condition that cathode gas flow exceeds the stoichiometric requirement by a factor of no less than 3 and, more typically, 50. Oxygen diffusion in the cathode is also neglected in this model as cathode diffusion related losses have been shown to be insignificant at moderate currents [1]. As this model will be compared to experimental results obtained in a furnace the temperature is considered constant.

It should be noted at this point that the implementation of a distributed model would allow the mitigation of these assumptions, as aspects of the model (e.g. cathode air stream CFD) could be solved on other computers.

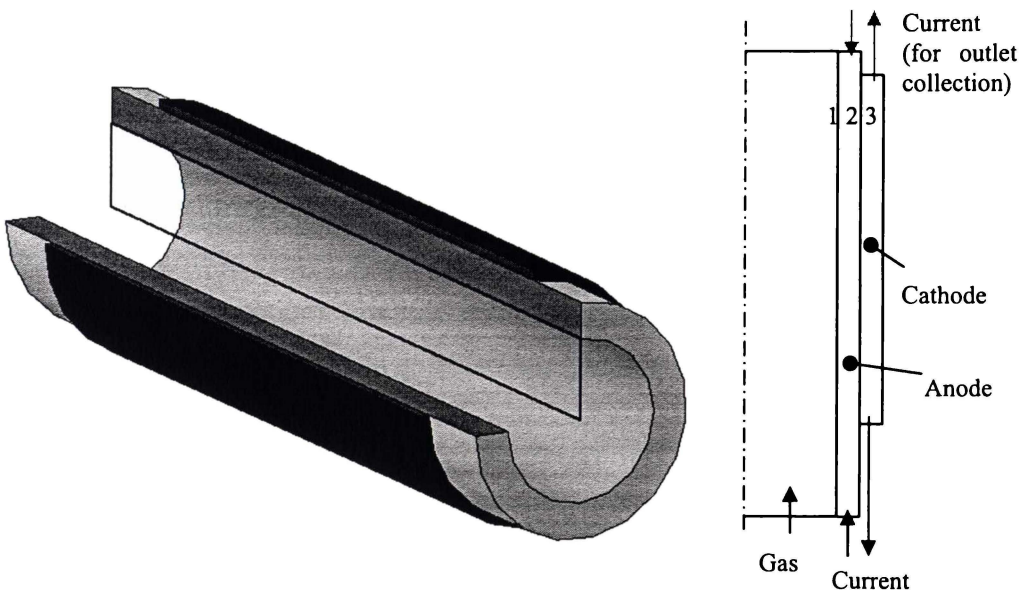


Figure 4-1 Section of tube and corresponding model geometry

4.1.2 The Method of Finite Elements

Any number of elementary texts on finite element modelling will provide a detailed breakdown of the method of finite elements, with Zienkiewicz [2] being one example. An online reference text is also provided by the University of Auckland, New Zealand†. As a brief overview, the finite element method is in essence a refined approximation. The problem domain is divided into a finite number of elements, with nodes forming the vertices of these elements. The differential equations under examination are approximated in terms of nodal values and interpolations between nodes. This approximation allows for the creation of a stiffness matrix which, upon multiplication with a vector of nodal values, equates to a vector of source terms. So the solution is reached by solving this system of equations (or finding the inverse of the stiffness matrix). It is at this point that numerical methods come into play, to solve what can be an extremely large matrix. Numerical methods provide a solution that is arbitrarily accurate at

† <http://www.esc.auckland.ac.nz/Academic/Texts/FEM-BEM-notes.html>

each point in the matrix. Many numerical methods exist for solving these equations (e.g. Gaussian elimination, Gauss-Seidel iteration, successive over-relaxation, generalized minimal residual, Chebyshev iteration), but the selection of methods is usually limited in commercial finite element software. Selection of solution method is highly dependant on the system being solved. For example, a small finite element problem will often best be solved with a direct Gaussian elimination. However, as the model size increases, the memory requirements of a direct solution increase, possibly necessitating an iterative method.

4.1.3 Flow Field – Momentum Transport

Considering only the gas stream, the flow field is obtained via the Navier-Stokes equations, that is, a momentum balance (equation 4-1) and the steady-state continuity equation (4-2). Here, μ is the viscosity of the fluid, \mathbf{u} is the velocity vector (u_r, u_z), ρ is the fluid density, and P is the pressure.

$$-\mu \nabla^2 \mathbf{u} + \rho(\mathbf{u} \cdot \nabla) \mathbf{u} + \nabla P = 0 \quad (4-1)$$

$$\nabla \cdot \mathbf{u} = 0 \quad (4-2)$$

Boundary conditions for the Navier-Stokes momentum balance, in equation (4-1), are determined for the gas sub-domain, as shown in Figure 4-1. In the expression of boundary conditions, \mathbf{n} is the unit vector normal to the boundary, and \mathbf{t} is the unit vector tangential to the boundary. At the anode boundary a no-slip condition is specified, i.e. all velocity components are zero ($\mathbf{u} = 0$). Inherent in this condition is the assumption that all mass-transfer between the gas stream and the porous anode structure occurs by diffusion. At the opposite boundary (the symmetry axis) an infinite slip condition applies, whereby there is no velocity term normal to the boundary ($\mathbf{n} \cdot \mathbf{u} = 0$). As the gas flow rate is relatively small the flow-field at the exhaust is assumed to be purely normal to the exhaust boundary and the reference pressure is deemed to apply ($\mathbf{t} \cdot \mathbf{u} = 0, P = 0$). The

inflow condition (inlet axial velocity; $\mathbf{u} = \mathbf{u}_0$) specified in equation (4-3) is calculated from the required fuel flow, ϕ , (rendered as a volumetric flow rate with the ideal gas law) divided by the cross-sectional area, where the fuel flow is determined from the estimated current, I , and specified fuel utilization, η , by Faraday's law; equation (4-4).

$$u_z = \frac{\phi R T}{\pi r^2 P} \quad (4-3)$$

$$\phi = \frac{I}{2F\eta} \quad (4-4)$$

Within each element the fluid density is calculated from the ideal gas law, using an average mass calculated from the local composition. The average mass in equation (4-5), is calculated from the sum of products of the mole fraction, χ , and mass, M , for each species, i .

$$\rho = \frac{P \sum \chi_i M_i}{R T} \quad (4-5)$$

Viscosity is initially considered to be constant, a general condition of the Navier-Stokes equations in Femlab, and is initially set to 2×10^{-5} kg.m⁻¹.s⁻¹, approximately the viscosity of hydrogen at 800°C [3].

4.1.4 Diffusion – Mass Transport

Mass transfer by diffusion occurs in both the gas and anode regions. The current model considers only hydrogen and water but, in anticipation of a methane/syngas model, a multi-component diffusion model was selected rather than simple binary diffusion (Fick's law). Femlab provides a multi-component diffusion system

based on the Maxwell-Stefan equations, utilizing Curtis' well established symmetric diffusivities definition [4]. The mass-balance is specified by equation (4-6), wherein, w is the mass fraction, and D_{eff} is the effective diffusivity of component i in component k .

$$\nabla \cdot \left[-\rho w_i \sum_{\substack{k=1 \\ k \neq i}}^n D_{eff} \frac{M_{Tot}}{M_k} \left(\nabla w_k + w_k \frac{\nabla M_{Tot}}{M_{Tot}} \right) \right] = 0 \quad (4-6)$$

For gases at low density, the Maxwell-Stefan diffusivities can be replaced by the binary diffusivities. The binary diffusivities are predicted using the Fuller-Schettler-Giddings relationship [5] (an empirical fit based on the kinetic theory of gases), as recommended by Reid et al [6]. Equation (4-7) expresses the (symmetric) diffusivity, D_{ik} , of gas i in gas k , using the specific atomic diffusion volumes, v_i and v_k .

$$D_{ik} = \frac{1.013 \times 10^{-6} T^{1.75}}{P \left(v_i^{1/3} + v_k^{1/3} \right)^2} \left(\frac{1}{M_i} + \frac{1}{M_k} \right)^{0.5} \quad (4-7)$$

Bulk diffusion in the porous anode, D_{eff} , is scaled by the ratio of porosity, ϵ_p , to tortuosity, τ .

$$D_{eff} = \frac{\epsilon_p}{\tau} D_{ik} \quad (4-8)$$

Due to a lack of better information, the tortuosity is initially set to 6. The porosity has been determined experimentally as 0.3 [7].

Following Virkar et al [8], the initial model approximates the total effective diffusivity from the effective binary diffusivity, ignoring the Knudsen diffusion contribution. This is justified by the fact that the mean free path of the molecules is orders of magnitude less than the pore diameter, while the standard condition for Knudsen diffusion is for a mean free path greater than ten times the pore diameter.

The local current density (j) is calculated in the electrochemical model (see below). In order to allow ready comparison with experimental data, the feed gas is assumed to be humidified to 3 mol% water, thus $\chi_{H_2,in}$ (inlet hydrogen mole fraction) is set at 0.97.

The boundary conditions for diffusive mass transfer are slightly more complex than those for momentum transport. At the gas inlet, the gas composition is specified by setting the hydrogen mass fraction as specified in equation (4-9).

$$w_{H_2} = \frac{\chi_{H_2,in} M_{H_2}}{\chi_{H_2,in} M_{H_2} + (1 - \chi_{H_2,in}) M_{H_2O}} \quad (4-9)$$

At the gas outlet, the dominant mass transport mechanism is convective transport, so the mass flux is specified by the boundary velocity as shown in equation (4-10).

$$\mathbf{n} \cdot \mathbf{m}_{H_2} = w_{H_2} \rho \mathbf{u} \cdot \mathbf{n} \quad (4-10)$$

Electrochemical conversion is accounted for, in the diffusion model, by an outward flux of hydrogen at the electrolyte interface, according to the corresponding outward current density, j , at the boundary and Faraday's law (equation 4-11).

$$\mathbf{n} \cdot \mathbf{m}_{H_2} = \frac{-j M_{H_2}}{2 F} \quad (4-11)$$

All other boundaries are impervious, so a zero flux condition applies ($\mathbf{n} \cdot \mathbf{m} = 0$).

4.1.5 Electronic – Electron Transport

The electrical energy balances, in the cathode and anode, are modelled separately, with a standard DC conductivity differential equation,

$$-\nabla \cdot (\sigma \nabla V) = 0 \quad (4-12)$$

where $-\sigma \nabla V = \mathbf{J}$ (the current density vector), and σ is the electronic conductivity ($S.m^{-1}$).

Conductivity, σ , is expressed as a function of temperature in both anode and cathode domains. In order to account for the scaling of the cathode current collector geometry, the conductivity is scaled to compensate for this. The bulk conductivity scales inversely with the change in cross-sectional area (A_{old}/A_{new}).

The lower boundaries of these regions impart the potential constraints, defining the cell operating voltage, as this is where the current is physically collected. The anode terminal is arbitrarily selected as the voltage reference (set to 0 V), and the cathode terminal is set to the operating voltage. The shared boundary (electrolyte interface) has a specified current density ($j = -\mathbf{n} \cdot \mathbf{J}$), as calculated in the electrochemical model, and this ensures that the two domains are consistent. All other boundaries are insulating ($-\mathbf{n} \cdot \mathbf{J} = 0$).

Initial results led to the testing of current collection at both ends of the cell and the additional potential constraints are added in the model for comparison. The additional current collection is shown in grey in Figure 4-1. The ends of the cell are forced to be equipotential, as would be required in a stack.

4.1.6 Electrochemistry

As fuel is consumed along the length of the fuel cell, the Nernst potential will drop. However, the conduction losses in the current collectors increase with length and hence the local cell potential decreases more rapidly than the Nernst potential. The Nernst potential is calculated from published values for the temperature dependence of the Gibbs potential [3] and the concentration gradient (equation 4-13). As the cathode oxidant concentration is held constant, and cathodic diffusion is ignored, the partial pressure of oxygen, p_{O_2} , is fixed at 0.21.

$$E_N = 1.271 - 2.75 \times 10^{-4} T - \frac{RT}{2F} \ln \left(\frac{p_{H_2O}}{p_{H_2} p_{O_2}^{0.5}} \right) \quad (4-13)$$

The difference in electrode potentials, $E_C - E_A$, (which is also the local cell potential) must be equal to the Nernst potential less any overpotential. This can be re-arranged such that the sum of the overpotentials equates to the Nernst potential less the electrode potential (equation 4-14).

$$E_N - (E_C - E_A) = E_{ohm} + E_{act,C} + E_{act,A} \quad (4-14)$$

The ohmic overpotential, E_{ohm} , is determined from literature values of the ionic conductivity for yttria-stabilized zirconia [3], and is shown in equation 4-15. Note that the electrode portions of the ohmic overpotential are accounted for in the electrical partial differential equations.

$$E_{ohm} = 1.1765 \times 10^{-5} t_{el} e^{\left(\frac{11000}{T}\right)} \cdot j \quad (4-15)$$

The Butler-Volmer equation is utilized in the calculation of activation overpotentials, E_{act} . In the Butler-Volmer equation (4-16), j_0 is the exchange current density, β is the ionic exchange transfer co-efficient, and n_e is the number of electrons transferred.

$$j = j_0 \left\{ \exp \left[\beta \frac{n_e F E_{act}}{R T} \right] - \exp \left[(\beta - 1) \frac{n_e F E_{act}}{R T} \right] \right\} \quad (4-16)$$

Using a transfer co-efficient of 0.5, this expression conforms to the definition of the hyperbolic sine function, and can then be rearranged to give expressions for the two electrode overpotentials (equations 4-17, 4-18).

$$E_{act,C} = \frac{R T}{2 F} \sinh^{-1} \left(\frac{j}{2 j_{0,C}} \right) \quad (4-17)$$

$$E_{act,A} = \frac{R T}{F} \sinh^{-1} \left(\frac{j}{2 j_{0,A}} \right) \quad (4-18)$$

Substituting into equation (4-14), the local cell potential becomes a complicated function of the current density. This would lend itself well to the specification of boundary potential, rather than current density, but the differential equations become unstable in this configuration, hence equation (4-14) must be solved for current density. An alternative to this is to add an outer iteration, solving the electrochemical equations as another system. However, the combination of overpotentials can be empirically approximated by a hyperbolic sine function. This fit is most applicable when the activation overpotentials are dominant, and the exchange current densities are either, close to equal, or one dominates. The fit

can also be improved by additional factors. In this system the most efficient was found to be an additional exponential term (equation 4-19).

$$j = k_1 \exp\left[\frac{k_2}{T}(E_N + E_A - E_C)\right] \sinh\left[\frac{k_3}{T}(E_N + E_A - E_C)\right] \quad (4-19)$$

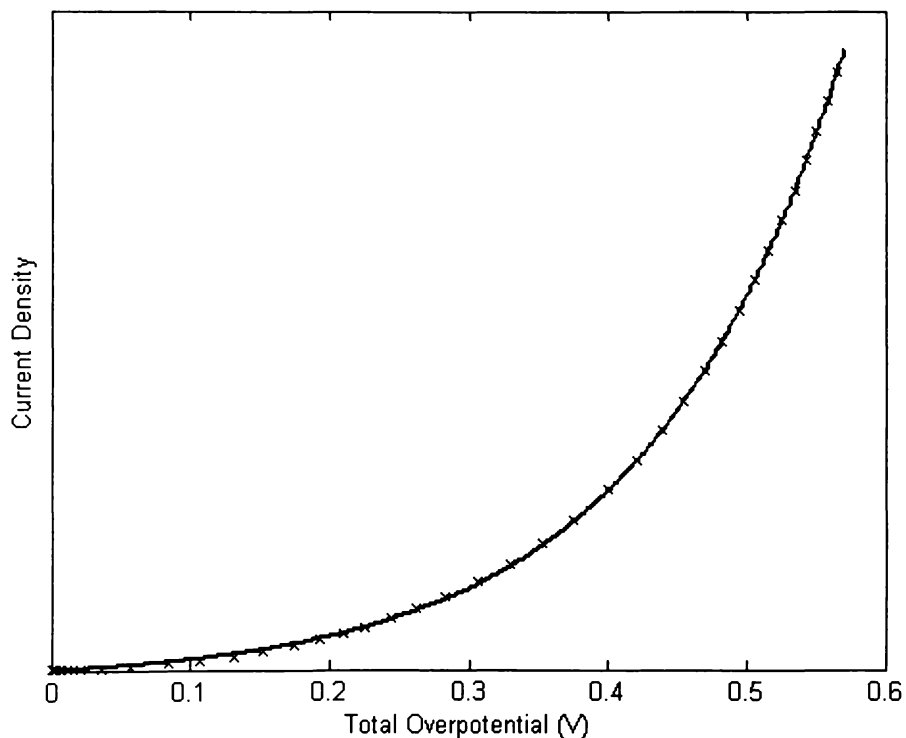


Figure 4-2 Empirical fit of current density to total overpotential

In this application, the exchange current densities are very different. Anode exchange current density is taken from literature [1] while the much lower, and therefore dominant, cathode term was determined experimentally [9] as described in 4.1.6.1 *Cathodic Exchange Current Density*. A limitation of this approach is that the fit must be re-calculated if any of the overpotential terms need to be modified. The utility of this fit can be seen in Figure 4-2, where the points represent calculated data and the line is the fit specified by equation 4-19. The fit

coefficients were recalculated at a number of temperatures, between 650°C and 1000°C, and k_1 , k_2 and k_3 were found to be constant across this temperature range. The local current density is calculated at each element along the boundary, and is used in boundary conditions for the electrical and diffusion models.

4.1.6.1 Cathodic Exchange Current Density

Effective exchange current density has been determined by fitting the fuel cell voltage-current characteristic at low current density to equation 4-20, wherein the ohmic overpotential is determined experimentally using the current interruption technique, and E_N , and j_0 are the fitting parameters.

$$E = E_N - E_{\text{ohm}} - \frac{RT}{2F} \ln \left(\frac{1}{2j_0} + \frac{1}{2} \sqrt{\left(\frac{j}{j_0} \right)^2 + 4} \right) \quad (4-20)$$

By fixing the anode exchange current density high (as described above), the cathode exchange current density is calculated to be 200 A.m^{-2} . This value is an order of magnitude lower than the commonly reported literature value of 2000 A.m^{-2} but a number of factors should be considered.

This method of fitting, lumps all unknown effects into this single value. For example, if the anode exchange current density was lower than the assumption, the cathode exchange current density would actually be a higher value. A further complicating factor is the geometry of the sample. It has been established that tubular electrochemical cells present voltage fields that disrupt the normal function of reference electrodes [10]. This calls into question the validity of current interruption measurements to accurately isolate ohmic and activation effects. For this reason, higher values of the cathode exchange current density will be explored later.

4.1.7 Thermal

The primary directive of this initial modelling is validation against steady-state laboratory test data. As these results are obtained in a temperature controlled electric furnace, the model temperature is considered constant.

4.1.8 Mesh and Solver

Femlab creates a tetrahedral/triangular Delaunay mesh using a successive refinement algorithm. The mesh utilized consists of approximately 5 000 nodes, 8 000 elements, and gives rise to 40 000 degrees of freedom. The system does not readily solve with an iterative solver, so a full non-linear solution is required. This leads to a large matrix and correspondingly large computational memory requirement. In order to reduce the matrix size, and therefore the memory requirement, the problem is solved as two coupled systems. First the CFD and diffusion equations are solved as a fully coupled system. Once convergence of this system is obtained, the subsequent solution encompasses the diffusion and electrical potentials. In this way, the diffusion equations act as a coupling system, yielding improved stability (over a fully separated solution) and improved convergence rate (over a fully coupled system).

The output current of the system is calculated (by boundary integration) and the input current estimate is then updated for the next iteration. Iterations proceed until the output current agrees with the value calculated by Faraday's Law (from the input fuel and target fuel utilization) to within a specified error level. On systems with sufficient memory (1 gigabyte or more) the complete system can be solved as a single matrix, although stability was improved if the first iteration was solved as two systems, as described above.

4.2 Model Validation

Limited experimental data is available for tubular SOFCs. Validation of the model is made against previously unpublished experimental data, before the model is used to predict the effects of design variations. Geometry of the three tube types analyzed is given in Table 4-1.

Table 4-1 Tube geometries

Tube identifier	Outside diameter (mm)	Anode thickness (mm)	Active length (mm)
A	7.5	0.75	190
B	14.3	1.42	190
D	14.3	1.42	330

The correlation between modelled and experimental data can be seen in Figure 4-3 through Figure 4-6, wherein the apparent scattering of the experimental data is due to the collation of multiple samples (i.e. several almost linear plots). While both models A and B align with the best experimental performance at 800°C (Figure 4-3 and Figure 4-5), the 850°C model lies in the middle of the experimental data (Figure 4-4). This suggests that the geometry effects are reasonably well modelled, but the temperature dependencies may require some adjustment.

Figure 4-3 shows that the predicted voltage drop due to an increase in fuel utilization (from 50% to 75%) is much less than the experimental value. A number of plausible explanations present themselves, including, poor modelling of diffusion characteristics, and limited experimental data.

Figure 4-5, shows a wide variation in experimental data which has been attributed to a change in processing methods, however details of this change could not be furnished to the author. The higher points correspond to an earlier batch, produced by a similar method to that for geometry A. Geometry D shares the characteristic of the lower performers from geometry B, which could explain the over-estimation of performance shown in Figure 4-6. However, the *magnitude* of change for current collection at both ends can be seen to correlate reasonably well.

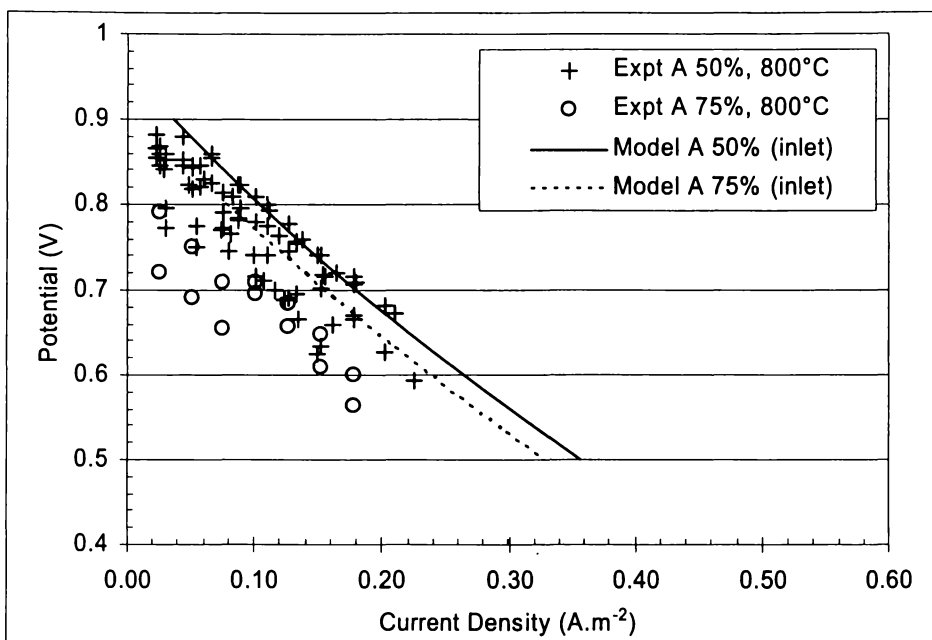


Figure 4-3 Experimental and modelled data at 800°C (geometry A)

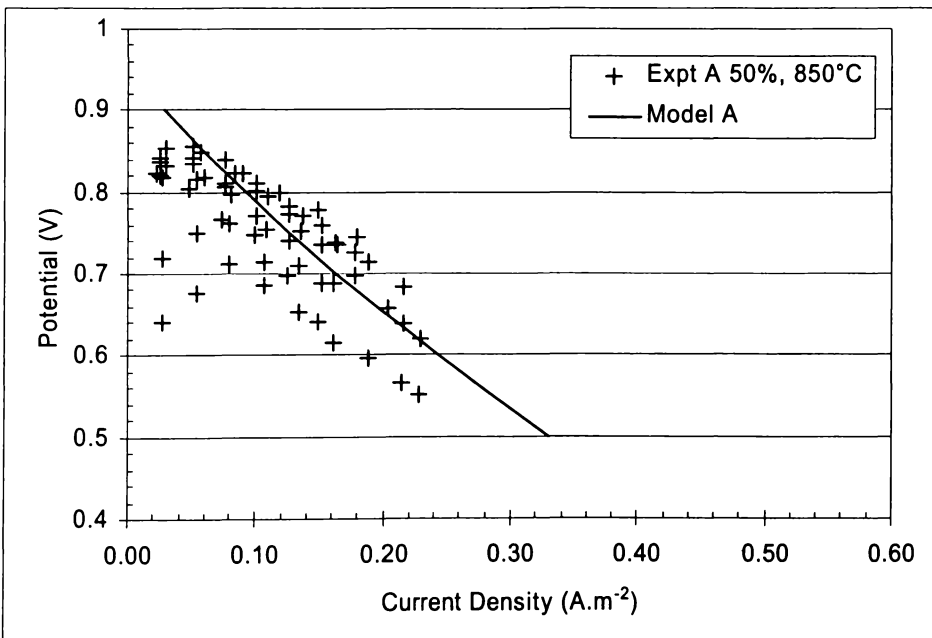


Figure 4-4 Experimental and modelled data at 850°C (geometry A)

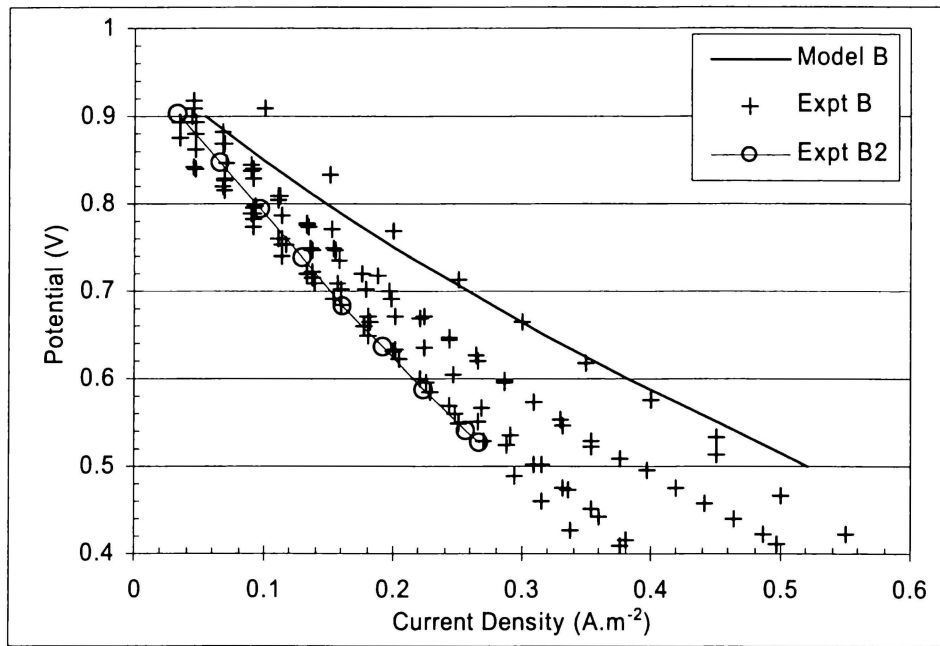


Figure 4-5 Experimental and modelled data at 800°C (geometry B)

4.2.1 Single/Double-ended geometry

Upon obtaining model data for the existing designs, one of the proposed changes was the addition of a current collection point at the exhaust end of the cell. The modelled impact of this on the current density profile (at constant terminal voltage) can be seen in Figure 4-7, and the increase in total current output (integral of the current density) is approximately 75% (Figure 4-6). This agrees well with the little experimental data yet available, which exhibits an increase of 60 - 70%, even though the absolute fit is poor.

Figure 4-8 shows that a sharp impact on the hydrogen mole fraction is concomitant with outlet current collection. At higher levels of fuel utilization, this effect could contribute to performance degradation, due to this diffusion limitation at the outlet.

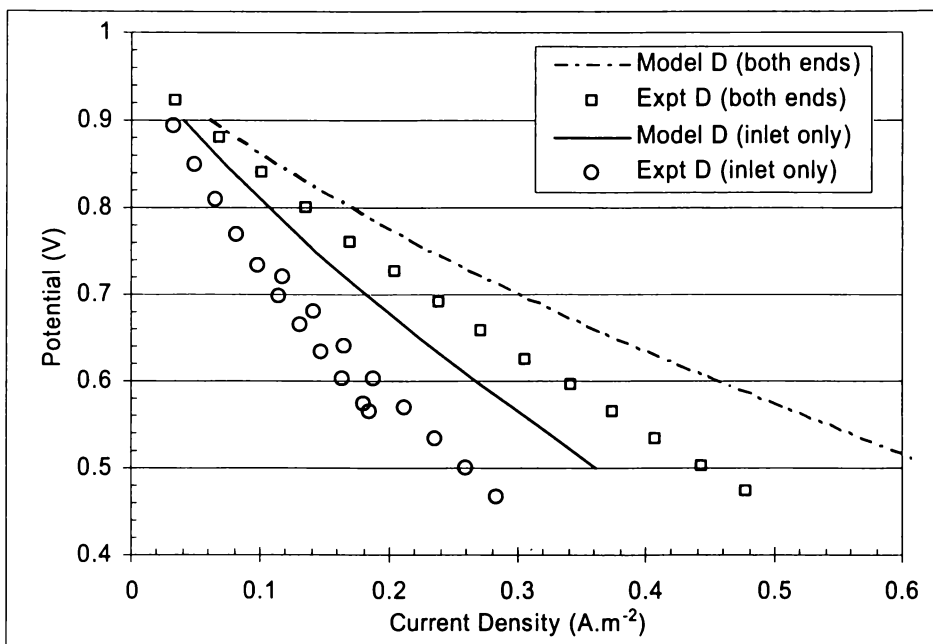


Figure 4-6 Experimental and modelled data at 800°C and (geometry D)

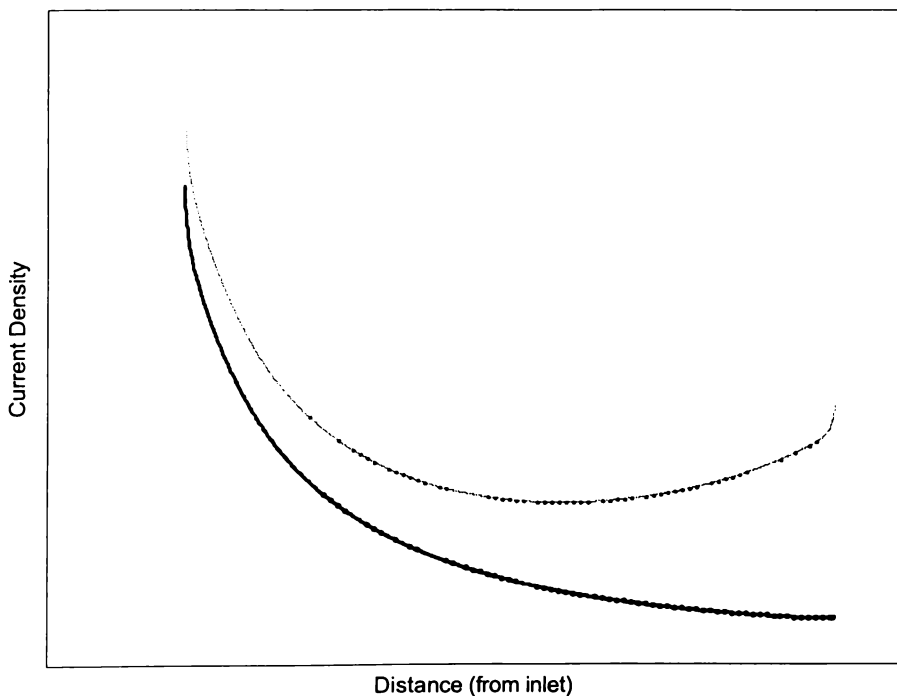


Figure 4-7 Axial current density plot showing single end and double end collection

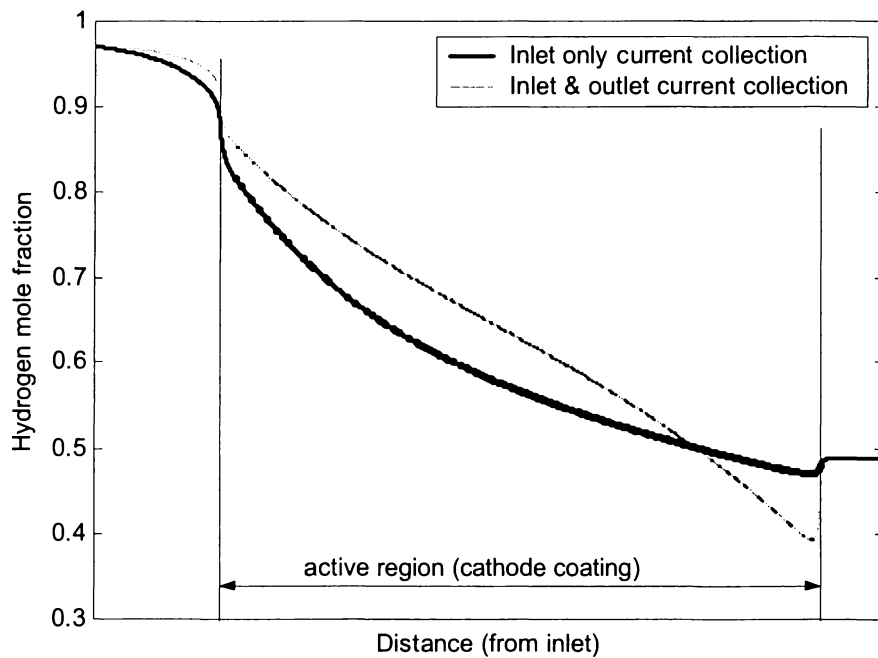


Figure 4-8 Axial hydrogen mole fraction at electrolyte boundary (50% fuel utilization)

4.3 Conclusions

Modelling of a tubular solid oxide fuel cell, under laboratory conditions, has been undertaken. The model has been validated against experimental data providing reasonable prediction of geometric variations, with a possible weakness uncovered in thermal dependencies.

4.4 List of Symbols

D^T thermal diffusivity ($\text{m}^2.\text{s}^{-1}$)

E voltage, potential, overpotential (V)

E_A anodic potential (V)

E_C cathodic potential (V)

E_N Nernst potential (V)

F	Faraday's constant (96485 C.mol ⁻¹)
I	current (A)
j	current density (A.m ⁻²)
j ₀	exchange current density (A.m ⁻²)
M _i	molar mass of specie i (kg)
p	partial pressure (Pa)
P	pressure (Pa)
R	ideal gas constant (8.3145 J.K ⁻¹ .mol ⁻¹)
T	Temperature (K)
t _{el}	thickness of electrolyte layer (m)
u	velocity component (m.s ⁻¹)
w	mass fraction ()

vectors

j _i	diffusive mass flux vector of component i
m	mass flux vector
n	normal vector (to a boundary)
t	tangent vector (to a boundary)
u	velocity vector

greeks

ρ	density (kg.m ⁻³)
μ	dynamic viscosity (kg.m ⁻¹ .s ⁻¹)
ϕ	flow (mol.s ⁻¹)
η	fuel utilization

τ tortuosity

χ_i mole fraction of species i

ϵ_p porosity

4.5 Default Values

		H ₂	H ₂ O	
D ^T	thermal diffusivity (m ² .s ⁻¹)	1.310 x10 ⁻³	2.015 x10 ⁻⁴	
M _i	molar mass of specie i (kg)	2.017 x10 ⁻³	18.03 x10 ⁻³	
v	gas diffusion volume	7.07 x10 ⁻⁶	12.7 x10 ⁻⁶	
		Ni	Ag	
σ	electronic conductivity (S.m ⁻¹) (scaled for porosity/surface area)	3.29 x10 ⁵	4.10 x10 ⁶	
		j _{0A} (A.m ⁻²)	j _{0C} (A.m ⁻²)	
j ₀	exchange current density	5000	200	
		k ₁ (A.m ⁻²)	k ₂ (K.V ⁻¹)	k ₃ (K.V ⁻¹)
	Overpotential fitting coefficient	4968	4839	2348
$\chi_{H_2,0}$	inlet mole fraction hydrogen	0.97		
μ	dynamic viscosity (kg.m ⁻¹ .s ⁻¹)	2 x 10 ⁻⁵		
T	Temperature (K)	750, 800, 850 °C		
t _{el}	thickness of electrolyte layer (m)	20 μm		

η	fuel utilization	0.50, 0.75
τ	tortuosity	6
ϵ_p	porosity	0.3

4.6 References

1. Chan, S. H., Khor, K. A. & Xia, Z. T. A complete polarization model of a solid oxide fuel cell and its sensitivity to the change of cell component thickness. *Journal of Power Sources* **93**, 130-140 (2001).
2. Zienkiewicz, O. C. *The Finite Element Method in Engineering Science* (McGraw-Hill, London, 1993).
3. Bossel, U. G. in *Final Report on SOFC Data* (International Energy Agency, Berne, 1992).
4. Curtiss, C. F. Symmetric gaseous diffusion coefficients. *Journal of Chemical Physics* **49**, 2917-2919 (1968).
5. Fuller, E. N., Schettler, P. D. & Giddings, J. C. New Method For Prediction Of Binary Gas-Phase Diffusion Coefficients. *Industrial Engineering Chemistry* **58**, 18-27 (1966).
6. Reid, R. C., Sherwood, T. K. & Prausnitz, J. M. *The Properties of Gases and Liquids* (McGraw-Hill, 1987).
7. Fernandes, N. Unpublished results, Acumentrics Corporation (2003).
8. Virkar, A. V., Chen, J., Tanner, C. W. & Kim, J.-W. The role of electrode microstructure on activation and concentration polarizations in solid oxide fuel cells*1. *Solid State Ionics* **131**, 189-198 (2000).
9. Gopalan, S. Unpublished experimental data, Boston University (2003).
10. Adler, S. B., Henderson, B. T., Wilson, M. A., Taylor, D. M. & Richards, R. E. Reference electrode placement and seals in electrochemical oxygen generators. *Solid State Ionics* **134**, 35-42 (2000).

5 Component Analysis Results for a Tubular SOFC

In order to provide direction for further research into specific cell components, a parametric analysis of the tubular solid oxide fuel cell (SOFC) is undertaken. Results contained herein are derived from the partially validated model described previously. Primary losses are shown to occur due to the cathode activation polarization and the anode conductivity. Modelling of variations in these two components provides vectors for further development.

5.1 Component Loss Calculations

Component losses, in this study, are derived by integrating, along the active layer boundary, the product of the local current density and an expression for the voltage drop, due to that component. This yields a loss in Watts, as shown in equation 5-1, wherein L is the boundary path, $j_n(L)$ is the current density normal to the boundary, $E(L,j)$ is the voltage drop attributed to the component., and \dot{q} is the loss in Watts (using common notation for heat energy).

$$-\dot{q} = 2\pi r \int_a^b [j_n(L) \cdot E(L,j)] dL \quad (5-1)$$

In this model the boundary path is linear, in the z-direction, so the path, L, in equation 5-1, becomes z.

For the anode and cathode conduction losses, the $E(L,j)$ term is obtained directly from the model's DC conductivity solution (offset for the outlet terminal voltage).

The loss due to the ohmic drop is the only mechanism considered in the electrolyte, and in this case E is determined as shown in equation 5-2, wherein t_{el} is the electrolyte thickness. It should be noted that the constant in the exponential

incorporates the Ideal gas constant, from the Arrhenius equation. Substitution into equation 5-1, and changing path dimension, yields equation 5-3. Note that the temperature dependence of the electrolyte resistivity could be removed from the integral, as this particular model is isothermal.

$$E_{\text{ohm}} = 1.1765 \times 10^{-5} t_{\text{el}} e^{\left(\frac{11000}{T}\right)} \cdot j \quad (5-2)$$

$$-\dot{q}_{\text{electrolyte}} = 2.353 \times 10^{-5} \pi r t_{\text{el}} \int_{z_0}^{z_1} [j_n^2 \cdot e^{\left(\frac{11000}{T}\right)}] dz \quad (5-3)$$

The Butler-Volmer equation is utilized in the calculation of activation overpotentials, E_{act} , as described previously. Using a transfer co-efficient of 0.5, the two electrode overpotentials, are repeated in equations 5-4 and 5-6, with the corresponding loss integrals in equations 5-5 and 5-7.

$$E_{\text{act,C}} = \frac{RT}{2F} \sinh^{-1} \left(\frac{j}{2j_{0,C}} \right) \quad (5-4)$$

$$-\dot{q}_{\text{act,C}} = \pi r \frac{RT}{F} \int_{z_0}^{z_1} [j_n \sinh^{-1} \left(\frac{j}{2j_{0,C}} \right)] dz \quad (5-5)$$

$$E_{\text{act,A}} = \frac{RT}{F} \sinh^{-1} \left(\frac{j}{2j_{0,A}} \right) \quad (5-6)$$

$$-\dot{q}_{act,A} = 2\pi r \frac{R T}{F} \int_{z_0}^{z_1} j_n \sinh^{-1} \left(\frac{j}{2j_{0,A}} \right) dz \quad (5-7)$$

Increases in the cathode exchange current density are considered, requiring new relationships for the current density expression, at each value of the exchange current density. The current density expression is modified from that presented earlier to the form in equation 5-8, wherein ΣE is the sum of the overpotentials, which is equivalent to the difference between the Nernst potential and the electrode potentials. The translation of the earlier form to this one is realized by the definition of the hyperbolic sine function, and distributing the pre-exponential factor through the sinh definition. Best-fit coefficients were determined using the Matlab curve-fitting tool and are shown in Table 5-1 along with the regression statistic for each fit. The fits were evaluated at current densities from 0.001 A.m^{-2} to $25\,000 \text{ A.m}^{-2}$, with 4 points per decade up to $1\,000 \text{ A.m}^{-2}$, 500 A.m^{-2} increments up to $10\,000 \text{ A.m}^{-2}$, $2\,000 \text{ A.m}^{-2}$ increments up to $20\,000 \text{ A.m}^{-2}$, and a final point at $25\,000 \text{ A.m}^{-2}$.

$$j = A \left(e^r \sum E - e^s \sum E \right) \quad (5-8)$$

Table 5-1 Coefficients for equation 5-8 at various cathode exchange current densities.

j_{0C}	A	r	s	R^2
200	100 100	2.357	2.218	0.997
400	131 500	2.069	1.931	0.999
800	122 600	1.765	1.570	0.999 6
2 000	227 900	1.272	1.122	0.999 98
5 000	12 800	2.376	-1.296	0.999 99

Electrical conductivity of the anode is seen to be a problem, and two variations are considered to increase anode performance. First, a highly porous, cylindrical nickel insert is added inside the cell. This is modelled by extending the solution of the anode conductivity solution into the gas stream, with a conductivity determined by the nickel insert. The insert selected is a 95% porous metallic foam, with the solid component being 99.9% nickel. The conductivity of the foam is the product of the conductivity of nickel, the solid fraction (1 - porosity), and a percolation factor (c.f. 1 / tortuosity). The percolation factor is determined from room temperature conductivity measurements to be 0.35. The high porosity is required both to minimize the pressure drop inside the cell, and to lower thermal expansion mismatch stresses on the cell.

The second improvement considered for the anode conductivity is thickening of the anode. This is realized by increasing the thickness of the anode towards the axis of the cell thereby preserving the surface area of the cell, and giving comparable results. Increasing the anode thickness prompts the inclusion of a loss component attributed to diffusion limitations. From an energy balance perspective, the only remaining contributor is the so called Nernst effect, yielding equation 5-9.

$$-\dot{q}_{\text{Nernst}} = 2\pi r \frac{R T}{2 F} \int_{z_0}^{z_1} j_n \log \left(\frac{p_{H_2O}}{p_{H_2} \cdot p_{O_2}^{0.5}} \right) dz \quad (5-9)$$

The energy balance mentioned above is justified from the Nernst equation, a derivation of which is shown in equation 5-10. Certain thermodynamic definitions are utilized in equation 5-10 as follows. The starting point of the derivation is the Gibbs state function $G = H - T\Delta S$, and the definition of enthalpy (H) in terms of total energy (U) and pressure-volume work ($w = pV$). On rendering to differential form the system is restricted to an isothermal one ($dT = 0$). Once in differential form, the definitions of entropy, and energy change are used to eliminate the heat term (q). Work is subsequently considered as the work done by a change in

volume against a constant pressure, simplifying to $dG = VdP$. The ideal gas law provides the final substitution prior to integration. Following integration (from unity pressure to partial pressure), the Gibbs free energy of a substance is given as a function of its; standard Gibbs free energy, temperature, and partial pressure. Next the Gibbs free energy *change* is simplified with algebraic manipulation of the logarithms, and the reaction quotient (Q) is introduced. Finally, substitution with the electromotive force yields the familiar form of the Nernst equation, which will be used in the progression of the energy balance.

$$\begin{aligned}
 G &= H - TS \\
 &= U + pV - TS \\
 dG &= dU + pdV + VdP - TdS, & (dT = 0) \\
 &= q + w + pdV + VdP - q, & \left(dS = \frac{q}{T} \right) \\
 &= -pdV + pdV + Vdp, & (-w = pdV) \\
 &= nRT \frac{dp}{p}, & (pV = nRT) \\
 \int_{G_0}^G dG &= nRT \int_1^p \frac{dp}{p} \\
 G - G_0 &= nRT [\ln(p) - \ln(1)] \\
 G &= G_0 + RT \ln(p^n) \\
 \Delta G &= \Delta G_0 + \sum_{i=1}^{\# \text{products}} RT \ln(p_i^{n_i}) - \sum_{j=1}^{\# \text{reactants}} RT \ln(p_j^{n_j}) \\
 &= \Delta G_0 + RT \ln \left(\frac{\prod_{i=1}^{\# \text{products}} p_i^{n_i}}{\prod_{j=1}^{\# \text{reactants}} p_j^{n_j}} \right) \tag{5-10} \\
 \Delta E &= \Delta E_0 - \frac{RT}{n_e F} \ln(Q), & (-\Delta G = n_e F \Delta E)
 \end{aligned}$$

The starting point of the energy balance requires the fuel flow into the system. Ignoring the effects of fuel utilization, equation 5-11 provides a slightly modified

form of Faraday's law, expressing the electric current in terms of the integral of the current density across the electrolyte.

$$\phi = \frac{1}{n_e F} \int_{z_0}^{z_1} j_n dz \quad (5-11)$$

Given this molar flow, and ignoring any pressure volume work (ideal gas at atmospheric pressure), the rate at which energy is added to the system is given by equation 5-12. Utilizing the Gibbs free energy change definition and the electromotive force expression, equation 5-13 elucidates the loss due to the entropy change in the system. For a constant current, and temperature, this term will always be constant, and this was found to be the case in modelling.

$$\begin{aligned} -\frac{dU}{dt} &= -\phi \Delta H_0 \\ &= \frac{-1}{n_e F} \int_{z_0}^{z_1} j_n \Delta H_0 dz \end{aligned} \quad (5-12)$$

$$\begin{aligned} -\frac{dU}{dt} &= \frac{-1}{n_e F} \int_{z_0}^{z_1} j_n \Delta G_0 dz - \frac{T \Delta S}{n_e F} \int_{z_0}^{z_1} j_n dz \\ &= \int_{z_0}^{z_1} j_n \Delta E_0 dz - \frac{T \Delta S}{n_e F} \int_{z_0}^{z_1} j_n dz \end{aligned} \quad (5-13)$$

Equation 5-14 uses the Nernst equation, derived in equation 5-10, to extract the loss integral shown in equation 5-9, with an 'N' subscript added to the Nernst potential for clarity.

$$\Delta E_N = \Delta E_0 - \frac{RT}{n_e F} \ln(Q) \quad (5-14)$$

$$\int_{z_0}^{z_1} j_n \Delta E_0 dz = \int_{z_0}^{z_1} j_n \Delta E_N dz + \frac{RT}{n_e F} \int_{z_0}^{z_1} j_n \ln(Q) dz$$

Subsequently, equation 5-15, expresses the balance of the losses between the Nernst potential and the cell outlet potential. ζ represents the activation and ohmic overpotentials, the integrals for which were outlined in equations 5-3, 5-5, and 5-7, in terms of the normal current density (j_n) and temperature (T). The integral corresponding to the cell potential is obviously the cell output power, and could be used to calculate the electrical efficiency of the system. Intervening expressions represent the conduction losses in the cathode and anode respectively.

$$\Delta E_N(z) = \Delta E_{cell} + [E_{cat}(z) - \Delta E_{cell}] - E_{an}(z) + \sum_{\zeta} E_{\zeta}(j_n, T) \quad (5-15)$$

5.2 Results & Discussion

Results were obtained at 50% and 75% fuel utilization for cells of 280 mm length and 190 mm length, with equipotential current collection at both ends of the cell. In addition a 190 mm cell was modelled with current collection only at the fuel inlet. All other model parameters were kept constant, and the specified surface integrals were calculated to determine the loss of each cell component as well as the total power output. These results were then scaled by the surface area of the cell to give losses per square centimetre, facilitating comparison between models.

For each set of model parameters, the cell current was obtained for fixed cell voltages, from 0.5 V to 0.9 V in 0.05 V increments.

Results are shown in Figure 5-1 through Figure 5-6.

All results show a dominance of the cathode polarization loss at low current density, with the dc conduction loss in the anode increasing to become

comparable to, or surpass, the cathode polarization loss at higher current densities. Indicative relative contributions are shown in Figure 5-7 using the same results as Figure 5-5. Figure 5-7 highlights the shift in dominance from cathode activation at low current density to anode conduction at higher current densities.

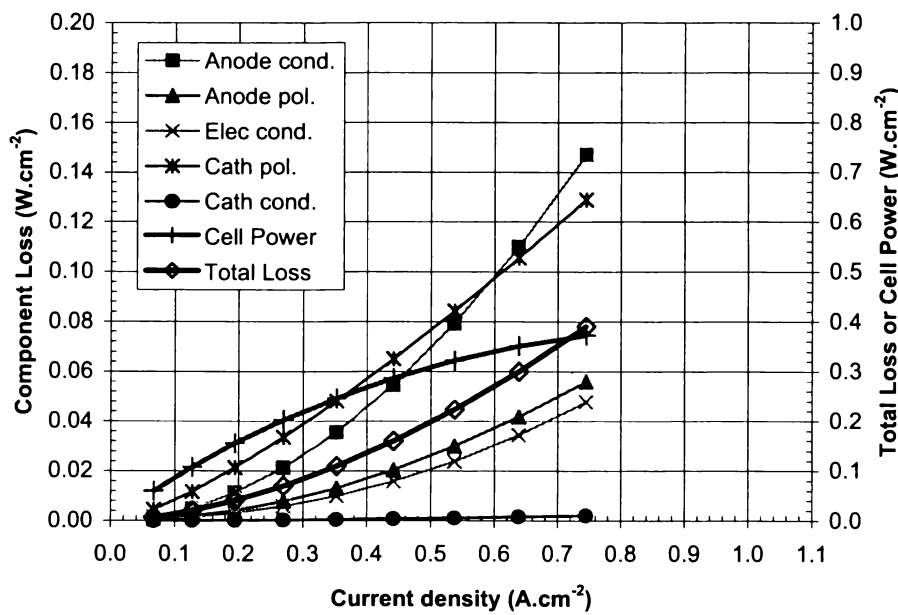


Figure 5-1 Component losses for double-ended 14 x 280 mm tube at 50% fuel utilization

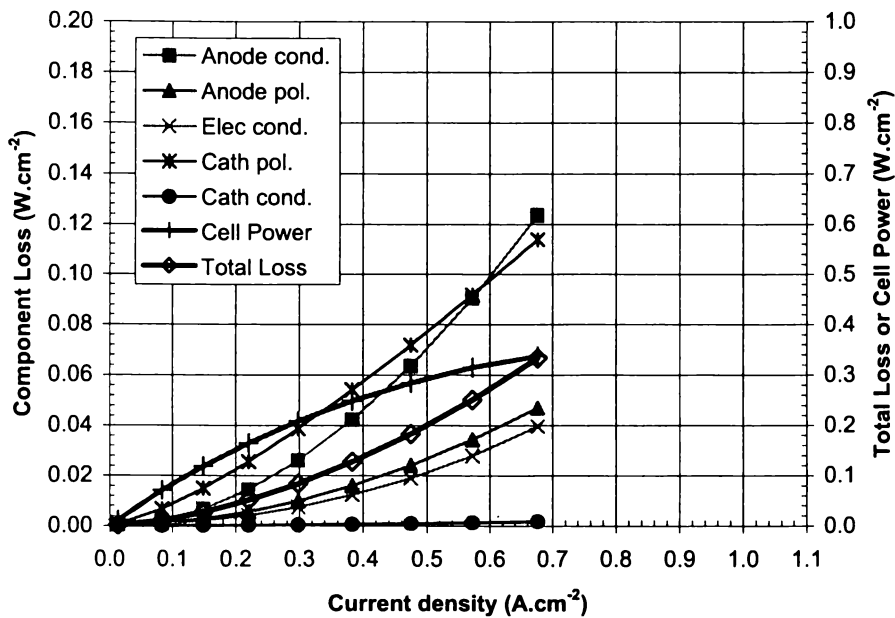


Figure 5-2 Component losses for double-ended 14 x 280 mm tube at 75% fuel utilization

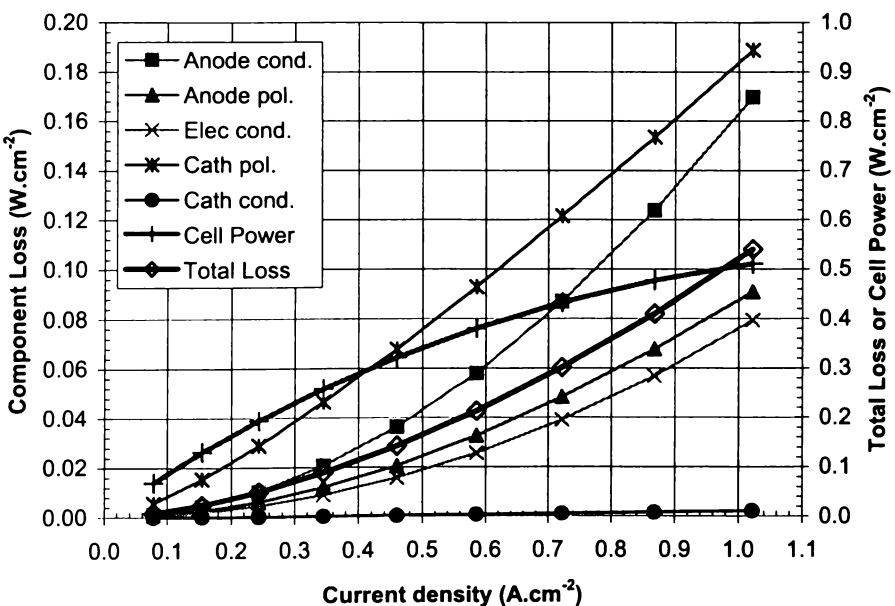


Figure 5-3 Component losses for double-ended 14 x 190 mm tube at 50% fuel utilization

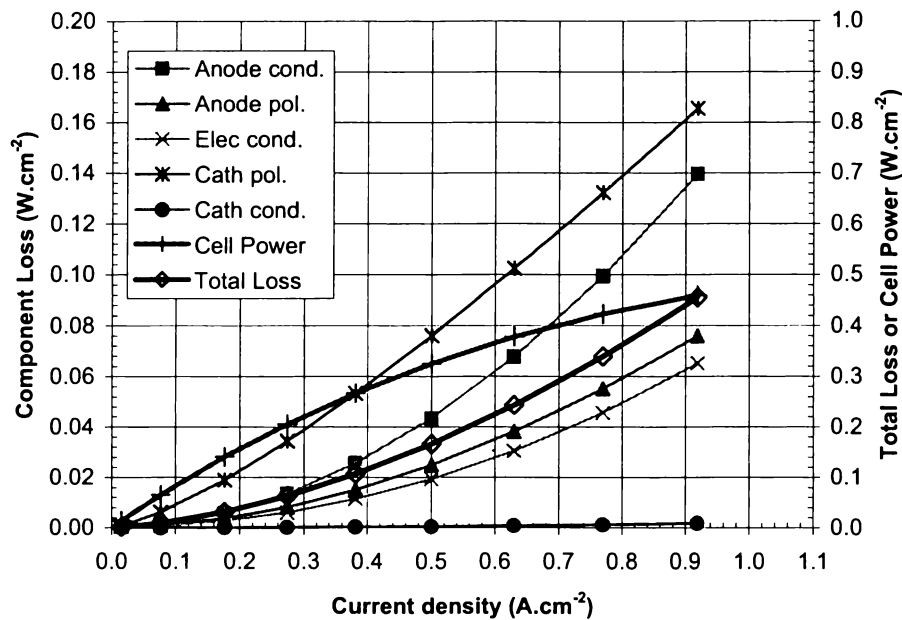


Figure 5-4 Component losses for double-ended 14 x 190 mm tube at 75% fuel utilization

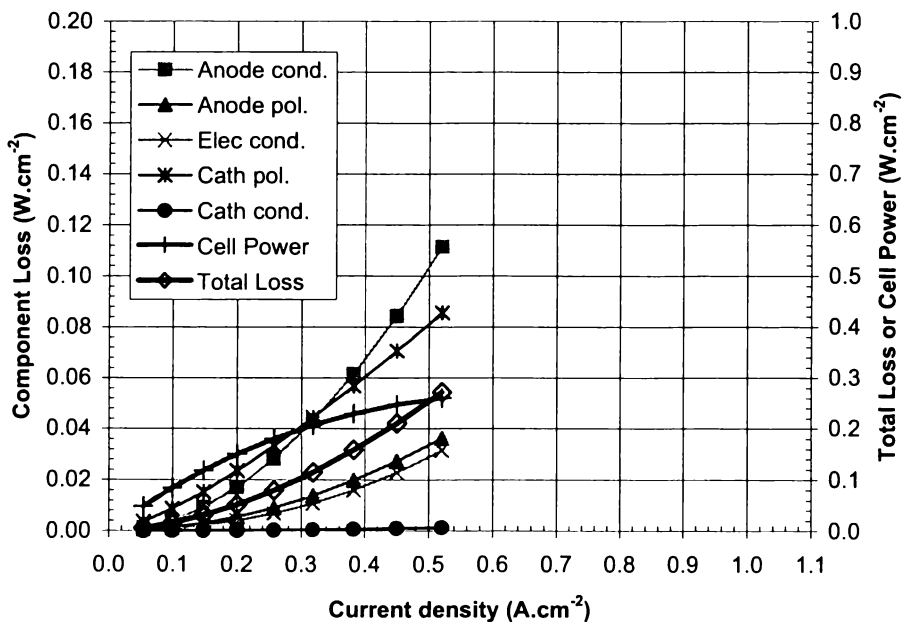


Figure 5-5 Component losses for single-ended 14 x 190 mm tube at 50% fuel utilization

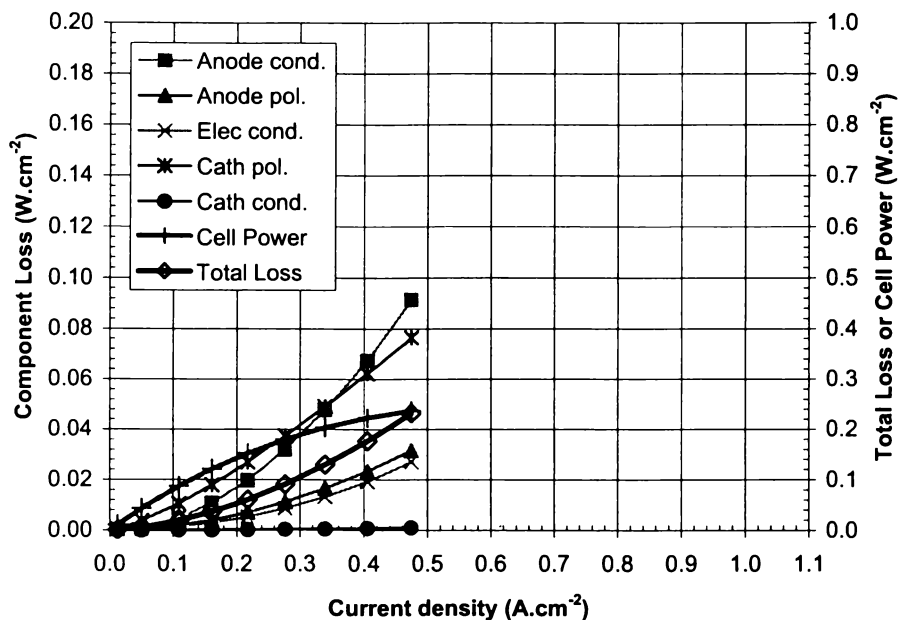


Figure 5-6 Component losses for double-ended 14 x 190 mm tube at 75% fuel utilization

The relatively low exchange current density of the cathode electrode is responsible for the significance of the cathode polarization loss. While polarization losses are expected to increase rapidly at low current densities, they are expected to be less significant at higher current densities. Polarization overpotential scales in a logarithmic fashion to current density, while resistive voltages scale linearly, according to Ohm's law. The logarithmic nature of the polarization overpotential is readily understood from the Butler-Volmer equation.

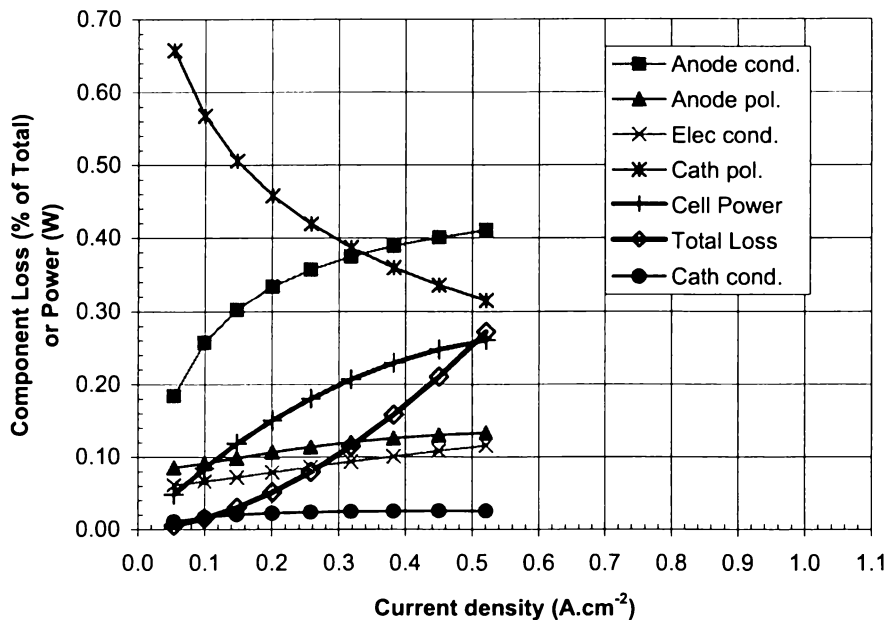


Figure 5-7 Relative losses for single-ended 14 x 190 mm tube at 50% fuel utilization

5.2.1 Cathode Polarization

Due to the low exchange current density of this cathode, the cathode polarization loss remains significant even at higher current densities. To qualify the effect of the exchange current density, further modelling was undertaken, varying the cathode exchange current density, attaining a new total polarization fit (for calculating local current density during the solution process), and solving for a fixed current density. Figure 5-8 shows the increase in cell performance at 50% utilization, with the result at 2000 A.m^{-2} accentuated as this represents a literature value for the material [1]. These results were modelled for a 280 mm long cell with current collection at the inlet only (design was changed between models).

Improvement of the cathode performance to “standard” levels is shown to yield an improvement in overall cell output of 13% (580 mV to 658 mV). However, this is an order of magnitude increase in cathode exchange current density, implying that a 5-10% improvement might be more attainable in the short term.

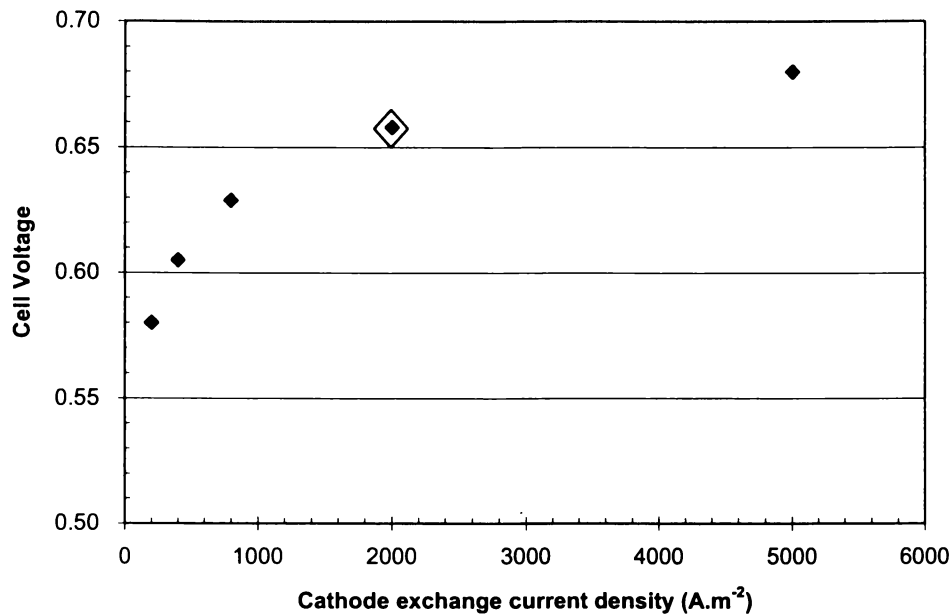


Figure 5-8 Cell performance increase due to cathode exchange current density

A breakdown of the relative component contributions is shown in Figure 5-9, further highlighting the limitation of the anode conductivity. Other trends are visible in Figure 5-9 and, while small enough to be attributed to numerical errors, could also be explained by a skewed current density distribution. For example, losses due to the anode and cathode conductivity both decrease as the cathode exchange current density is increased. Higher cathode exchange current allows for a higher current density at the start of the active area of the cell. Hence, the current density profile becomes skewed towards the cell inlet, insofar as diffusion rates allow. Correspondingly, the current has a shorter path to the cell terminals, thereby lowering the conduction losses in both electrodes. However, if the current collection were to occur only at the cell outlet (which has been explored for mechanical design reasons beyond the scope of this thesis) this behaviour would be reversed.

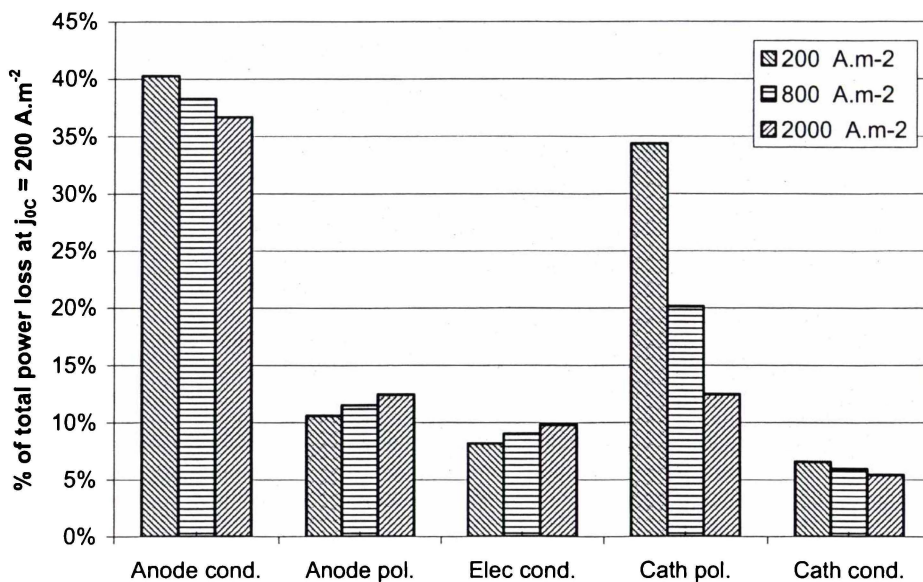


Figure 5-9 Change in component losses at various cathode exchange current densities (relative to $j_{oc} = 200 \text{ A.m}^{-2}$) for 28 cm cell at 50% fuel utilization with inlet only current collection.

5.2.2 Anode Conductivity

The strong contribution of the anode conduction loss is inherent in this tubular design. As the current must pass through the ends of the cell, current produced away from these sites (towards the middle of the tube), is subjected to a greater resistive drop. While this design relies on the anode electrode material to carry current from the cell, this can be seen to be a severe limitation at present (in agreement with Boersma et al. [2]). Increasing the thickness of the anode material, while improving the current carrying capacity, will lead to longer diffusion times, and could impact the manufacturability of the tube. Specific manufacturing issues would include the ability to dry a thicker extrudate without cracking, and sinterability of the dried extrudate.

Addition of a metallic insert, as described above, into the gas stream yields a modelled improvement in overall performance of 5% (+28 mV), by reducing the anode conductivity loss by 15% (see Figure 5-10). While the improvement in anode conductivity is to be expected, the effect of the metallic insert is most easily

quantified by examining the change in the current density distribution (with reference to the skewed current density distribution shown in Figure 4-7). Figure 5-11 shows the impact of the insert on both the cross-plane current density (impacts the activation overpotentials), and the in-plane, or cumulative, current density. By increasing the in-plane conductivity, the insert promotes a more uniform cross-plane current density distribution, reducing the cross-plane current density range from (471, 5950) to (513, 5560). The effect of the insert on the gas flow was not considered, as the porosity of 95% is deemed insignificant.

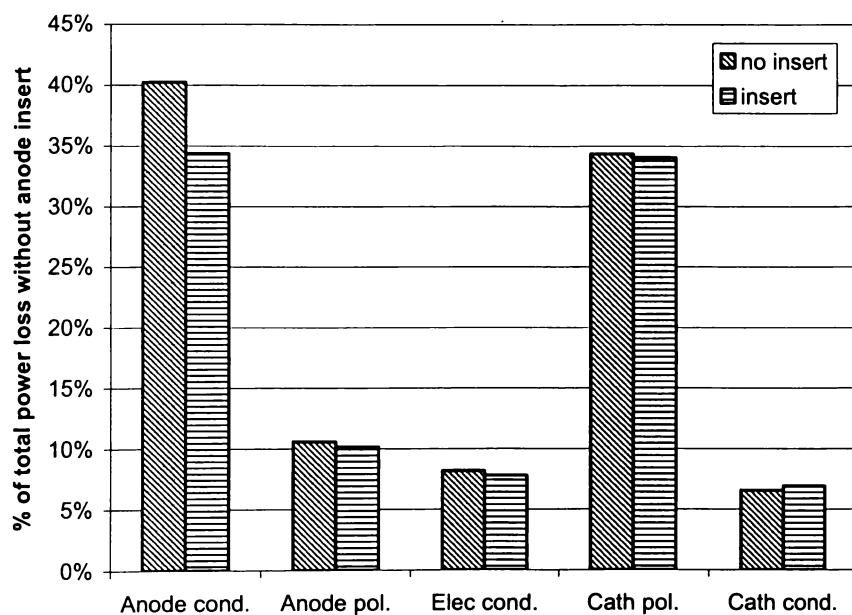


Figure 5-10 Change in component losses due to the addition of a porous metallic annulus.

Fernandes [3] performed an experimental comparison of two fuel cells with the anode insert, against two control cells for 1000 hours. The reported increase in cell voltage due to the nickel insert of ~30 mV is in good agreement with the predicted improvement (28 mV).

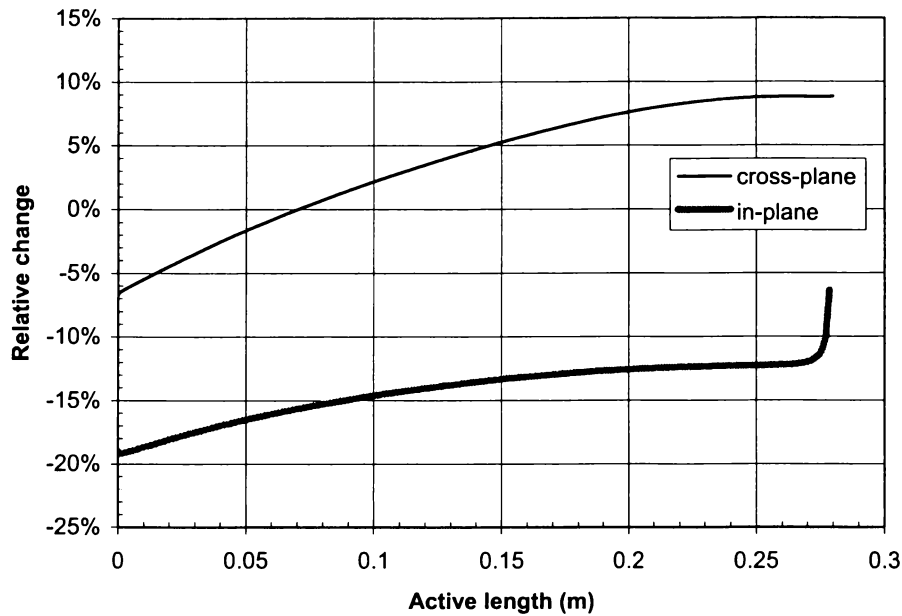


Figure 5-11 Percentage change in current density distribution due to introduction of anode insert.

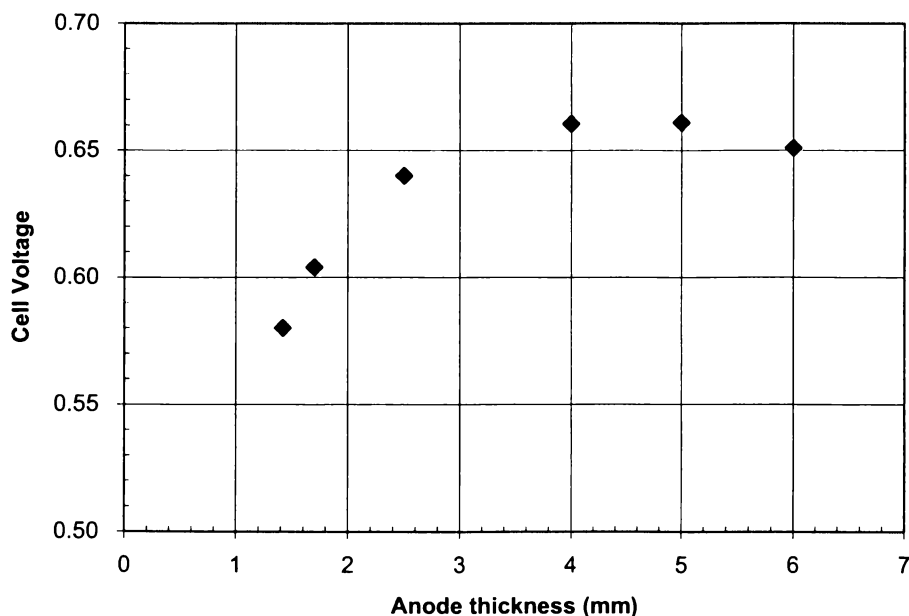


Figure 5-12 Cell performance change due to anode thickness

Increasing the thickness of the anode shows promising results, with significant increases in performance with small increases in thickness. Figure 5-12 highlights

the fact that an optimal anode thickness will exist, beyond which increasing the anode thickness leads to a drop in overall performance. Mass-transfer becomes the limiting factor at higher thicknesses, as shown in Figure 5-13.

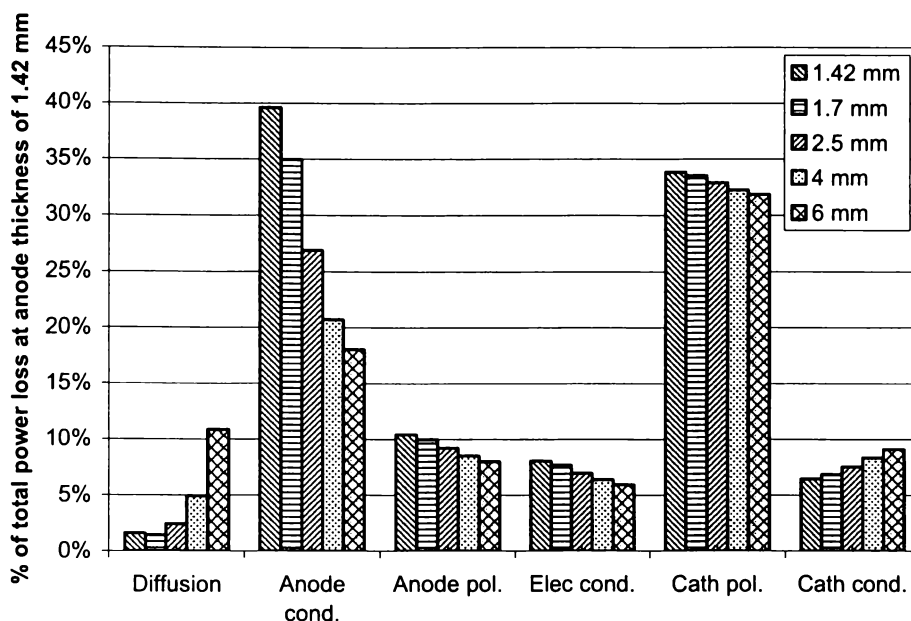


Figure 5-13 Change in component losses at various anode thicknesses (relative to 1.4 mm).

It should be noted that this analysis only considers diffusion effects associated with increasing the anode thickness, and does not consider the impact a thicker anode will have on other parameters, such as the exchange current density.

5.3 Conclusions

An analysis of the components of an anode supported tubular solid oxide fuel cell has been made. Losses attributed to each component have been determined for a selection of geometries, highlighting the dominance of the cathode polarization and anode conduction losses in all cases. Further analyses provide potential performance improvements if these components can be enhanced. In particular, the addition of a metallic insert inside the cell is shown to yield a moderate

performance benefit with minimal engineering effort, and is supported by experimental results.

5.3.1 Recommended Component Focus

Further experimental study of the cathode performance would be beneficial, to validate the extreme impact this component has on cell performance. Composition and active area experiments would be most helpful at this early stage of development.

Anode thickness studies could deliver information leading to improved cell performance, as well as a refined cell model. That is, a further refined model could be used to back calculate changes in anodic overpotential due to thickness. Calculations of this nature would be contingent on a discrete parameterization of overpotentials (rather than the empirical fit used at present).

5.4 References

1. Chan, S. H., Khor, K. A. & Xia, Z. T. A complete polarization model of a solid oxide fuel cell and its sensitivity to the change of cell component thickness. *Journal of Power Sources* **93**, 130-140 (2001).
2. Boersma, R. J., Sammes, N. M. & Fee, C. J. Losses resulting from in-plane electricity conduction in tubular solid oxide fuel cells. *Solid State Ionics* **135**, 493-502 (2000).
3. Fernandes, N. Unpublished results, Acumentrics Corporation (2004).

6 Development of a Generic Distributed Computation Interface

6.1 Introduction

The potential for distributed computing modelling of fuel cells can not be realized without a distribution interface for models more advanced than the simple ladder network detailed in chapter 3. To that end, the interface presented previously is modified to allow for the solution of finite element models specified through the Matlab modelling language ‘m’. Femlab finite element models can be specified and executed through a Matlab ‘m-file’ interface, so the finite element model developed in this thesis is used in the test method.

6.2 Distributed Computation with Matlab

The Visual Basic application described previously (see chapter 3) required extensive modification to achieve this goal, as well as the addition of some new components to interface with Matlab. Matlab 6, used for this project, provides an automation server of its own; however, it does not support asynchronous execution. Therefore the first component required for this distribution interface is a Matlab application wrapper. An application wrapper takes the functionality of an application (in this case Matlab) and provides it through an alternative interface (the MatAppWrap class) performing manipulations as necessary. The wrapper nomenclature arises from the understanding that the application presents the functionality in an alternative form, or wrapper. In this instance the wrapper class adds an asynchronous execution method and a completion notification event.

The Matlab wrapper class is compiled into an ActiveX component (MatWrap.exe). Both the client and server applications, outlined previously, can use the Matlab wrapper application to interface asynchronously with local installations of Matlab. A sample program flow, showing the effects of asynchronous call-backs and the Matlab wrapper, is outlined in Figure 6-1.

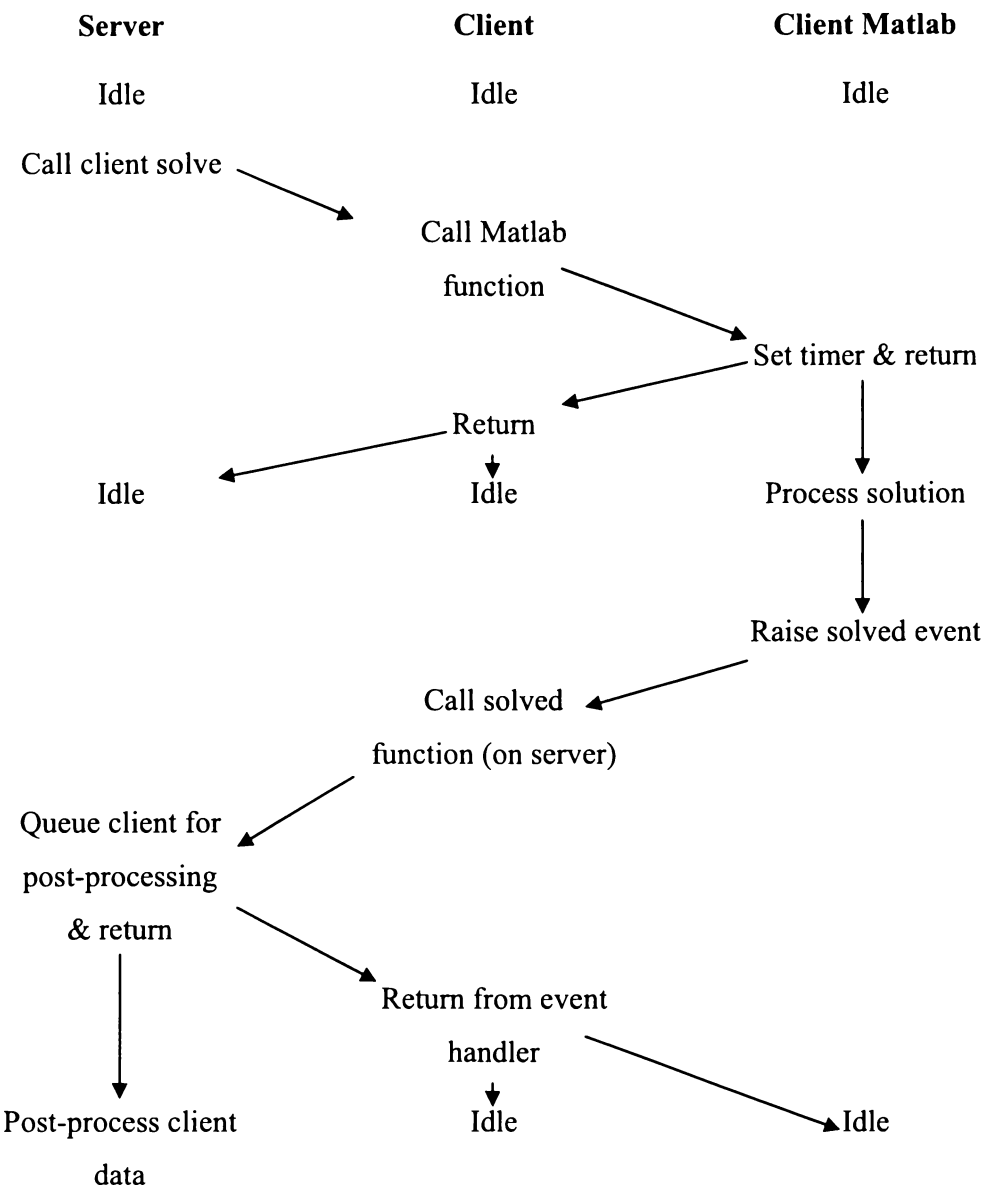


Figure 6-1 Client and server application status during asynchronous solution processing.

The ‘Idle’ nomenclature in Figure 6-1 does not mean that the computer is idle, just that the particular application is responsive and, in the case of the server, can be processing other information. It should be noted that the Matlab wrapper component will be unresponsive while it is awaiting a Matlab solution; however, the client is responsive, due to the asynchronous execution in the Matlab wrapper. Arrows between the server and client applications (in Figure 6-1) rely on features

of the remote automation library provided with Visual Basic, and can incur reasonable overhead while waiting on remote machine response. Mitigating this delay, (which would be essential in an internet distributed application and could increase the performance of a large-scale local network application) could be achieved with a message passing interface. In a message passing scheme, the server would send a message to a client (e.g. execute command xxx) without notification. Once the client receives the command it could (optionally) send an acknowledgement. This would require that the client and server have open “listening” ports, or that a connection be maintained between the server and each client at all times. Additionally, a protocol would need to be defined to manage communications between the two applications.

Modifications to the Server user interface can be seen in Figure 6-2 (compare with original user interface in section 3.2.1). All of the pertinent paths and files are specified directly on the main screen, although this could be relocated to a configuration form, as before.

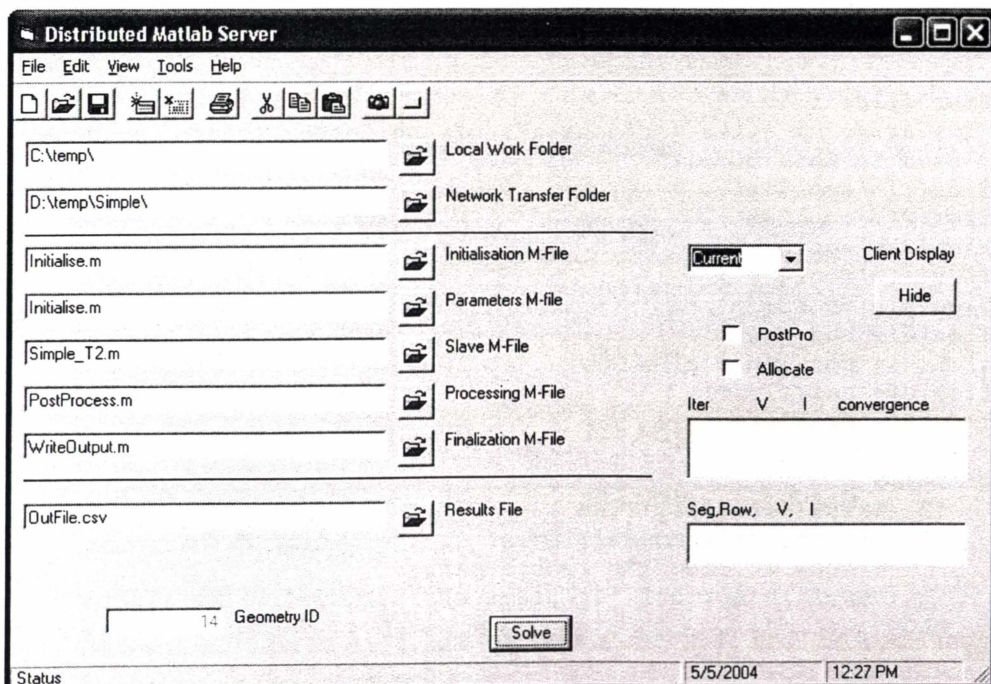


Figure 6-2 Modified user interface for the distributed Matlab server.

Transfer of the model data and code is achieved through a shared location on the local area network (LAN). For models composed of multiple m-files, a top level m-file must be written to perform the file copying, launching of the client side solution, and, write back of solution data to the network share. For the purposes of this demonstration, the file copying process is added to the top-level m-file, as shown in Figure 6-3, with the only result being returned in the m-file return variable (as a string).

Client and server behaviour are as described in section 3.2.2, except that the solution routine in the client and the outer-iterations of the server, are rendered in m-files.

The cell model used is an unrefined (early version) of the finite element model used in chapters 4 and 5.

```

function Icell = Full_test2(localPath, GeomID, remotePath, ...
                           OutFile, index, Ucell, Temps)
% cell013_H2_DC takes the cell voltage as input, and returns
% the cell current.
% This early version gives little flexibility, but will allow
% testing of the COM object.

clear files i
% The array of files includes all of the "non-standard" m-files
% used in this model.
files{1}='appl1.m';
files{2}='appl2.m';
files{3}='appl3.m';
files{4}='appl4.m';
files{5}='fcGeom.m';
files{6}='bnd_gen.m';
files{7}='equ_gen.m';
files{8}='datTrim.m';
files{9}='PostInteg.m';

for i=1:9
    if (exist(files{i}, 'file') ~= 2)
        %If the file doesn't exist in the m-file path,
        % copy it from the remote path.
        copyfile(sprintf('%s',remotePath,files{i}),localPath);
    end
end

```

Figure 6-3 File copy setup for distributed Matlab.

6.3 Results & Discussion

A stack model is considered using the geometry described in section 3.2.1, Figure 3-4 (page 57). Each row in the stack consists of 3 cells, connected in parallel, and there are four such rows, connected in series electrically. A fixed stack current of 18 Amps is required. An initial cell voltage of 0.7 V is used.

A dedicated server is used, starting with a single client (at 4:09 PM), and adding two additional clients (at 4:28 PM and 4:29 PM). Progression of the three clients can be seen in Figure 6-4, with pertinent specifications shown in Table 6-1. Client 0 shows clearly superior performance, which is easily explained by the differences between the machines. RAM is the primary factor in the solution of this finite element model, as is evidenced (in Figure 6-4) by the fact that Client 2 with a slower CPU provides better performance than Client 1. Table 6-1 shows Client 0 as a P4-1.5 GHz, whereas it is, in fact, a Pentium 4, 3.0 GHz machine. Its processing performance is somewhat retarded by the fact that the CPU has “hyper-threading” enabled, which makes the CPU appear as two distinct CPUs. Matlab, can only use a single CPU, and thus only ever achieves a 50% load on this machine.

Table 6-1 Computer specifications

Name	CPU	Speed	RAM
Client 0	Pentium 4	1500 MHz	1024 MB
Client 1	Pentium III	1000 MHz	256 MB
Client 2	Pentium III	733 MHz	512 MB
Server	Pentium III	733 MHz	128 MB

The variability introduced by a lack of system memory, and the concomitant necessity to use virtual memory, is a possible explanation for the change in performance of Client 1. Figure 6-5 highlights this variability, and the magnitude and irregularity of the variation suggests that another process may be active on

Client 1, and is detracting from the performance (Client 1 subsequently experienced a hard disk failure which may be related).

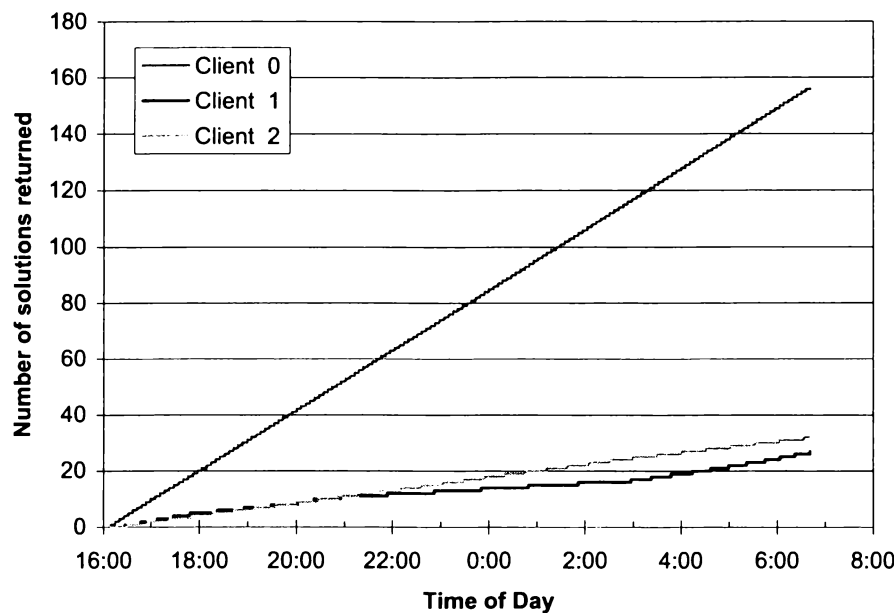


Figure 6-4 Solution performance of each client.

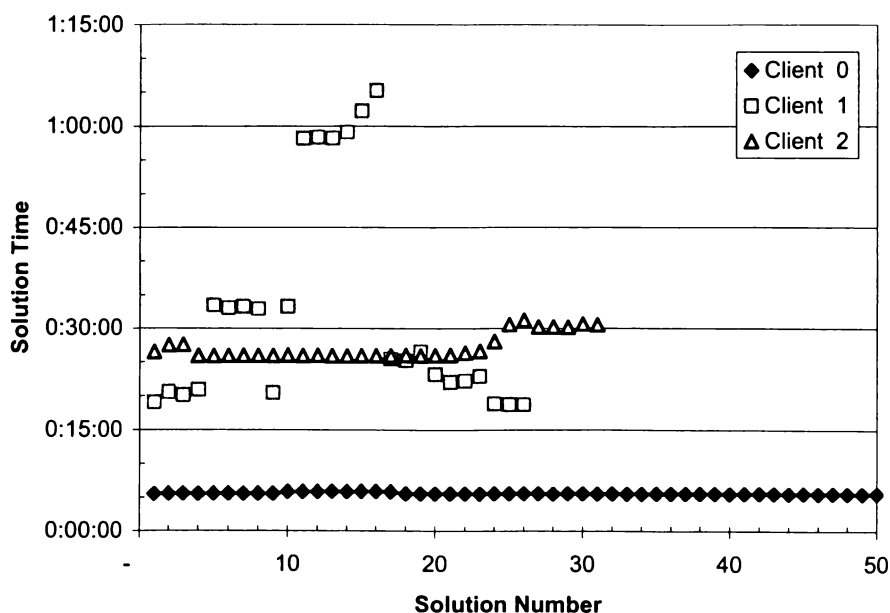


Figure 6-5 Solution processing times for each client.

As all of the cells in this model are identical, with identical fuel flows, and identical uniform temperature, the solution requires that each cell produces exactly 6 Amps. While the solution failed to terminate correctly, all cells had returned a current of 6.0003 Amps after three global iterations. Table 6-3 shows a reformatted excerpt from the solution log, giving the server processing entries. Using the initial voltage of 0.7 V, Table 6-3 shows that a cell current of 5.7159 Amps is attained at 0.7 V. Subsequently a cell voltage of 0.6801 yields 6.0412 Amps, and 0.6826 provides the final (not shown) result of 6.0003 Amps.

All rows had returned the required current after 2:46:10, which can be considered the total solution time. Extrapolating for Client 0, using the average solution time of 5:35 for Client 0 (note range 5:33 to 5:55, so average is close to minimum) the 12 solutions required (4 rows by 3 cells) and 3 iterations give a total time of 3:21:00. Hence the solution time for the distributed model is reduced to 83% of the best single-client time, with the additional clients being far below the initial client's performance. A similar analysis based on Client 2 leads to a solution time reduction to 18% of the single-client time.

A more useful metric, the net CPU utilization, is derived from the ratio of total beneficial CPU time to total active CPU time. Table 6-2 provides the solution statistics for the three clients. Accounting for the differing start times the net CPU utilization is 97%. Calculating the total time from the first client start time to the last client end time yields an 89% net CPU utilization.

Table 6-2 Distributed solution statistics.

	Client 0	Client 1	Client 2
Start time	16:09:22	16:28:14	16:29:02
Last used solution	18:53:28	18:55:30	18:42:36
Solutions returned	29	6	5

As the division of time between client processing and overhead (communications and server processing) is far more disparate than the case outlined in chapter 3, the client scaling is almost ideal (very little time is spent in communications). This suggests that if three high performance machines were available, the solution time would likely be close to one-third of the unit time. It is difficult to estimate at what point the communications network and server performance would become limiting factors, but with long solution times and very small data transfers it could realistically be hundreds of machines. As such, limitations imposed by the model geometry are likely to come into play first. For this sample stack, no more than 12 clients could be used (one for each cell), and there would be delays associated with the performance disparities of the clients. However, with a realistic stack consisting of hundreds of cells, far more clients could be utilised.

Table 6-3 Results log excerpt.

Time	Command (row, cell, Amps)	Result (row, new Voltage)
4:14:55 PM	PostProcess(1, 1, 5.7159)	0
4:20:30 PM	PostProcess(1, 2, 5.7159)	0
4:26:04 PM	PostProcess(1, 3, 5.7159)	1 0.6801
4:31:38 PM	PostProcess(2, 1, 5.7159)	0
4:37:13 PM	PostProcess(3, 1, 5.7159)	0
4:42:47 PM	PostProcess(3, 2, 5.7159)	0
4:47:17 PM	PostProcess(2, 2, 5.7159)	0
4:48:22 PM	PostProcess(3, 3, 5.7159)	3 0.6801
4:53:56 PM	PostProcess(4, 2, 5.7159)	0
4:55:35 PM	PostProcess(2, 3, 5.7159)	2 0.6801
4:59:32 PM	PostProcess(4, 3, 5.7159)	0
5:05:25 PM	PostProcess(1, 2, 6.0412)	0
5:07:52 PM	PostProcess(4, 1, 5.7159)	4 0.6801
5:11:17 PM	PostProcess(1, 3, 6.0412)	0
5:17:10 PM	PostProcess(3, 2, 6.0412)	0
5:23:03 PM	PostProcess(3, 3, 6.0412)	0
5:23:08 PM	PostProcess(1, 1, 6.0412)	1 0.6826
5:28:00 PM	PostProcess(3, 1, 6.0412)	3 0.6826
5:28:56 PM	PostProcess(2, 1, 6.0412)	0
5:34:50 PM	PostProcess(4, 1, 6.0412)	0
5:40:43 PM	PostProcess(4, 2, 6.0412)	0
5:46:36 PM	PostProcess(4, 3, 6.0412)	4 0.6826
5:48:57 PM	PostProcess(2, 3, 6.0412)	0
5:50:44 PM	PostProcess(2, 2, 6.0412)	2 0.6826

While this model is simplistic, a more detailed model could include a detailed flow model on the cathode side of the cells. This would be considerably more complex, and promotes more rigorous partitioning. The introduction of a client identifier could allow the server to identify high-performance clients, although additional intelligence would be required in the server to delineate the problem. Beyond this, the server could track the performance of clients, or collect pertinent

statistics from clients, in order to better determine the ability of clients. An alternative approach would be to run two networks, a high performance network, and a low performance network, implementing data sharing directly between the servers, or through a shared network resource.

6.4 Conclusions

Detailed modelling of fuel cells using distributed techniques has been shown to be not only feasible but to yield measurable performance benefits. Testing with three client computers showed that 97% of the CPU cycles of the three machines were used in the solution of the problem. While an extrapolation has been made from these results to suggest that multiple high-performance clients could yield excellent performance results, a more useful observation follows. The performance of distributed fuel cell models can be enhanced by the addition of low-performance client machines, which could be optimized by intelligent problem partitioning. Utilizing low-performance PCs in the solution of fuel cell models could ease the financial burden on both academic and private sector entities, allowing currently deployed computers to make a significant contribution to intensive fuel cell analysis.

7 Conclusions & Further Work

7.1 Conclusions

7.1.1 Finite Element Solid Oxide Fuel Cell Model

A detailed model of a tubular solid oxide fuel cell has been developed in the generic finite element modelling package FEMLAB. The model has produced results that correlate well with experimental data and has proven a useful design tool in a commercial environment[†].

A sensitivity analysis demonstrated the significant role played by both the electrical conductivity of the anode and the activation overpotential at the cathode making up 40% and 34% respectively of the total losses at a nominal operating current. Further study revealed a 15% decrease in anode resistive losses with the addition of a porous metallic insert, in direct agreement with experimental results. This corresponds to a decrease in overall losses of 6.6% or an increase in cell voltage (and hence power) of 4.7%.

Increasing the cathode exchange current density to a value expressed in the literature was modelled to lower the overall loss by 23%, increasing power output by 13%. However, this is a factor of 10 improvement over the only data available. Increasing the cathode exchange current density by a factor of 4 reduces the improvement to a 15% reduction in losses or 8.4% increase in power output.

7.1.2 Distributed Computing for Fuel Cell Modelling

A feasibility study (chapter 3) showed the potential for distributed computing techniques to be applied to fuel cell models, showing a good improvement in performance with the addition of computers to the problem. Specifically, a linear increase in communications overhead was seen with the addition of clients and excluding this overhead gave close to ideal scaling. Subsequently (chapter 6), a

[†] Acumentrics Corporation, a developer/manufacturer of solid oxide fuel cells.

proof-of-concept software package was developed for the distributed solution of arbitrarily complex systems and was applied to a fuel cell stack model of detailed finite element cells. Initial testing showed that three computers could be applied to the problem in parallel, with 97% of the total CPU cycles contributing to the solution. Even with extremely mismatched computers (one computer performed 73% of the computations), the solution time was reduced by 17% over the best single computer, giving a concrete demonstration of the power of distributed computing for fuel cell modelling.

7.2 Further Work

7.2.1 Cell Modelling

The most beneficial improvement to the finite element model would be the addition of thermal effects. A simple starting point would be to specify an inlet fuel temperature, and a convective boundary at the cathode. However, a method for applying the generated heat is less obvious. The heat (other than resistive heating in the electrodes) can be calculated from the overpotential terms, however, these are determined by the cross-electrolyte current density, leaving no solid body to apply a heat generation rate to. Thus a line source is created between the two electrodes, but FEMLAB does not implement such a source.

Activation overpotential calculations should be separated into individual electrode contributions to better study these effects. However, initial trials have shown such a system to be unstable so additional effort is required here.

Additional effort should also be directed to hydrocarbon modelling, at least including a CO-CO₂ system. Again, a FEMLAB limitation comes about in that only four species can be modelled in the Stefan-Maxwell system. Hence a fully steam-reformed stream could be considered, but there are insufficient species to model a partial-oxidation stream. In-situ reforming is also out of the question for even the simplest reaction mechanisms, again due to the species limitation. One possible avenue is to define multiple coupled systems, with a number of active species (less than four each) and one or more balance species which are a summation of all remaining species. For example, a methane-steam system could

possibly be modelled as two systems; $\text{H}_2 | \text{H}_2\text{O} | \text{CO} + \text{CO}_2 | \text{CH}_4$ and $\text{CO} | \text{CO}_2 | \text{CH}_4 + \text{H}_2\text{O} | \text{H}_2$. Such a system would likely be extremely unstable.

7.2.2 Experimental Studies

The extremely low exchange current density measured for the cathode (approximately one-tenth of the standard literature value) is a major cause for concern. Further experimental work should be directed at characterising the cathode and improving its performance.

Additional study of various cell lengths has already begun and these results will be extremely useful both for characterising the model and for optimising the cell design. Central to the length limitation is the resistive losses in the anode. Increasing the anode thickness could alleviate this problem but other issues arise, most notably diffusive mass-transfer limitations.

7.2.3 Distributed Computing

Improving the presentation of the software, as it stands, and providing detailed documentation would allow researchers in many disciplines to make use of distributed computing resources with minimal effort. To further leverage distributed computing for fuel cell modelling requires a detailed stack model including a domain partitioning scheme. To this end, the development of a stack section (including a cell and surrounding volume) should be pursued to facilitate a detailed stack model.

Appendix A Distributed FEM

Results Log Files

A.1 Solution.log

```
12:00:00 AM  Solution Started ...
16:09:19.9 Flow Setup Started ...
16:09:21.9 Starting Solution ...
16:09:21.9 Clients Initialised.
16:09:22.0 Row 101 allocated to client 0
16:14:55.1Solution from Client 0
1/1/2003 4:14:55 PM  Commence Postprocess. Row 101
16:14:55.2 Row 102 allocated to client 0
16:20:30.1Solution from Client 0
1/1/2003 4:20:30 PM  Commence Postprocess. Row 102
16:20:30.2 Row 103 allocated to client 0
16:26:04.5Solution from Client 0
1/1/2003 4:26:04 PM  Commence Postprocess. Row 103
16:26:04.6 Row 201 allocated to client 0
16:28:14.3 Row 202 allocated to client 1
16:29:01.9 Row 203 allocated to client 2
16:31:38.9Solution from Client 0
1/1/2003 4:31:38 PM  Commence Postprocess. Row 201
16:31:38.0 Row 301 allocated to client 0
16:37:12.7Solution from Client 0
1/1/2003 4:37:13 PM  Commence Postprocess. Row 301
16:37:13.9 Row 302 allocated to client 0
16:42:47.5Solution from Client 0
1/1/2003 4:42:47 PM  Commence Postprocess. Row 302
16:42:47.7 Row 303 allocated to client 0
16:47:17.7Solution from Client 1
1/1/2003 4:47:17 PM  Commence Postprocess. Row 202
16:47:18.8 Row 401 allocated to client 1
16:48:22.3Solution from Client 0
1/1/2003 4:48:22 PM  Commence Postprocess. Row 303
16:48:22.4 Row 402 allocated to client 0
16:53:56.7Solution from Client 0
1/1/2003 4:53:56 PM  Commence Postprocess. Row 402
16:53:56.9 Row 403 allocated to client 0
16:55:35.1Solution from Client 2
1/1/2003 4:55:35 PM  Commence Postprocess. Row 203
16:55:35.3 Row 101 allocated to client 2
16:59:31.6Solution from Client 0
1/1/2003 4:59:32 PM  Commence Postprocess. Row 403
16:59:32.7 Row 102 allocated to client 0
17:05:25.2Solution from Client 0
1/1/2003 5:05:25 PM  Commence Postprocess. Row 102
17:05:25.4 Row 103 allocated to client 0
17:07:52.5Solution from Client 1
1/1/2003 5:07:52 PM  Commence Postprocess. Row 401
17:07:53.7 Row 301 allocated to client 1
```

```
17:11:17.0Solution from Client 0
1/1/2003 5:11:17 PM Commence Postprocess. Row 103
17:11:18.2 Row 302 allocated to client 0
17:17:10.2Solution from Client 0
1/1/2003 5:17:10 PM Commence Postprocess. Row 302
17:17:10.4 Row 303 allocated to client 0
17:23:03.7Solution from Client 0
1/1/2003 5:23:03 PM Commence Postprocess. Row 303
17:23:03.9 Row 201 allocated to client 0
17:23:08.6Solution from Client 2
1/1/2003 5:23:08 PM Commence Postprocess. Row 101
17:23:08.7 Row 202 allocated to client 2
17:28:00.3Solution from Client 1
1/1/2003 5:28:00 PM Commence Postprocess. Row 301
17:28:01.4 Row 203 allocated to client 1
17:28:56.0Solution from Client 0
1/1/2003 5:28:56 PM Commence Postprocess. Row 201
17:28:56.1 Row 401 allocated to client 0
17:34:50.7Solution from Client 0
0

1/1/2003 5:34:50 PM Commence Postprocess. Row 401
17:34:50.9 Row 402 allocated to client 0
17:40:43.7Solution from Client 0
1/1/2003 5:40:43 PM Commence Postprocess. Row 402
17:40:43.9 Row 403 allocated to client 0
17:46:36.9Solution from Client 0
1/1/2003 5:46:36 PM Commence Postprocess. Row 403
17:46:36.1 Row 101 allocated to client 0
17:48:57.8Solution from Client 1
1/1/2003 5:48:57 PM Commence Postprocess. Row 203
17:48:57.0 Row 102 allocated to client 1
17:50:44.5Solution from Client 2
1/1/2003 5:50:44 PM Commence Postprocess. Row 202
17:50:44.7 Row 103 allocated to client 2
17:52:10.2Solution from Client 0
1/1/2003 5:52:10 PM Commence Postprocess. Row 101
17:52:10.3 Row 301 allocated to client 0
17:57:44.1Solution from Client 0
1/1/2003 5:57:44 PM Commence Postprocess. Row 301
17:57:44.1 Row 302 allocated to client 0
18:03:19.1Solution from Client 0
1/1/2003 6:03:19 PM Commence Postprocess. Row 302
18:03:19.2 Row 303 allocated to client 0
18:08:53.3Solution from Client 0
1/1/2003 6:08:53 PM Commence Postprocess. Row 303
18:08:53.4 Row 401 allocated to client 0
18:14:28.0Solution from Client 0
1/1/2003 6:14:28 PM Commence Postprocess. Row 401
18:14:28.1 Row 402 allocated to client 0
18:16:39.6Solution from Client 2
1/1/2003 6:16:39 PM Commence Postprocess. Row 103
18:16:40.8 Row 403 allocated to client 2
18:20:01.3Solution from Client 0
1/1/2003 6:20:01 PM Commence Postprocess. Row 402
18:20:01.4 Row 201 allocated to client 0
18:22:25.0Solution from Client 1
1/1/2003 6:22:25 PM Commence Postprocess. Row 102
18:22:26.0 Row 202 allocated to client 1
```

```
18:25:36.8Solution from Client 0
1/1/2003 6:25:36 PM Commence Postprocess. Row 201
18:25:36.8 Row 203 allocated to client 0
18:31:10.8Solution from Client 0
1/1/2003 6:31:10 PM Commence Postprocess. Row 203
18:31:10.9 Row 101 allocated to client 0
18:36:45.8Solution from Client 0
1/1/2003 6:36:45 PM Commence Postprocess. Row 101
18:36:45.9 Row 301 allocated to client 0
18:42:19.7Solution from Client 0
1/1/2003 6:42:19 PM Commence Postprocess. Row 301
18:42:19.8 Row 302 allocated to client 0
18:42:36.5Solution from Client 2
1/1/2003 6:42:36 PM Commence Postprocess. Row 403
18:42:36.5 Row 303 allocated to client 2
18:47:53.2Solution from Client 0
1/1/2003 6:47:53 PM Commence Postprocess. Row 302
18:47:53.3 Row 401 allocated to client 0
18:53:27.7Solution from Client 0
1/1/2003 6:53:27 PM Commence Postprocess. Row 401
```

```
18:53:27.8 Row 103 allocated to client 0
18:55:29.9Solution from Client 1
1/1/2003 6:55:30 PM Commence Postprocess. Row 202
18:55:30.0 Row 402 allocated to client 1
18:59:02.8Solution from Client 0
1/1/2003 6:59:02 PM Commence Postprocess. Row 103
18:59:02.9 Row 102 allocated to client 0
19:04:35.0Solution from Client 0
1/1/2003 7:04:36 PM Commence Postprocess. Row 102
19:04:36.1 Row 201 allocated to client 0
19:08:34.1Solution from Client 2
1/1/2003 7:08:34 PM Commence Postprocess. Row 303
19:08:34.2 Row 203 allocated to client 2
19:10:10.6Solution from Client 0
1/1/2003 7:10:10 PM Commence Postprocess. Row 201
19:10:10.7 Row 101 allocated to client 0
19:15:43.0Solution from Client 0
1/1/2003 7:15:43 PM Commence Postprocess. Row 101
19:15:44.1 Row 301 allocated to client 0
19:21:17.3Solution from Client 0
1/1/2003 7:21:17 PM Commence Postprocess. Row 301
19:21:17.4 Row 403 allocated to client 0
19:26:52.2Solution from Client 0
1/1/2003 7:26:52 PM Commence Postprocess. Row 403
19:26:52.3 Row 302 allocated to client 0
19:28:45.4Solution from Client 1
1/1/2003 7:28:45 PM Commence Postprocess. Row 402
19:28:45.5 Row 401 allocated to client 1
19:32:26.7Solution from Client 0
1/1/2003 7:32:26 PM Commence Postprocess. Row 302
19:32:26.8 Row 202 allocated to client 0
19:34:32.8Solution from Client 2
1/1/2003 7:34:32 PM Commence Postprocess. Row 203
19:34:32.9 Row 103 allocated to client 2
19:38:00.6Solution from Client 0
1/1/2003 7:38:00 PM Commence Postprocess. Row 202
19:38:00.7 Row 102 allocated to client 0
```

```

19:43:35.8Solution from Client 0
1/1/2003 7:43:35 PM Commence Postprocess. Row 102
19:43:35.9 Row 303 allocated to client 0
19:49:09.5Solution from Client 0
1/1/2003 7:49:09 PM Commence Postprocess. Row 303
19:49:09.6 Row 201 allocated to client 0
19:54:43.9Solution from Client 0
1/1/2003 7:54:43 PM Commence Postprocess. Row 201
19:54:43.0 Row 101 allocated to client 0
20:00:18.2Solution from Client 0
1/1/2003 8:00:18 PM Commence Postprocess. Row 101
20:00:18.3 Row 301 allocated to client 0
20:00:30.0Solution from Client 2
1/1/2003 8:00:30 PM Commence Postprocess. Row 103
20:00:30.1 Row 403 allocated to client 2
20:01:40.3Solution from Client 1
1/1/2003 8:01:40 PM Commence Postprocess. Row 401
20:01:40.4 Row 402 allocated to client 1
20:05:52.0Solution from Client 0
1/1/2003 8:05:52 PM Commence Postprocess. Row 301
20:05:52.1 Row 302 allocated to client 0
20:11:26.4Solution from Client 0
1/1/2003 8:11:26 PM Commence Postprocess. Row 302
20:11:26.5 Row 203 allocated to client 0
20:17:00.9Solution from Client 0
1/1/2003 8:17:00 PM Commence Postprocess. Row 203
20:17:00.0 Row 202 allocated to client 0
20:22:08.5Solution from Client 1
1/1/2003 8:22:08 PM Commence Postprocess. Row 402
20:22:08.6 Row 102 allocated to client 1
20:22:34.6Solution from Client 0

```

Remainder of file deleted for brevity.

A.2 Communications (Comms.log)

```

16:09:22.0 Setting up Client 0
16:09:22.0 Send basic data
16:09:22.0 Send gas flux & temperature data.
16:09:22.0 Setup Complete.
16:09:22.0 Solving Client 0
1/1/2003 4:14:55 PM Commence Postprocess. Client 0
16:14:55.2 Setting up Client 0
16:14:55.2 Send basic data
16:14:55.2 Send gas flux & temperature data.
16:14:55.2 Setup Complete.
16:14:55.2 Solving Client 0
1/1/2003 4:20:30 PM Commence Postprocess. Client 0
16:20:30.2 Setting up Client 0
16:20:30.2 Send basic data
16:20:30.2 Send gas flux & temperature data.
16:20:30.2 Setup Complete.
16:20:30.2 Solving Client 0
1/1/2003 4:26:04 PM Commence Postprocess. Client 0
16:26:04.6 Setting up Client 0
16:26:04.6 Send basic data

```

```
16:26:04.6 Send gas flux & temperature data.
16:26:04.6 Setup Complete.
16:26:04.6 Solving Client 0
16:28:14.3 Setting up Client 1
16:28:14.3 Send basic data
16:28:14.3 Send gas flux & temperature data.
16:28:14.3 Setup Complete.
16:28:14.3 Solving Client 1
16:29:01.9 Setting up Client 2
16:29:01.9 Send basic data
16:29:01.9 Send gas flux & temperature data.
16:29:01.9 Setup Complete.
16:29:01.9 Solving Client 2
1/1/2003 4:31:38 PM Commence Postprocess. Client 0
16:31:38.0 Setting up Client 0
16:31:38.0 Send basic data
16:31:38.0 Send gas flux & temperature data.
16:31:38.0 Setup Complete.
16:31:38.0 Solving Client 0
1/1/2003 4:37:13 PM Commence Postprocess. Client 0
16:37:13.9 Setting up Client 0
16:37:13.9 Send basic data
16:37:13.9 Send gas flux & temperature data.
16:37:13.9 Setup Complete.
16:37:13.9 Solving Client 0
1/1/2003 4:42:47 PM Commence Postprocess. Client 0
16:42:47.7 Setting up Client 0
16:42:47.7 Send basic data
16:42:47.7 Send gas flux & temperature data.
16:42:47.7 Setup Complete.
16:42:47.7 Solving Client 0
1/1/2003 4:47:17 PM Commence Postprocess. Client 1
16:47:18.8 Setting up Client 1
16:47:18.8 Send basic data
16:47:18.8 Send gas flux & temperature data.
16:47:18.8 Setup Complete.
16:47:18.8 Solving Client 1
1/1/2003 4:48:22 PM Commence Postprocess. Client 0
16:48:22.4 Setting up Client 0
16:48:22.4 Send basic data
16:48:22.4 Send gas flux & temperature data.
16:48:22.4 Setup Complete.
16:48:22.4 Solving Client 0
1/1/2003 4:53:56 PM Commence Postprocess. Client 0
16:53:56.9 Setting up Client 0
16:53:56.9 Send basic data
16:53:56.9 Send gas flux & temperature data.
16:53:56.9 Setup Complete.
16:53:56.9 Solving Client 0
1/1/2003 4:55:35 PM Commence Postprocess. Client 2
16:55:35.3 Setting up Client 2
16:55:35.3 Send basic data
16:55:35.3 Send gas flux & temperature data.
16:55:35.3 Setup Complete.
16:55:35.3 Solving Client 2
1/1/2003 4:59:32 PM Commence Postprocess. Client 0
16:59:32.7 Setting up Client 0
16:59:32.7 Send basic data
16:59:32.7 Send gas flux & temperature data.
```

```
16:59:32.7 Setup Complete.
16:59:32.7 Solving Client 0
1/1/2003 5:05:25 PM Commence Postprocess. Client 0
17:05:25.4 Setting up Client 0
17:05:25.4 Send basic data
17:05:25.4 Send gas flux & temperature data.
17:05:25.4 Setup Complete.
17:05:25.4 Solving Client 0
1/1/2003 5:07:52 PM Commence Postprocess. Client 1
17:07:53.7 Setting up Client 1
17:07:53.7 Send basic data
17:07:53.7 Send gas flux & temperature data.
17:07:53.7 Setup Complete.
17:07:53.7 Solving Client 1
1/1/2003 5:11:17 PM Commence Postprocess. Client 0
17:11:18.2 Setting up Client 0
17:11:18.2 Send basic data
17:11:18.2 Send gas flux & temperature data.
17:11:18.2 Setup Complete.
17:11:18.2 Solving Client 0
1/1/2003 5:17:10 PM Commence Postprocess. Client 0
17:17:10.4 Setting up Client 0
17:17:10.4 Send basic data
17:17:10.4 Send gas flux & temperature data.
17:17:10.4 Setup Complete.
17:17:10.4 Solving Client 0
1/1/2003 5:23:03 PM Commence Postprocess. Client 0
17:23:03.9 Setting up Client 0
17:23:03.9 Send basic data
17:23:03.9 Send gas flux & temperature data.
17:23:03.9 Setup Complete.
17:23:03.9 Solving Client 0
1/1/2003 5:23:08 PM Commence Postprocess. Client 2
17:23:08.7 Setting up Client 2
17:23:08.7 Send basic data
17:23:08.7 Send gas flux & temperature data.
17:23:08.7 Setup Complete.
17:23:08.7 Solving Client 2
1/1/2003 5:28:00 PM Commence Postprocess. Client 1
17:28:01.4 Setting up Client 1
17:28:01.4 Send basic data
17:28:01.4 Send gas flux & temperature data.
17:28:01.4 Setup Complete.
17:28:01.4 Solving Client 1
1/1/2003 5:28:56 PM Commence Postprocess. Client 0
17:28:56.1 Setting up Client 0
17:28:56.1 Send basic data
17:28:56.1 Send gas flux & temperature data.
17:28:56.1 Setup Complete.
17:28:56.1 Solving Client 0
1/1/2003 5:34:50 PM Commence Postprocess. Client 0
17:34:50.9 Setting up Client 0
17:34:50.9 Send basic data
17:34:50.9 Send gas flux & temperature data.
17:34:50.9 Setup Complete.
17:34:50.9 Solving Client 0
1/1/2003 5:40:43 PM Commence Postprocess. Client 0
17:40:43.9 Setting up Client 0
17:40:43.9 Send basic data
```

```
17:40:43.9 Send gas flux & temperature data.
17:40:43.9 Setup Complete.
17:40:43.9 Solving Client 0
1/1/2003 5:46:36 PM Commence Postprocess. Client 0
17:46:36.1 Setting up Client 0
17:46:36.1 Send basic data
17:46:36.1 Send gas flux & temperature data.
17:46:36.1 Setup Complete.
17:46:36.1 Solving Client 0
1/1/2003 5:48:57 PM Commence Postprocess. Client 1
17:48:57.0 Setting up Client 1
17:48:57.0 Send basic data
17:48:57.0 Send gas flux & temperature data.
17:48:57.0 Setup Complete.
17:48:57.0 Solving Client 1
1/1/2003 5:50:44 PM Commence Postprocess. Client 2
17:50:44.7 Setting up Client 2
17:50:44.7 Send basic data
17:50:44.7 Send gas flux & temperature data.
17:50:44.7 Setup Complete.
17:50:44.7 Solving Client 2
1/1/2003 5:52:10 PM Commence Postprocess. Client 0
17:52:10.3 Setting up Client 0
17:52:10.3 Send basic data
17:52:10.3 Send gas flux & temperature data.
17:52:10.3 Setup Complete.
17:52:10.3 Solving Client 0
1/1/2003 5:57:44 PM Commence Postprocess. Client 0
17:57:44.1 Setting up Client 0
17:57:44.1 Send basic data
17:57:44.1 Send gas flux & temperature data.
17:57:44.1 Setup Complete.
17:57:44.1 Solving Client 0
1/1/2003 6:03:19 PM Commence Postprocess. Client 0
18:03:19.2 Setting up Client 0
18:03:19.2 Send basic data
18:03:19.2 Send gas flux & temperature data.
18:03:19.2 Setup Complete.
18:03:19.2 Solving Client 0
1/1/2003 6:08:53 PM Commence Postprocess. Client 0
18:08:53.4 Setting up Client 0
18:08:53.4 Send basic data
18:08:53.4 Send gas flux & temperature data.
18:08:53.4 Setup Complete.
18:08:53.4 Solving Client 0
1/1/2003 6:14:28 PM Commence Postprocess. Client 0
18:14:28.1 Setting up Client 0
18:14:28.1 Send basic data
18:14:28.1 Send gas flux & temperature data.
18:14:28.1 Setup Complete.
18:14:28.1 Solving Client 0
1/1/2003 6:16:39 PM Commence Postprocess. Client 2
18:16:40.8 Setting up Client 2
18:16:40.8 Send basic data
18:16:40.8 Send gas flux & temperature data.
18:16:40.8 Setup Complete.
18:16:40.8 Solving Client 2
1/1/2003 6:20:01 PM Commence Postprocess. Client 0
18:20:01.4 Setting up Client 0
```

```
18:20:01.4 Send basic data
18:20:01.4 Send gas flux & temperature data.
18:20:01.4 Setup Complete.
18:20:01.4 Solving Client 0
1/1/2003 6:22:25 PM Commence Postprocess. Client 1
18:22:26.0 Setting up Client 1
18:22:26.0 Send basic data
18:22:26.0 Send gas flux & temperature data.
18:22:26.0 Setup Complete.
18:22:26.0 Solving Client 1
1/1/2003 6:25:36 PM Commence Postprocess. Client 0
18:25:36.8 Setting up Client 0
18:25:36.8 Send basic data
18:25:36.8 Send gas flux & temperature data.
18:25:36.8 Setup Complete.
18:25:36.8 Solving Client 0
1/1/2003 6:31:10 PM Commence Postprocess. Client 0
18:31:10.9 Setting up Client 0
18:31:10.9 Send basic data
18:31:10.9 Send gas flux & temperature data.
18:31:10.9 Setup Complete.
18:31:10.9 Solving Client 0
1/1/2003 6:36:45 PM Commence Postprocess. Client 0
18:36:45.9 Setting up Client 0
18:36:45.9 Send basic data
18:36:45.9 Send gas flux & temperature data.
18:36:45.9 Setup Complete.
18:36:45.9 Solving Client 0
1/1/2003 6:42:19 PM Commence Postprocess. Client 0
18:42:19.8 Setting up Client 0
18:42:19.8 Send basic data
18:42:19.8 Send gas flux & temperature data.
18:42:19.8 Setup Complete.
18:42:19.8 Solving Client 0
1/1/2003 6:42:36 PM Commence Postprocess. Client 2
18:42:36.5 Setting up Client 2
18:42:36.5 Send basic data
18:42:36.5 Send gas flux & temperature data.
18:42:36.5 Setup Complete.
18:42:36.5 Solving Client 2
1/1/2003 6:47:53 PM Commence Postprocess. Client 0
18:47:53.3 Setting up Client 0
18:47:53.3 Send basic data
18:47:53.3 Send gas flux & temperature data.
18:47:53.3 Setup Complete.
18:47:53.3 Solving Client 0
1/1/2003 6:53:27 PM Commence Postprocess. Client 0
18:53:27.8 Setting up Client 0
18:53:27.8 Send basic data
18:53:27.8 Send gas flux & temperature data.
18:53:27.8 Setup Complete.
18:53:27.8 Solving Client 0
1/1/2003 6:55:30 PM Commence Postprocess. Client 1
18:55:30.0 Setting up Client 1
18:55:30.0 Send basic data
18:55:30.0 Send gas flux & temperature data.
18:55:30.0 Setup Complete.
18:55:30.0 Solving Client 1
1/1/2003 6:59:02 PM Commence Postprocess. Client 0
```

```
18:59:02.9 Setting up Client 0
18:59:02.9 Send basic data
18:59:02.9 Send gas flux & temperature data.
18:59:02.9 Setup Complete.
18:59:02.9 Solving Client 0
1/1/2003 7:04:36 PM Commence Postprocess. Client 0
19:04:36.1 Setting up Client 0
19:04:36.1 Send basic data
19:04:36.1 Send gas flux & temperature data.
19:04:36.1 Setup Complete.
19:04:36.1 Solving Client 0
1/1/2003 7:08:34 PM Commence Postprocess. Client 2
19:08:34.2 Setting up Client 2
19:08:34.2 Send basic data
19:08:34.2 Send gas flux & temperature data.
19:08:34.2 Setup Complete.
19:08:34.2 Solving Client 2
1/1/2003 7:10:10 PM Commence Postprocess. Client 0
19:10:10.7 Setting up Client 0
19:10:10.7 Send basic data
19:10:10.7 Send gas flux & temperature data.
19:10:10.7 Setup Complete.
19:10:10.7 Solving Client 0
1/1/2003 7:15:43 PM Commence Postprocess. Client 0
19:15:44.1 Setting up Client 0
19:15:44.1 Send basic data
19:15:44.1 Send gas flux & temperature data.
19:15:44.1 Setup Complete.
19:15:44.1 Solving Client 0
1/1/2003 7:21:17 PM Commence Postprocess. Client 0
19:21:17.4 Setting up Client 0
19:21:17.4 Send basic data
19:21:17.4 Send gas flux & temperature data.
19:21:17.4 Setup Complete.
19:21:17.4 Solving Client 0
1/1/2003 7:26:52 PM Commence Postprocess. Client 0
19:26:52.3 Setting up Client 0
19:26:52.3 Send basic data
19:26:52.3 Send gas flux & temperature data.
19:26:52.3 Setup Complete.
19:26:52.3 Solving Client 0
1/1/2003 7:28:45 PM Commence Postprocess. Client 1
19:28:45.5 Setting up Client 1
19:28:45.5 Send basic data
19:28:45.5 Send gas flux & temperature data.
19:28:45.5 Setup Complete.
19:28:45.5 Solving Client 1
1/1/2003 7:32:26 PM Commence Postprocess. Client 0
19:32:26.8 Setting up Client 0
19:32:26.8 Send basic data
19:32:26.8 Send gas flux & temperature data.
19:32:26.8 Setup Complete.
19:32:26.8 Solving Client 0
1/1/2003 7:34:32 PM Commence Postprocess. Client 2
19:34:32.9 Setting up Client 2
19:34:32.9 Send basic data
19:34:32.9 Send gas flux & temperature data.
19:34:32.9 Setup Complete.
19:34:32.9 Solving Client 2
```

```
1/1/2003 7:38:00 PM Commence Postprocess. Client 0
19:38:00.7 Setting up Client 0
19:38:00.7 Send basic data
19:38:00.7 Send gas flux & temperature data.
19:38:00.7 Setup Complete.
19:38:00.7 Solving Client 0
1/1/2003 7:43:35 PM Commence Postprocess. Client 0
19:43:35.9 Setting up Client 0
19:43:35.9 Send basic data
19:43:35.9 Send gas flux & temperature data.
19:43:35.9 Setup Complete.
19:43:35.9 Solving Client 0
1/1/2003 7:49:09 PM Commence Postprocess. Client 0
19:49:09.6 Setting up Client 0
19:49:09.6 Send basic data
19:49:09.6 Send gas flux & temperature data.
19:49:09.6 Setup Complete.
19:49:09.6 Solving Client 0
1/1/2003 7:54:43 PM Commence Postprocess. Client 0
19:54:43.0 Setting up Client 0
19:54:43.0 Send basic data
19:54:43.0 Send gas flux & temperature data.
19:54:43.0 Setup Complete.
19:54:43.0 Solving Client 0
1/1/2003 8:00:18 PM Commence Postprocess. Client 0
20:00:18.3 Setting up Client 0
20:00:18.3 Send basic data
20:00:18.3 Send gas flux & temperature data.
20:00:18.3 Setup Complete.
20:00:18.3 Solving Client 0
1/1/2003 8:00:30 PM Commence Postprocess. Client 2
20:00:30.1 Setting up Client 2
20:00:30.1 Send basic data
20:00:30.1 Send gas flux & temperature data.
20:00:30.1 Setup Complete.
20:00:30.1 Solving Client 2
1/1/2003 8:01:40 PM Commence Postprocess. Client 1
20:01:40.4 Setting up Client 1
20:01:40.4 Send basic data
20:01:40.4 Send gas flux & temperature data.
20:01:40.4 Setup Complete.
20:01:40.4 Solving Client 1
1/1/2003 8:05:52 PM Commence Postprocess. Client 0
20:05:52.1 Setting up Client 0
20:05:52.1 Send basic data
20:05:52.1 Send gas flux & temperature data.
20:05:52.1 Setup Complete.
20:05:52.1 Solving Client 0
1/1/2003 8:11:26 PM Commence Postprocess. Client 0
20:11:26.5 Setting up Client 0
20:11:26.5 Send basic data
20:11:26.5 Send gas flux & temperature data.
20:11:26.5 Setup Complete.
20:11:26.5 Solving Client 0
1/1/2003 8:17:00 PM Commence Postprocess. Client 0
20:17:00.0 Setting up Client 0
20:17:00.0 Send basic data
20:17:00.0 Send gas flux & temperature data.
20:17:00.0 Setup Complete.
```

```
20:17:00.0 Solving Client 0
1/1/2003 8:22:08 PM Commence Postprocess. Client 1
```

```
*****  
Remainder of file deleted for brevity.  
*****
```

A.3 Sample Client Log

```
1/1/2003 4:28:14 PM
Full_test2('C:\Temp\',1,'T:\Rhys\temp\',0.7)
```

```
1/1/2003 4:47:16 PM
```

Iter	ErrEst	Damping	Stepsize	nfun	njac	nfac	nbsu
1	1.1e+005	0.1000000	1.2e+005	2	1	1	2
2	6.3	0.1136680	7.1	3	2	2	4
3	1.6	0.1821224	1.9	4	3	3	6
4	0.78	0.1856248	0.94	5	4	4	8
5	0.45	0.2403834	0.57	6	5	5	10
6	0.29	0.2939242	0.39	7	6	6	12
7	0.2	0.4214265	0.32	8	7	7	14
8	0.099	0.7229670	0.27	9	8	8	16
9	0.011	1.0000000	0.18	10	9	9	18
10	9.3e-008	1.0000000	0.039	11	10	10	20
11	9.6e-009	1.0000000	6.7e-006	12	11	11	22
Iter	ErrEst	Damping	Stepsize	nfun	njac	nfac	nbsu
1	1.7e+007	0.1000000	1.9e+007	2	1	1	2
2	0.015	1.0000000	0.24	3	2	2	4
3	0.0022	1.0000000	0.017	4	3	3	6
4	0.00026	1.0000000	0.0029	5	4	4	8
5	0.00011	1.0000000	0.00026	6	5	5	10
6	2.7e-005	1.0000000	0.00011	7	6	6	12
7	9.4e-006	1.0000000	2.7e-005	8	7	7	14
8	3.3e-006	1.0000000	9.4e-006	9	8	8	16
9	9.3e-007	1.0000000	3.3e-006	10	9	9	18

```
ans =
```

```
5.7159
```

```
Results file copy Error: File not found
```

```
1/1/2003 4:47:17 PM
```

```
Full_test2('C:\Temp\',1,'T:\Rhys\temp\',0.7)
```

```
1/1/2003 5:07:51 PM
```

Iter	ErrEst	Damping	Stepsize	nfun	njac	nfac	nbsu
1	1.1e+005	0.1000000	1.2e+005	2	1	1	2
2	6.3	0.1136680	7.1	3	2	2	4
3	1.6	0.1821224	1.9	4	3	3	6
4	0.78	0.1856248	0.94	5	4	4	8
5	0.45	0.2403834	0.57	6	5	5	10
6	0.29	0.2939242	0.39	7	6	6	12
7	0.2	0.4214265	0.32	8	7	7	14
8	0.099	0.7229670	0.27	9	8	8	16

	9	0.011	1.0000000	0.18	10	9	9	18
	10	9.3e-008	1.0000000	0.039	11	10	10	20
	11	9.6e-009	1.0000000	6.7e-006	12	11	11	22
Iter		ErrEst	Damping	Stepsize	nfun	njac	nfac	nbsu
1	1	1.7e+007	0.1000000	1.9e+007	2	1	1	2
2	2	0.015	1.0000000	0.24	3	2	2	4
3	3	0.0022	1.0000000	0.017	4	3	3	6
4	4	0.00026	1.0000000	0.0029	5	4	4	8
5	5	0.00011	1.0000000	0.00026	6	5	5	10
6	6	2.7e-005	1.0000000	0.00011	7	6	6	12
7	7	9.4e-006	1.0000000	2.7e-005	8	7	7	14
8	8	3.3e-006	1.0000000	9.4e-006	9	8	8	16
9	9	9.3e-007	1.0000000	3.3e-006	10	9	9	18

ans =

5.7159

Results file copy Error: File not found
 1/1/2003 5:07:52 PM
 Full_test2('C:\Temp\',1,'T:\Rhys\temp\',0.6801)

1/1/2003 5:27:59 PM

	1	1.1e+005	0.1000000	1.2e+005	2	1	1	2
	2	6.3	0.1136680	7.1	3	2	2	4
	3	1.6	0.1821224	1.9	4	3	3	6
Iter		ErrEst	Damping	Stepsize	nfun	njac	nfac	nbsu
1	1	1.1e+005	0.1000000	1.2e+005	2	1	1	2
2	2	6.3	0.1136680	7.1	3	2	2	4
3	3	1.6	0.1821224	1.9	4	3	3	6
4	4	0.78	0.1856248	0.94	5	4	4	8
5	5	0.45	0.2403834	0.57	6	5	5	10
6	6	0.29	0.2939242	0.39	7	6	6	12
7	7	0.2	0.4214265	0.32	8	7	7	14
8	8	0.099	0.7229670	0.27	9	8	8	16
9	9	0.011	1.0000000	0.18	10	9	9	18
10	10	9.3e-008	1.0000000	0.039	11	10	10	20
11	11	9.6e-009	1.0000000	6.7e-006	12	11	11	22
Iter		ErrEst	Damping	Stepsize	nfun	njac	nfac	nbsu
1	1	1.4e+007	0.1000000	1.6e+007	2	1	1	2
2	2	0.011	1.0000000	0.23	3	2	2	4
3	3	0.0017	1.0000000	0.012	4	3	3	6
4	4	0.00021	1.0000000	0.0022	5	4	4	8
5	5	8.5e-005	1.0000000	0.00021	6	5	5	10
6	6	2.5e-005	1.0000000	8.5e-005	7	6	6	12
7	7	9.2e-006	1.0000000	2.5e-005	8	7	7	14
8	8	3.4e-006	1.0000000	9.2e-006	9	8	8	16
9	9	1e-006	1.0000000	3.4e-006	10	9	9	18
10	10	2.9e-007	1.0000000	1e-006	11	10	10	20

ans =

6.0412

Results file copy Error: File not found
 1/1/2003 5:28:00 PM
 Full_test2('C:\Temp\',1,'T:\Rhys\temp\',0.6801)

1/1/2003 5:48:56 PM

Iter	ErrEst	Damping	Stepsize	nfun	njac	nfac	nbsu
1	1.1e+005	0.1000000	1.2e+005	2	1	1	2
2	6.3	0.1136680	7.1	3	2	2	4
3	1.6	0.1821224	1.9	4	3	3	6
4	0.78	0.1856248	0.94	5	4	4	8
5	0.45	0.2403834	0.57	6	5	5	10
6	0.29	0.2939242	0.39	7	6	6	12
7	0.2	0.4214265	0.32	8	7	7	14
8	0.099	0.7229670	0.27	9	8	8	16
9	0.011	1.0000000	0.18	10	9	9	18
10	9.3e-008	1.0000000	0.039	11	10	10	20
11	9.6e-009	1.0000000	6.7e-006	12	11	11	22

Iter	ErrEst	Damping	Stepsize	nfun	njac	nfac	nbsu
1	1.4e+007	0.1000000	1.6e+007	2	1	1	2
2	0.011	1.0000000	0.23	3	2	2	4
3	0.0017	1.0000000	0.012	4	3	3	6
4	0.00021	1.0000000	0.0022	5	4	4	8
5	8.5e-005	1.0000000	0.00021	6	5	5	10
6	2.5e-005	1.0000000	8.5e-005	7	6	6	12
7	9.2e-006	1.0000000	2.5e-005	8	7	7	14
8	3.4e-006	1.0000000	9.2e-006	9	8	8	16
9	1e-006	1.0000000	3.4e-006	10	9	9	18
10	2.9e-007	1.0000000	1e-006	11	10	10	20

ans =

6.0412

Results file copy Error: File not found
 1/1/2003 5:48:57 PM
`Full_test2('C:\Temp\',1,'T:\Rhys\temp\',0.6826)`

1/1/2003 6:22:24 PM

Iter	ErrEst	Damping	Stepsize	nfun	njac	nfac	nbsu
1	1.1e+005	0.1000000	1.2e+005	2	1	1	2
2	6.3	0.1136680	7.1	3	2	2	4
3	1.6	0.1821224	1.9	4	3	3	6
4	0.78	0.1856248	0.94	5	4	4	8
5	0.45	0.2403834	0.57	6	5	5	10
6	0.29	0.2939242	0.39	7	6	6	12
7	0.2	0.4214265	0.32	8	7	7	14
8	0.099	0.7229670	0.27	9	8	8	16
9	0.011	1.0000000	0.18	10	9	9	18
10	9.3e-008	1.0000000	0.039	11	10	10	20
11	9.6e-009	1.0000000	6.7e-006	12	11	11	22

Iter	ErrEst	Damping	Stepsize	nfun	njac	nfac	nbsu
1	1.4e+007	0.1000000	1.6e+007	2	1	1	2
2	0.011	1.0000000	0.23	3	2	2	4
3	0.0018	1.0000000	0.013	4	3	3	6
4	0.00021	1.0000000	0.0022	5	4	4	8
5	8.7e-005	1.0000000	0.00021	6	5	5	10
6	2.6e-005	1.0000000	8.7e-005	7	6	6	12
7	9.2e-006	1.0000000	2.6e-005	8	7	7	14

8	3.4e-006	1.0000000	9.2e-006	9	8	8	16
9	1e-006	1.0000000	3.4e-006	10	9	9	18

ans =

6.0003

Results file copy Error: File not found
 1/1/2003 6:22:25 PM
 Full_test2('C:\Temp\',1,'T:\Rhys\temp\',0.6826)

1/1/2003 6:55:28 PM

Iter	ErrEst	Damping	Stepsize	nfun	njac	nfac	nbsu
1	1.1e+005	0.1000000	1.2e+005	2	1	1	2
2	6.3	0.1136680	7.1	3	2	2	4
3	1.6	0.1821224	1.9	4	3	3	6
4	0.78	0.1856248	0.94	5	4	4	8
5	0.45	0.2403834	0.57	6	5	5	10
6	0.29	0.2939242	0.39	7	6	6	12
7	0.2	0.4214265	0.32	8	7	7	14
8	0.099	0.7229670	0.27	9	8	8	16
9	0.011	1.0000000	0.18	10	9	9	18
10	9.3e-008	1.0000000	0.039	11	10	10	20
11	9.6e-009	1.0000000	6.7e-006	12	11	11	22
Iter	ErrEst	Damping	Stepsize	nfun	njac	nfac	nbsu
1	1.4e+007	0.1000000	1.6e+007	2	1	1	2
2	0.011	1.0000000	0.23	3	2	2	4
3	0.0018	1.0000000	0.013	4	3	3	6
4	0.00021	1.0000000	0.0022	5	4	4	8
5	8.7e-005	1.0000000	0.00021	6	5	5	10
6	2.6e-005	1.0000000	8.7e-005	7	6	6	12
7	9.2e-006	1.0000000	2.6e-005	8	7	7	14
8	3.4e-006	1.0000000	9.2e-006	9	8	8	16
9	1e-006	1.0000000	3.4e-006	10	9	9	18

ans =

6.0003

Results file copy Error: File not found
 1/1/2003 6:55:29 PM
 Full_test2('C:\Temp\',1,'T:\Rhys\temp\',0.6826)

1/1/2003 7:28:44 PM

Iter	ErrEst	Damping	Stepsize	nfun	njac	nfac	nbsu
1	1.1e+005	0.1000000	1.2e+005	2	1	1	2
2	6.3	0.1136680	7.1	3	2	2	4
3	1.6	0.1821224	1.9	4	3	3	6
4	0.78	0.1856248	0.94	5	4	4	8
5	0.45	0.2403834	0.57	6	5	5	10
6	0.29	0.2939242	0.39	7	6	6	12
7	0.2	0.4214265	0.32	8	7	7	14
8	0.099	0.7229670	0.27	9	8	8	16

```

    9      0.011  1.0000000      0.18   10   9   9   18
   10     9.3e-008 1.0000000      0.039   11   10   10   20
   11     9.6e-009 1.0000000      6.7e-006   12   11   11   22
Iter    ErrEst      Damping      Stepsize nfun njac nfac nbsu
   1     1.4e+007 0.1000000      1.6e+007   2   1   1   2
   2      0.011 1.0000000      0.23   3   2   2   4
   3      0.0018 1.0000000      0.013   4   3   3   6
   4      0.00021 1.0000000      0.0022   5   4   4   8
   5     8.7e-005 1.0000000      0.00021   6   5   5   10
   6     2.6e-005 1.0000000      8.7e-005   7   6   6   12
   7     9.2e-006 1.0000000      2.6e-005   8   7   7   14
   8     3.4e-006 1.0000000      9.2e-006   9   8   8   16
   9     1e-006 1.0000000      3.4e-006  10   9   9   18

```

ans =

6.0003

Section deleted for brevity.

Results file copy Error: File not found
1/2/2003 6:40:56 AM

Full_test2('C:\Temp\',1,'T:\Rhys\temp\',0.6826)

1/2/2003 7:00:34 AM

Iter	ErrEst	Damping	Stepsize	nfun	njac	nfac	nbsu
1	1.1e+005	0.1000000	1.2e+005	2	1	1	2
2	6.3	0.1136680	7.1	3	2	2	4
3	1.6	0.1821224	1.9	4	3	3	6
4	0.78	0.1856248	0.94	5	4	4	8
5	0.45	0.2403834	0.57	6	5	5	10
6	0.29	0.2939242	0.39	7	6	6	12
7	0.2	0.4214265	0.32	8	7	7	14
8	0.099	0.7229670	0.27	9	8	8	16
9	0.011	1.0000000	0.18	10	9	9	18
10	9.3e-008	1.0000000	0.039	11	10	10	20
11	9.6e-009	1.0000000	6.7e-006	12	11	11	22

Iter	ErrEst	Damping	Stepsize	nfun	njac	nfac	nbsu
1	1.4e+007	0.1000000	1.6e+007	2	1	1	2
2	0.011	1.0000000	0.23	3	2	2	4
3	0.0018	1.0000000	0.013	4	3	3	6
4	0.00021	1.0000000	0.0022	5	4	4	8
5	8.7e-005	1.0000000	0.00021	6	5	5	10
6	2.6e-005	1.0000000	8.7e-005	7	6	6	12
7	9.2e-006	1.0000000	2.6e-005	8	7	7	14
8	3.4e-006	1.0000000	9.2e-006	9	8	8	16
9	1e-006	1.0000000	3.4e-006	10	9	9	18

ans =

6.0003

```
Results file copy Error: File not found
```

Appendix B SOFC Materials

SOFC materials are constantly scrutinized in the search for performance improvements. Some of the key improvements sought are:

- Increased ionic conductivity of electrolyte at lower operating temperature
- Improved strength and toughness of all components
- Compatibility and stability of materials
- Enhanced electrical and chemical performance of electrodes

B.1 Electrolytes

The electrolyte forms the basis of a fuel cell and, in a SOFC, conducts oxide ions. Oxide-ion conduction is empirically understood to occur by a process of oxygen vacancy diffusion, and models have successfully described the process [1-4].

B.1.1 Zirconia

Zirconia (zirconium oxide – ZrO_2) has been the base for SOFC electrolytes for many years. In fact, in 1899, Nernst showed that zirconia, when doped with other oxides (e.g. magnesium oxide), is a high temperature ionic conductor [5]. SOFC electrolytes have been yttria (yttrium sesqui-oxide – Y_2O_3) stabilized zirconia (YSZ), for a number of years. In the 1980s the favoured dopant level was 10 mol% yttria (10YSZ) [6], but more recently 8 mol% yttria (8YSZ) is favoured for, although it gives a slightly lower ionic conductivity at lower temperatures, it is stronger than the 10YSZ. The temperature dependence of the ionic conductivity of 8YSZ, prepared from fine powders, has been expressed as $850e^{(-11\ 000/T)}$ S.cm⁻¹ [6], yielding 0.03 S.cm⁻¹ at 800°C and 0.15 S.cm⁻¹ at 1000°C. Alternative trivalent dopants into zirconia have been examined, including scandia (Sc_2O_3) [7-9], gadolinia (Gd_2O_3) [10], and ytterbia (Yb_2O_3) [11]. Analysis of bivalent oxides continues, with studies of magnesia (MgO) [5,12,13] and calcia (CaO) [13-15], but these dopants are widely ignored in favour of higher performance alternatives.

YSZ electrolyte-supported cells need to be operated at high temperatures (typ. $\geq 1000^{\circ}\text{C}$), in order to overcome the relatively high resistance of the electrolyte. With the thinner electrolyte in electrode supported designs, it becomes feasible to operate the cell at much lower temperatures, while still maintaining reasonable performance. Lower temperature also facilitates metallic current collection, which provides improved performance and reduced cost [16]. While an electrode-supported design can help to reduce electrolyte losses, the overall performance of a cell is still dependent on other losses in the system, including activation polarization and electronic resistance.

B.1.2 Ceria

Ceria (cerium oxide – CeO_2) doped with gadolinia, samaria, yttria, or lanthanum has shown promise as an electrolyte material for lower temperature operation, with gadolinia doped Ceria (CGO) receiving the widest attention [17-19]. Problems are known to exist due to the electrolyte becoming electronically conductive in reducing environments. This, however, can be mitigated by eliminating exposure to reducing atmosphere by coating [20], or bi-layer electrolytes [21]. Another perceived difficulty with ceria is that sintering to full density requires high temperatures (1300°C to 1600°C) and long dwell times (up to 10 hours) [17-19], resulting in large grain sizes and hence, poor mechanical stability. The addition of co-dopants has been shown to enhance sinterability, achieving $>99\%$ theoretical density at less than 900°C [22]. However, these solutions are seeing only gradual acceptance, and often inhibit the enhanced conduction of the ceria based materials. Disagreement exists over the optimum ceria content, and the effect of impurities in various ceria sources.

B.1.3 Other Electrolyte Materials

Alternative materials are regularly proposed to serve as the electrolyte for SOFC systems. Lanthanum gallate doped with strontium and magnesium (LSGM), has recently shown high ionic conductivities (0.15 S.cm^{-1} at 800°C) [23-26], and is receiving significant attention. Other electrolytes have been considered, including doped Bi_2O_3 and doped $\text{Ba}_2\text{In}_2\text{O}_5$. Doped $\text{Ba}_2\text{In}_2\text{O}_5$, is a well known fast oxide ion

conductor and, shows promise as a low temperature electrolyte, with a conductivity of $\sim 2.3 \text{ S.cm}^{-1}$ at 727°C [27]. Recently, lanthanum molybdenum oxide ($\text{La}_2\text{Mo}_2\text{O}_9$) has been shown to be a low temperature fast oxide-ion conductor [28,29], yielding a conductivity of $\sim 10 \text{ S.cm}^{-1}$ at 650°C [30].

B.2 Anodes

The anode material for SOFCs is traditionally a nickel-zirconia cermet. This is fabricated from stabilized zirconia and nickel oxide, which are sintered and subsequently, reduced to metallic nickel in a stabilized zirconia matrix. Varying nickel contents have been explored, with the best performance obtained from multi-layered anodes [31]. However, each additional layer increases the cost of the cell, so a trade-off is required. Anodes are commonly 30-40 vol% nickel (after reduction) [6]. Anodes have seen benefit from the use of mixed particle sizes, particularly bi-modal particle size distributions [32]. Manganese additions have been shown to cause a reduction in polarization resistance by factors as great as 5 [33,34], however no optimisation of additive content is forthcoming. Currently published material proposes 2-20% (atomic basis).

Electronic conduction is considered independent of temperature for anodes, and ranges between 300 and 1000 S.cm^{-1} (depending on the specific anode) [6].

Beyond Ni-YSZ, a Ni-TiO₂ cermet anode has been explored, offering the benefit of a thermal expansion in closer agreement with the other components in the system [35]. Ni-TiO₂ has also been extrapolated to titania doped YSZ. This was however dismissed, as the inability to form a single phase at greater than 10 mol% titania did not allow for the expected gains in electronic conductivity. Subsequent analysis by Feighery et al. [36] revealed that concentrations of up to 18 atm% titania were possible by synthesising from ZrO₂, Y₂O₃ and TiO₂, rather than from YSZ and TiO₂ as was previously attempted.

B.3 Cathodes

Strontium doped lanthanum manganite (LSM – eg. $\text{La}_{0.9}\text{Sr}_{0.1}\text{MnO}_3-\delta$) is very much the universally accepted cathode material at temperatures above 850°C . The

addition of iron, as a B-site dopant (Mn substitute), has been shown to reduce both, the polarization resistance and, the electrode activation energy. Electronic conduction is approximately 130 S.cm^{-1} , and, like the anode, is considered independent of temperature [6]. Other cathode materials have been considered, primarily for use with alternative electrolytes, including LSCF, for ceria electrolytes, at temperatures around 500°C .

B.4 Current Collection

Current collection provides the means of connecting a fuel cell to a load. As the primary requirement of this part is electronic conduction, the use of metals is strongly favoured. However, the difference in thermal expansion, between a metallic current collector and ceramic electrodes, is cause for concern in a number of designs. This is especially true in the planar design, wherein, an interconnecting plate provides electrical (series) connection between adjacent cells, and provides gas channels for distributing gases. Thermal expansion mismatch is of particular concern with this flat-plate design.

Planar SOFC have long used strontium doped lanthanum chromite (LSC) as interconnecting material, and this is used also in the Westinghouse and Mitsubishi Heavy Industries tubular designs. This has had the problem of a low electronic conductivity of approximately 30 S.cm^{-1} . Concern has also been expressed at the expansion of LSC in a reducing environment. The addition of 10 mol% magnesium, as a B-site dopant, has been shown to reduce this expansion from 0.35% to 0.13% [37].

In metallic interconnectors, an oxide dispersion strengthened chromium alloy ($\text{Cr}_5\text{Fe}_1\text{Y}_2\text{O}_3$), has been tested in a planar stack [38]. However, chromium poisoning of the cathode has been shown to occur, in the presence of chromium based interconnects, due to the formation of chromium oxides and oxihydroxides [39]. This has been mitigated by a variety of different coatings. Lanthanum coboltite, as well as strontium or calcium doped lanthanum chromites have been shown successful in preventing this, by their coating onto the metallic interconnect [38,40,41].

B.5 References

1. Brinkman, H. W., Briels, W. J. & Verweij, H. Molecular dynamics simulations of yttria-stabilized zirconia. *Chemical Physics Letters* **247**, 386-390 (1995).
2. Li, X. & Hafskjold, B. Molecular dynamics simulations of yttrium-stabilized zirconia. *Journal of Physics Condensed Matter* **7**, 1255-1271 (1995).
3. Okazaki, H., Suzuki, H. & Ihata, K. A possibility of the oxygen diffusion enhancement in YSZ: a molecular dynamics study. *Physics Letters A* **188**, 291-295 (1994).
4. Fisher, C. A. J. & Matsubara, H. Molecular dynamics investigations of grain boundary phenomena in cubic zirconia. *Computational Materials Science* **14**, 177-184 (1999).
5. Nernst, W. On the Electrolytic Conduction of Solid Bodies at High Temperatures. *Zeischrift für Elektrochemie* **6** (1899).
6. Bossel, U. G. in *Final Report on SOFC Data* (International Energy Agency, Berne, 1992).
7. Spiridonov, F. M., Popova, L. N. & Popil'skii, R. Y. On the phase relations and the electrical conductivity in the system ZrO₂-Sc₂O₃. *Journal of solid state chemistry* **2**, 430-438 (1970).
8. Arachi, Y., Asai, T., Yamamoto, O., Takeda, Y., Imanishi, N., Kawate, K. & Tamakoshi, C. in *Solid Oxide Fuel Cells (SOFC VI)* (eds. Singhal, S. C. & Dokiya, M.) 179-184 (The Electrochemical Society, Honolulu, 1999).
9. Mizutani, Y., Kawai, M., Nomura, K., Nakamura, Y. & Yamamoto, O. in *Solid Oxide Fuel Cells (SOFC VI)* (eds. Singhal, S. C. & Dokiya, M.) 185-192 (The Electrochemical Society, Honolulu, 1999).
10. Bhattacharyya, S. & Agrawal, D. C. Preparation of tetragonal ZrO₂-Gd₂O₃ powders. *Journal of Materials Science* **30**, 1495-1499 (1995).
11. Yamamoto, O., Arati, Y., Takeda, Y., Imanishi, N., Mizutani, Y., Kawai, M. & Nakamura, Y. Electrical conductivity of stabilized zirconia with ytterbia and scandia. *Solid State Ionics* **79**, 137-142 (1995).
12. Muccillo, E. N. S. & Kleitz, M. Ionic conductivity of fully stabilized ZrO₂:MgO and blocking effects. *Journal of the European Ceramic Society* **15**, 51-55 (1995).
13. Bateman, C. A. & Notes, M. R. Coarsening kinetics in Mg(Ca, Ti, Y)-partially -stabilized zirconia. *J. Am. Ceram. Soc.* **75**, 1566 (1993).

- 150 Distributed Computing & Solid Oxide Fuel Cell Modelling
14. Nakamura, A. & Wagner, J. B. Defect structure, ionic conductivity, and diffusion in calcia-stabilized zirconia. *J. Electrochem. Soc.* **127**, 2325-2333 (1980).
 15. Patterson, J. W., Bogren, E. C. & Rapp, R. A. Mixed Conduction in Zr_{0.85}Ca_{0.15}O_{1.85} and Th_{0.85}Y_{0.15}O_{1.925} Solid Electrolytes. *Journal of the Electrochemical Society* **114**, 752-758 (1967).
 16. Yamamoto, O. Solid oxide fuel cells: fundamental aspects and prospects. *Electrochimica Acta* **45**, 2423-2435 (2000).
 17. Kim, N., Kim, B. H. & Lee, D. in *Solid Oxide Fuel Cells (SOFC VI)* (eds. Singhal, S. C. & Dokiya, M.) 201-208 (The Electrochemical Society, Honolulu, 1999).
 18. Torrens, R. S., Sammes, N. M., Kendall, K. & Austin, J. C. in *Solid Oxide Fuel Cells (SOFC VI)* (eds. Singhal, S. C. & Dokiya, M.) 209-216 (The Electrochemical Society, Honolulu, 1999).
 19. Wang, S., Kobayashi, T., Dokiya, M. & Hashimoto, T. in *Solid Oxide Fuel Cells (SOFC VI)* (eds. Singhal, S. C. & Dokiya, M.) 193-200 (The Electrochemical Society, Honolulu, 1999).
 20. Mehta, K., Hong, S. J., Jue, J.-F. & Virkar, A. V. in *3rd International Symposium on SOFCs* (eds. Singhal, S. C. & Iwahara, H.) 92-103 (Electrochemical Society, Honolulu, 1993).
 21. Zhu, B. & Mellander, B.-E. in *Solid Oxide Fuel Cells (SOFC VI)* (eds. Singhal, S. C. & Dokiya, M.) 244-253 (The Electrochemical Society, Honolulu, 1999).
 22. Kleinlogel, C. & Gauckler, L. J. in *Solid Oxide Fuel Cells (SOFC VI)* (eds. Singhal, S. C. & Dokiya, M.) 225-232 (The Electrochemical Society, Honolulu, 1999).
 23. Ishihara, T., Matsuda, H. & Takita, Y. Doped LaGaO₃ Perovskite Type Oxide as a New Oxide Ionic Conductor. *J. Am. Chem.* **116**, 3801-3803 (1994).
 24. Feng, M. & Goodenough, J. B. A superior oxide-ion electrolyte. *Eur. J. Solid State Inorg. Chem.* **t.31**, 663-672 (1994).
 25. Huang, P. N., Petric, A. & Ghosh, D. in *Solid Oxide Fuel Cells (SOFC VI)* (eds. Singhal, S. C. & Dokiya, M.) 285-291 (The Electrochemical Society, Honolulu, 1999).
 26. Stevenson, J. W., Armstrong, T. R., Pederson, L. R., Li, J., Lewinsohn, C. A. & Baskaran, S. Effect of A-site cation nonstoichiometry on the properties of doped lanthanum gallate. *Solid State Ionics* **113-115**, 571 (1998).

27. Kakinuma, K., Yamamura, H., Haneda, H. & Atake, T. in *Solid Oxide Fuel Cells (SOFC VI)* (eds. Singhal, S. C. & Dokiya, M.) 327-332 (The Electrochemical Society, Honolulu, 1999).
28. Lacorre, P., Goutenoire, F. & Laligant, Y. Designing fast oxide ion conductors based on $\text{La}_2\text{Mo}_2\text{O}_9$. *Nature* **404**, 856- (2000).
29. Goutenoire, F., Isnard, O. & Lacorre, P. Structural and transport characteristics of the LAMOX family of fast oxide-ion conductors, based on lanthanum molybdenum oxide $\text{La}_2\text{Mo}_2\text{O}_9$. *Journal of Materials Chemistry* **11**, 119- (2001).
30. Georges, S., Goutenoire, F., Altorfer, F., Sheptyakov, D., Fauth, F., Suard, E. & Lacorre, P. Thermal, structural and transport properties of the fast oxide-ion conductors $\text{La}_{2-x}\text{R}_x\text{Mo}_2\text{O}_9$ ($\text{R}=\text{Nd}, \text{Gd}, \text{Y}$). *Solid State Ionics* **161**, 231-241 (2003).
31. Wang, L. S. & Barnett, S. A. Sputter-deposited medium-temperature solid oxide fuel cells with multi-layer electrolytes. *Solid State Ionics* **61**, 273-276 (1993).
32. Itoh, H., Yamamoto, T., Mori, M., Mori, N., Watanabe, T., Horita, T., Sakai, N., Yokokawa, H. & Dokiya, M. in *2nd European SOFC Forum* 453- (Oslo, 1996).
33. Primdahl, S. & Mogensen, M. in *Solid Oxide Fuel Cells (SOFC VI)* (eds. Singhal, S. C. & Dokiya, M.) 530-540 (The Electrochemical Society, Honolulu, 1999).
34. Kawasaki, S. (1992).
35. Taimatsu, H., Toyooka, T., Kaneko, H., Matsukaze, N. & Iwata, T. in *2nd European SOFC Forum* 435- (Oslo, 1996).
36. Feighery, A. J., Fagg, D. P., Irvine, J. T. S. & Kaiser, A. Phase Relations at 1500°C in the Ternary System $\text{ZrO}_2\text{-Y}_2\text{O}_3\text{-TiO}_2$. *J. Solid State Chem.* **143**, 273-276 (1999).
37. Mori, K., Miyamoto, H., Takenobu, K. & Matsudaira, T. in *2nd European SOFC Forum* 541- (Oslo, 1996).
38. Buchkremer, H. P., Diekmann, U. & Stöver, D. in *2nd European SOFC Forum* 221- (Oslo, 1996).
39. Quadakkers, W. J., Greiner, H., Köck, W., Buchkremer, H. P., Hilpert, K. & Stövers, D. in *2nd European SOFC Forum* 297- (Oslo, 1996).
40. Günther, C., Beie, H.-J., Greil, P. & Richter, F. in *2nd European SOFC Forum* 491- (Oslo, 1996).

41. Urbanek, J., Miller, M., Schmidt, H. & Hilpert, K. in *2nd European SOFC Forum* 503- (Oslo, 1996).

Appendix C High Performance Computing

High Performance Computing (HPC) (of which supercomputing is a subset), is not applicable to every problem. A key requirement for HPC is that the problem can be logically broken down into semi-independent sub-problems. The level of separation required delineates HPC technologies, albeit with less than rigid boundaries. For example, vector supercomputers would be seen as an obvious category, but are omitted due to their sporadic implementation in contemporary systems. However, the Earth Simulator super computer is a massively parallel system of vector processing nodes. Further, some large clustered systems are being referred to as massively parallel, while others are labelled as networks of workstations. Subsequently, the following delineation is merely a guide to understanding HPC technologies, and terminology.

Testing of high performance computing solutions is collated on a 6-monthly basis by “Top500 Supercomputer sites”[1], a joint venture of the University of Tennessee, USA; the University of Mannheim, Germany; and the National Energy Research Scientific Computing Center, a US government agency. The test results published are attained on the LINPACK benchmark [2], which requires the solution of a dense system of linear equations with a standardised LU-factorisation algorithm. This benchmark gives an indication of the peak performance of the system under test in billions (10^9) of floating point operations per second (GFLOPS). This peak performance can be compared to the theoretical peak performance of a system (also in GFLOPS). It should be noted that a machine with a low GFLOPS score could still provide a high level of performance in a particular application, but LINPACK scores give a good indication of performance on large systems of linear equations.

C.1 Massively Parallel Processors

Massively Parallel Processors (MPP) is closest to the traditional supercomputer architecture (vector processing). A number of different interconnect topologies are

used, but the essence of MPP is the tight integration of multiple computer processors and memory resources. MPP computers can deal with some of the most complex and interconnected problems, and have long dominated the arena of supercomputing. For example, the “Earth Simulator” (Figure C-1), with 5120 processors and 10 TB of RAM (random access memory), has been ranked as the fastest supercomputer for more than a year, at 35 TFLOPS (10^{12} floating-point operations per second) [1]. The primary limitations of a MPP computer are the cost, and the requirement for customized software. Software must be tailor-made for supercomputer systems, not only to deal with their unique hardware but also, to allow for the distribution of a problem across the many processors, and accessing the distributed memories. However, the tight integration of the processors and memories allows for close coupling between simulation domains.

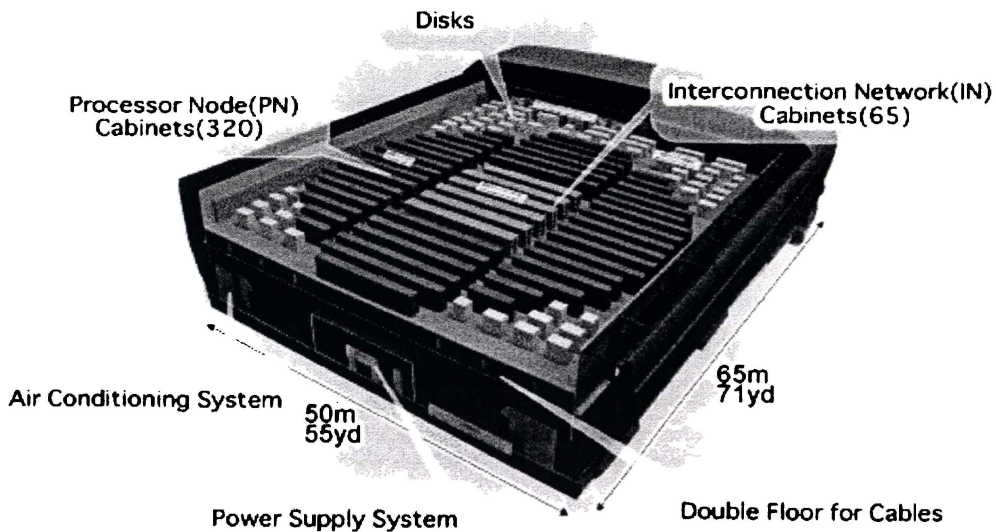


Figure C-1 Earth Simulator floor plan – World's fastest supercomputer (2003) [3]

C.2 Clusters

Clusters [4,5] are one step removed from MPP systems in price and latency. Clusters are composed of commercial off-the-shelf (COTS) systems connected by an interconnect solution (network). The overall performance of a cluster is contingent on the interconnect sub-system and topology; hence, expensive high-speed solutions are often implemented. Clusters are also constrained by the individual components and, more importantly, software.

Cluster operating systems (OS) provide some of the greatest benefits of clusters, but are also the greatest restriction. Cluster OS generally provide a high degree of fault tolerance, being able to detect and partition failed nodes, and/or segments. Additionally, clusters can support dynamic merging and partitioning, allowing for multiple clusters to be dynamically joined for the solution of a complex problem, and partitioned for the solution of multiple simple problems. A cluster still requires that application software be somewhat optimized for it, however, the task is much simplified (from the MPP scenario) by the cluster operating system.

Clusters are having a significant impact on the supercomputer market appearing in the top 5 supercomputers, and accounting for a third of the top 500 supercomputers [1]. Clusters can also achieve favourable price points, as demonstrated by The University of Kentucky's KASY0, the first system to break the \$100 per GFLOPS (10^9 floating-point operations per second) barrier (August 2003) [6]. KASY0, as seen in Figure C-2, is made up of 128 identical desktop computers with a total of 64 GB RAM providing a measured performance of 471.5 GFLOPS, for less than US\$40 000. It should be noted that this measurement (at 32-bit precision) never qualified KASY0 for the top 500 supercomputers, as the top 500 requires a 64-bit precision calculation, in which KASY0 only achieves 187.3 GFLOPS. Ranks 485-500 (June 2003) were held by a Hewlett-Packard Superdome 128 CPU system with 245.30 GFLOPS and a price tag of over \$3 million. November 2003 saw the bottom entry on the top500 supercomputers surpass 400 GFLOPS. Examples of clustering architectures are the Parallel Virtual Machine (PVM) [5], and the Beowulf project [7].

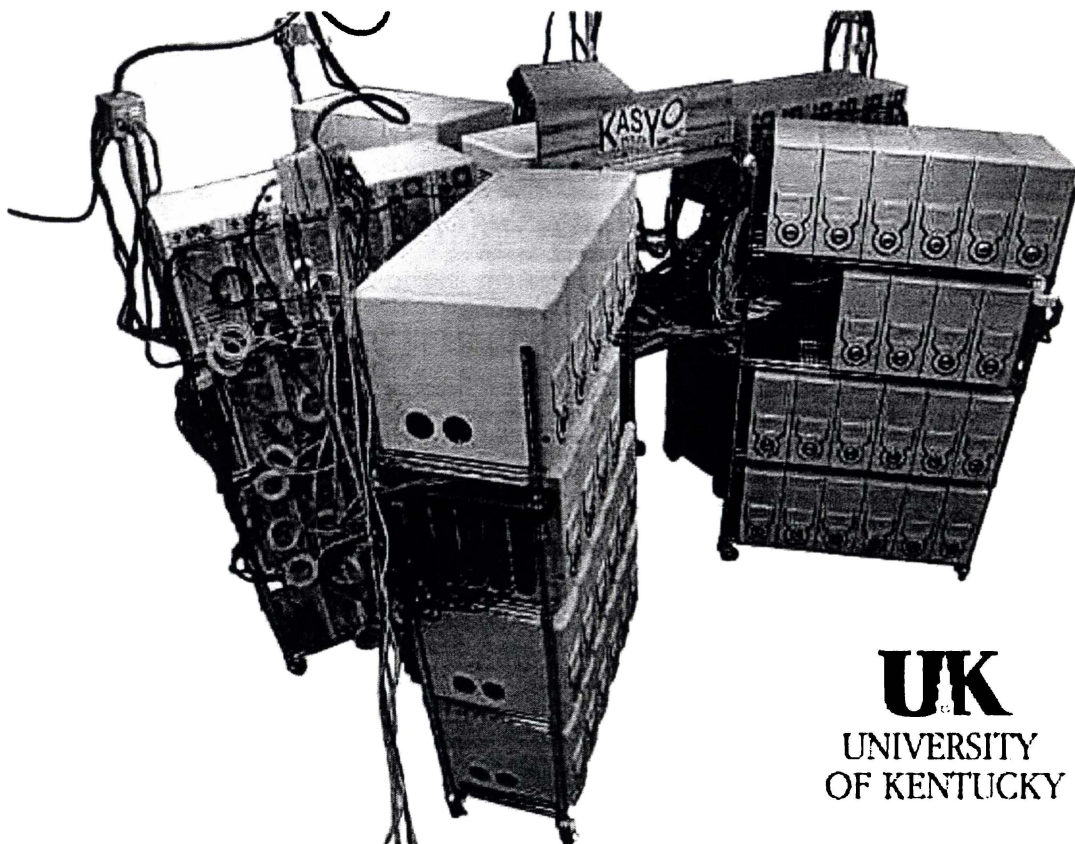


Figure C-2 Kentucky Asymmetric Zero (KASY0) - first supercomputer under \$100/GFLOPS [6]

The interconnect system is usually the determining factor in the performance and price of a cluster. This is perhaps most easily seen in the comparison of some systems from Dell Computer Corporation in Table C-1 (figures from Top500 June 2003). While the complete specifications of these systems are unavailable, Dell's 2003 price for these systems is around \$3000 per node (2 CPUs per node) and the high speed interconnects add approximately \$2000^{\$} per node, while Gigabit (1000T) Ethernet adds approx. \$750^{**} per node. Table C-1 shows that the highest effectiveness (measured GFLOPS divided by theoretical GFLOPS) is attained by the Myrinet and Quadrics high speed networks, however there is little difference in price/performance going to a gigabit (1000T) Ethernet cluster. 100 megabit

^{\$} Approximate pricing from www.quadrics.com and www.myrinet.com, Dec 2003.

^{**} Pricing from froogle.google.com for gigabit switch solutions, Dec 2003.

Ethernet obviously causes a significant bottleneck in a large cluster, impacting both effectiveness and price/performance.

Table C-1 Effect of interconnect on cluster price & performance (all prices approx.)

Processors (number and speed)	Interconnect	Effectiveness		US\$/GFLOPS	
		GFLOPS	Cost US\$000		
128 x 2 @ 2.4 GHz	Quadrics	877.9	71.4%	640	729
128 x 2 @ 2.4 GHz	1000T	618.3	54.9%	480	776
	Ethernet				
64 x 2 @ 2.4 GHz	Myrinet	421.9	68.7%	320	758
64 x 2 @ 2.8 GHz	1000T	383.2	53.5%	240	626
	Ethernet				
288 x 2 @ 2.8 GHz	100T Ethernet	363.4	11.3%	875	2 400

C.3 Networks of Workstations

Networks of workstations (NOW) [8] are the next step down the high performance computing hierarchy, in that each computer is a semi-independent entity. While a cluster is a dedicated computational entity that closely resembles a massively parallel system; a NOW, as the name suggests, is made up of individual workstation computers. A NOW allows for local user interaction at each workstation, and attempts to direct idle workstation resources to the solution of large numerical problems. These systems still rely on an advanced operating system to provide for resource/workload sharing, and have some dependence on a high-speed interconnection method. The greatest hindrance to NOW development is that the software must be tolerant of severe load imbalance and a non-deterministic network. Local user interaction at the workstation is the root cause of both of these problems. Of course, the primary attraction of NOW is that the workstations already exist and, therefore, hardware cost is minimal.

C.4 Distributed computing

Distributed computing refers to the use of geographically dispersed computing resources. Distributed computing had its genesis in the 1970's [9], developing in synergy with supercomputing. Distributed computing led to developments such as the Internet, and the Grid. The Internet grew from a vision of a highly reliable information/communication network. The Grid, conversely, aims to share supercomputing resources between collaborating institutions, focusing less on reliability and more on computational performance. A classic example of co-operative distributed computing is the Internet Domain Name System (DNS). DNS is implemented by a number of co-operating computers (DNS servers), that each store information regarding specific hosts and other DNS servers, allowing for the resolution of host names into IP addresses. When software requires that a domain name be resolved (e.g. www.waikato.ac.nz) it asks the local DNS server, as defined in the TCP/IP settings. If the local server cannot resolve the name, it contacts other DNS servers in a hierarchical fashion (it keeps a list), until it can resolve the name. For example, assuming the local DNS server has no record of ".nz", it will contact its next higher DNS server, which we will assume is one of the root name servers. The root name server will direct the local DNS server to the ".nz" server, which has a record for ".ac.nz", which in turn knows ".waikato.ac.nz", the Waikato University DNS server, which returns the IP address of www.waikato.ac.nz. The robustness of the worldwide web and email attest to the reliability of this highly distributed system.

C.5 Internet Distributed Computing

Internet distributed projects provide the lowest level of connectivity. In this topology, clients (idle computers) request tasks from a central server, which they analyze locally, uploading the results back to the central computer when they are finished. This requires that each set of data be extremely disconnected from other data sets, as clients are only updated through the central server and the server cannot be certain how long it will be before it receives results from a particular client.

Client and server software need to be created to leverage this resource, although careful development will allow the software to be applied to many classes of problems. Unlike less distributed solutions, the operating system requires no particular advanced features and the client can even be designed to function on multiple different operating systems (e.g. SETI@Home [10,11]). In common with the more tightly integrated variants, the Internet distributed workload must be formulated in such a way as to make distribution possible. Specifically, key algorithms may need to be customized for a given problem to facilitate distribution. A prime concern for Internet distributed projects is that a client base must be established. The most well known distributed computing projects are Internet distributed. These include:

- SETI@home [10-12].
Possibly the most well known Internet distributed computing project, SETI@home has been operating since 1999. This project involves clients in the “Search for Extraterrestrial Intelligence”. Data from the Arecibo radio telescope in Puerto Rico is analyzed for extraterrestrial signals.
- Distributed.net [13].
Operating since 1997, this non-profit corporation started providing projects related to breaking cryptographic keys and, more recently, mathematical problems related to cryptography.
- GIMPS [14].
Also operating since 1997, The Great Internet Mersenne Prime Search provides a client that attempts to find the largest prime number of the form $2^P - 1$. Five have been found with the current largest being $2^{13466917} - 1$, in November 2001.

A list of currently active, public, distributed computing projects is available at <http://www.aspenleaf.com/distributed>.

C.6 References

1. Website, *Top 500 Super Computers Trends for June 2003*, (2003)
<http://www.top500.org/lists/2003/06/trends.php>
2. Petitet, A., Whaley, C., Dongarra, J. & Cleary, A. *HPL - A Portable Implementation of the High-Performance Linpack Benchmark for Distributed-Memory Computers*, (2004)
<http://www.netlib.org/benchmark/hpl/index.html>
3. Website, *The Earth Simulator Center, Japan Marine Science and Technology Center*, (2003) <http://www.es.jamstec.go.jp/>

- 162 Distributed Computing & Solid Oxide Fuel Cell Modelling
4. Website, *Windows Clustering Technologies - An Overview*, (2002) www.microsoft.com/technet/
 5. Kronenberg, N. P., Levy, H. M. & Strecker, W. D. VAXclusters: A Closely Coupled Distributed System. *ACM Transactions on Computer Systems* **4**, 130-146 (1986).
 6. Website, *Kentucky Asymmetric Zero*, (2003) <http://aggregate.org/KASY0/>
 7. Website, *Beowulf.org*, <http://www.beowulf.org/beowulf/history.html>
 8. Anderson, T. E., Culler, D. E., Patterson, D. A. & team, a. t. N. A Case for Networks of Workstations: NOW. *IEEE Micro* **15**, 55-64 (1995).
 9. Fischer, M. J. & Merritt, M. Appraising two decades of distributed computing theory research. *Distributed Computing* **16**, 239-247 (2003).
 10. Anderson, D. in *Bioastronomy 99: A New Era in Bioastronomy* (eds. Lemarchand, G. & Meech, K.) 511 (Astronomical Society of the Pacific: San Francisco, 1999).
 11. Website, *SETI@Home website*, (1999) <http://setiathome.ssl.berkeley.edu>
 12. Anderson, D. P., Cobb, J., Korpela, E., Lebofsky, M. & Werthimer, D. SETI@home: An Experiment in Public-Resource Computing. *Communications of the ACM* **45**, 56-61 (2002).
 13. Website, *Distributed Computing Technologies Inc.*, <http://www.distributed.net/>
 14. Website, *The Great Internet Mersenne Prime Search*, <http://mersenne.org/>